NMR INSTRUMENTATION AND STUDIES IN AMMONIUM AND METHYL SUBSTITUTED AMMONIUM COMPOUNDS

A Thesis

Submitted for the award of the Degree of

Doctor of Philosophy

in the Faculty of Science

By

K. J. MALLIKARJUNAIAH

Department of Physics

Bangalore University

Bangalore - 560 056 (INDIA)

August 2007

List of Publications

Journals

1. "^{1}H and ^{19}F NMR relaxation time studies in $(NH_4)_2ZrF_6$ superionic conductor"
   K.J. Mallikarjunaiah, K.P. Ramesh and R. Damle
   Applied Magnetic Resonance (**2008**)
   Doi:10.1007/s00723

2. "^{1}H and ^{19}F NMR study of molecular dynamics in tetramethylammonium hexafluorophosphate"
   K.J. Mallikarjunaiah, K.P. Ramesh and R. Damle
   Solid State Nuclear Magnetic Resonance **34(3),** (**2008**).
   doi:10.1016/j.ssnmr.2008.08.002

3. "^{1}H NMR study of internal motions and quantum rotational tunneling in $(CH_3)_4NGeCl_3$"
   K.J. Mallikarjunaiah, K. Jugeshwar Singh, K.P. Ramesh and R. Damle
   Magnetic Resonance in Chemistry – ***46(2),*** 110-114 (**2008**)..
   doi:10.1002/mrc.2097

4. "Study of molecular reorientation and quantum rotational tunneling in tetramethylammonium selenate by ^{1}H NMR".
   K. J. Mallikarjunaiah, K. C. Paramita, K. P. Ramesh and R. Damle
   Solid State Nuclear Magnetic Resonance **32(1),** 11-15 (**2007**).
   doi:10.1016/j.ssnmr.2007.07.003

5. "Study of molecular dynamics and phase transitions in trimethylammonium trichlorogermanate using ^{1}H NMR and DSC measurements".
   K.J. Mallikarjunaiah, K.P. Ramesh and R. Damle
   Physica Status Solidi – b **244 (10),** 3809-3816 **(2007).**
   doi:10.1002/pssb.200743104

6. "Conditioning and automation of NMR signal acquisition"
   K. J. Mallikarjunaiah and R. Damle
   Vignanabharathi, **17(1)**, 50-55 (**2005**).

7. "Modulation schemes of wide-line NMR signal absorption"
   N. Sasidhar, **K. J. Mallikarjunaiah** and R.Damle
   Journal of Instrumentation Society of India, **32(1),** 1-8 (**2002**).
   www.isoi.in/Journal/BackIssues/32(1).pdf

Preface

Nuclear Magnetic Resonance (NMR) spectroscopy is one of the most powerful tools in modern science to study structure and dynamics of molecules. Basic research regarding phase transition, quantum tunneling, molecular dynamics and structure has been carried out using this spectroscopic technique. The application of NMR to modern day science has extended from the study of chemical dynamics to functional group analysis, medical diagnosis, bonding connectivity and orientation, molecular conformations and even to 3D imaging to resolutions of the order 1 mm.

Though commercial high-resolution NMR spectrometers are available, they are very expensive not only to procure but also to maintain them. However, low-resolution NMR spectrometers are sufficient for NMR second moment and relaxation time measurements. Thus, for those interested in time domain experiments, it is appropriate to develop their own NMR spectrometers. In a few laboratories in India and abroad too, the NMR study of molecular dynamics and phase transitions are being carried out using home made spectrometers.

This thesis describes the assembling and development of wide line and pulsed NMR spectrometer (with high temperature and low temperature cryostat assembly) and Proton (and Fluorine) NMR investigations in a few ammonium and methyl substituted

ammonium metal halides. Proton NMR line widths have been measured in these systems using a homemade wide line NMR spectrometer operating at 7-15 MHz. Proton NMR spin-lattice relaxation time (T_1) have been measured in the temperature range 400 K – 4.2 K.

Inorganic salts containing symmetrical molecular groups like NH_4 and CH_3 are known to have wide spectrum of technological applications such as in medicine, energy and agriculture. Apart from applications, these compounds are of academic interest also. Ammonium and methyl substituted ammonium metal halides have shown to exhibit not only complex reorientational dynamics but also interesting features like diffusion and spin rotation at higher temperatures (> 300K) and structural phase transitions in the temperature range 50 - 400 K. At lower temperatures, some of them have revealed the presence of tunnelling reorientations also. Many of these systems are also known to be good ionic conductors. However, there is rather little NMR data on inorganic compounds with low activation barrier. This thesis describes the NMR study of molecular dynamics in Diammonium hexafluorozirconate [$(NH_4)_2ZrF_6$], Tetramethylammonium hexafluorophosphate [$(N(CH_3)_4)PF_6$], Tetramethylammonium selenate [$(N(CH_3)_4)_2SeO_4$], Trimethylammonium trichlorogermanate [$NH(CH_3)_3GeCl_3$] and Tetramethylammonium trichlorogermanate [$N(CH_3)_4GeCl_3$]. The first two of these compounds are commercially procured while the rest of the compounds have been synthesized and characterized in the laboratory. Powder x-ray diffraction and Differential Scanning Calorimetry (DSC) have been employed for the characterization of the compounds.

The thesis is presented in 5 Chapters. **Chapter 1** starts with a brief introduction to the relevant basic theoretical aspects of NMR spectroscopy required for the present investigations. Different relaxation mechanisms, such as dipole-dipole, translational diffusion and quantum rotational tunnelling etc., the effect of molecular motions on second moment and spin-lattice relaxation time have been discussed in the Chapter 1, with a special attention to unlike spin interaction. This Chapter also discusses the second moment and spin lattice relaxation measurement techniques used in the present investigations.

Chapter 2 describes the assembling and testing of a home-made wide-line and pulsed NMR spectrometer. The wide-line NMR spectrometer basically consists of an electromagnet (Bruker B-MIN C5S), a marginal rf oscillator (operating in the frequency range 5-15 MHz), modulation and detection systems. NMR absorption signal is acquired on to a computer using a 12-bit ADC interface card. The automation of the NMR signal acquisition is found to be not only efficient and cost effective, but it provides a on-line calibration of the magnetic field for on-screen measurement of the line width of the NMR signal. The pulsed NMR spectrometer consists of an rf transmitter capable of delivering short and powerful rf pulses, a high gain and low noise receiver amplifier and a matching network to couple the rf pulses to the sample coil and the sample coil to the receiver. A home built computer controlled Programmable Pulsed Generator (PPG) has been used to generate the required pulse sequences. Assembling and testing of the pulsed NMR spectrometer operating in the frequency range 10-30 MHz is described. The fabrication

of a low temperature gas flow cryostat as well as high temperature assembly is also described.

Chapter 3 describes the NMR spin-lattice relaxation time (T_1) studies carried out in Diammonium hexafluorozirconate [$(NH_4)_2ZrF_6$]. Both ^1H and ^{19}F NMR T_1 measurements have been made at 21.337 MHz as a function of temperature in the range 410 to 11 K. T_1 shows a broad maximum around room temperature. On increasing the temperature, T_1 starts decreasing up to 395 K above which it reduces sharply to less than a millisecond. In the same temperature region, FID duration also has been monitored for both the nuclei. For ^1H, FID duration increases several times as the temperature is increased from 388 K to 410 K, while for ^{19}F, it increases a few times in the same temperature region. Both decrease in T_1 and narrowing of the NMR signal are attributed to diffusion of both NH_4 and F ions through the lattice. Reported high ionic conductivity above 400 K also supports this. ^1H NMR line width above 400 K, as reported, reaches a limit of modulation width indicating the diffusion of ammonium ions. Sublattice movement of F ions is also reported above 400 K. The observed maximum in T_1 in the present study around room temperature is attributed to the competition between diffusion and reorientational motion of the NH_4 ion. On decreasing the temperature below room temperature, both ^1H and ^{19}F T_1 gives rise to minimum around 160 K, which is attributed to NH_4 ion motion. The T_1 behaviour is analyzed based on the cross relaxation between proton and fluorine. At lower temperatures, T_1 remains almost constant up to 50 K. However, on further cooling the sample, T_1 increases for both the nuclei. Further, ^1H T_1 exhibits a shallow minimum around 21 K, which may be attributed to quantum rotational

tunneling of NH_4 ions, which is in agreement with reported line shape analysis in the same compound.

The present investigation reveals that, in Ammonium zirconate, ammonium ion plays a major role in relaxation mechanism in the temperature range of study. At higher temperature, compound shows a diffusion of both ammonium and fluorine sublattice. Sharp increase of FID duration and sudden increase of relaxation rate around 395 K, is supported by wide-line NMR line shape and second moment analysis as well as the conductivity studies. Further, this investigation reveals the reorientational motion of the ammonium ion is responsible for fluorine relaxation also. Another important observation is that even at low temperatures the fluorine nuclei are being relaxed due to quantum rotational tunneling of the ammonium ion. Superionic conductivity in the sample is interpreted as due to the diffusion of NH_4 ion and fluorine sublattice motion.

Chapter 4 describes the NMR studies in tetramethylammonium salts. T_1 studies (at 21.34 MHz) in Tetramethylammonium selenate $(N(CH_3)_4)_2SeO_4$ and Second moment (at 7 MHz) as well as T_1 (at 21.34 MHz) measurements in Tetramethylammonium hexafluorophosphate $N(CH_3)_4PF_6$ have been carried out.

A broad T_1 minimum observed in Tetramethylammonium selenate around 280 K is attributed to the simultaneous motions of CH_3 and $(CH_3)_4N$ groups. Lower activation energy obtained from the T_1 analysis as well as powder XRD measurements confirm that, the present compound crystallizes in cubic form and not in tetragonal. Magnetization recovery is found to be stretched exponential below 72 K with varying stretched

exponent. Low temperature T_1 results show the quantum rotational tunneling of methyl groups and the observed T_1 is the resultant of relaxation of all spin systems.

In $(N(CH_3)_4)PF_6$, ^1H T_1 measurements have been carried out at three Larmor frequencies (11.4, 16.1 and 21.34 MHz). At all frequencies, the observed single asymmetric minimum is attributed to simultaneous reorientations of both CH_3 and $(CH_3)_4N$ groups. Second moment measurements made at 7 MHz also supports this. ^{19}F NMR T_1 measurements have been carried out at 21.34 MHz and 16.1 MHz in the temperature range 350 - 77 K. Cross correlation between proton and fluorine has been invoked to account for the observed ^{19}F T_1 data.

In **Chapter 5,** ^1H NMR T_1 studies in Trimethylammonium trichlorogermanate $[NH(CH_3)_3GeCl_3]$ and ^1H NMR T_1 as well as second moment studies in Tetramethylammonium trichlorogermanate $[N(CH_3)_4GeCl_3]$ are presented. In Trimethylammonium trichlorogermanate $[NH(CH_3)_3GeCl_3]$, ^1H T_1 measurements have been made as a function of temperature in the range 391 – 5.2 K at 20.53 MHz. The T_1 data are analyzed in three parts: the High Temperature region (391 - 272 K), the Intermediate Temperature region (272-100 K) and the Low Temperature region (100 – 5.2 K). The Trimethylammonium trichlorogermanate undergoes several phase transitions (at 388, 323, 272, 100 and 57 K) along with thermally activated reorientations of the trimethylammonium and methyl groups. The observed phase transitions are attributed to the chloride ion diffusion (at higher temperatures) and changes in the symmetry of the $GeCl_3$ ions (at lower temperatures), which may have indirect effect on proton spin lattice

relaxation time. The observed two minima in intermediate temperature region are attributed to reorientation of $NH(CH_3)_3$ and CH_3 symmetric groups and corresponding motional parameters are evaluated. The observation of the decrease of activation energy of the TriMA/methyl groups with decrease in metal ion radius, in $TriMABCl_3$ complexes, may be due to the increased volume (higher metal ion (B) radius). At lower temperatures, T_1 results show quantum rotational tunneling of the methyl group.

In Tetramethylammonium trichlorogermanate $[N(CH_3)_4GeCl_3]$, ^1H NMR second moment (M_2) measurements are carried out, as a function of temperature in the temperature range 300 – 77 K at 7 MHz. ^1H NMR spin lattice relaxation time (T_1) measurements are carried out, as a function of temperature, at two Larmor frequencies 26 MHz and 11.4 MHz in the temperature range 270-17 K TMA-Germanate exhibits thermally activated reorientations of the Tetramethylammonium and methyl groups. In this compound, second moment results show only one plateau region and T_1 results show a single asymmetric minimum than expected two plateau regions in the second moment and two minima in the T_1 studies. This observation is explained by inferring that both the CH_3 and TMA groups in TMA – Germanate are reorienting with the same (order of magnitude) correlation times. It is also noticed that the decrease of activation energy of the TMA/methyl groups with decrease in metal ion radius, in $TMABCl_3$ complexes, may be due to the increased volume (higher metal ion (B) radius). Present investigations have not revealed any change in the magnetization recovery profile even below 170 K. Hence it is concluded that the TMA ion surrounding remains unaltered. At lower temperatures, T_1 results suggest the existence of the inequivalent methyl groups undergoing quantum

rotational tunneling.

All the compounds investigated have given very useful information on the dynamics of the reorienting groups and the influence of the anion dynamics on the activation energy of the reorienting groups. The signatures of unlike nuclear interactions affecting the relaxation of a particular nucleus is seen in the T_1 data. The activation energies of the reorienting groups are found to lie in the range 8 - 30 kJ/mol. The low activation energy for the molecular reorientation in these systems make them good candidates for basic studies as well as potential possible applications.

Most of the results of the present investigations are published in reputed International Journals.

Contents

Chapter 1

NMR - Basic Theory

Nuclear Magnetic Resonance (NMR) spectroscopy is one of the most powerful analytical tools in modern science. Basic research regarding phase transition, quantum rotational tunneling, molecular dynamics and structure analysis has been carried out using this technique. Structural investigations by NMR provide a valuable supplement to X-ray spectroscopy in structure analysis. NMR is indeed an indispensable tool for a modern scientist. The application of NMR to modern day science has extended from the study of chemical dynamics to functional group analysis, medical diagnosis, bonding connectivity and orientation, molecular conformations and even to 3D imaging to resolutions of the order 1 mm. This technique can give information about non-crystalline solids also.

In this introductory chapter, a brief outline of the basic theory of the magnetic resonance phenomenon of and topics relevant to the present work are given. Measurement techniques of second moment and spin lattice relaxation times with special emphasis to different magnetization recovery profiles for different pulse sequences used in the present investigations are also discussed in this chapter.

1.1 Nuclear Spins in a Static Magnetic field

Spin, the intrinsic quantum mechanical property of many fundamental particles or combinations of particles, is described by equations treating angular momentum. Each nucleus (having nuclear spin $\vec{I}$ with angular momentum $\vec{J}$ is associated with a magnetic moment $\vec{\mu}$, is given by

$$\vec{\mu} = \gamma\vec{J}; \qquad \vec{J} = \hbar\vec{I}, \tag{1.1}$$

where γ is the gyromagnetic ratio, characteristic of the given nucleus. The z component of a nuclear spin I has a (2I +1) fold degeneracy, which can be

lifted with an external static magnetic field. When a static magnetic field H_o is applied along the z direction, the energy of the nuclear spin can be written as

$$H = -\vec{\mu} \cdot \vec{H} = -\gamma \hbar I_z E_m = -m \gamma \hbar H_o , \qquad (1.2)$$

where m is the magnetic quantum number and has (2I+1) values from –I, -I +1, ……I-1, I. For spin quantum number I = 1/2, the allowed energy eigenvalules are $\pm \gamma \hbar H_o/2$ corresponding to m = ±1/2. The energy difference between the nuclear states for I = 1/2 is

$$E_{-1/2} - E_{1/2} = \Delta E = \gamma \hbar H_o = \hbar \omega_o , \qquad (1.3)$$

where $\omega_o = \gamma H_o$ is the Larmor frequency.

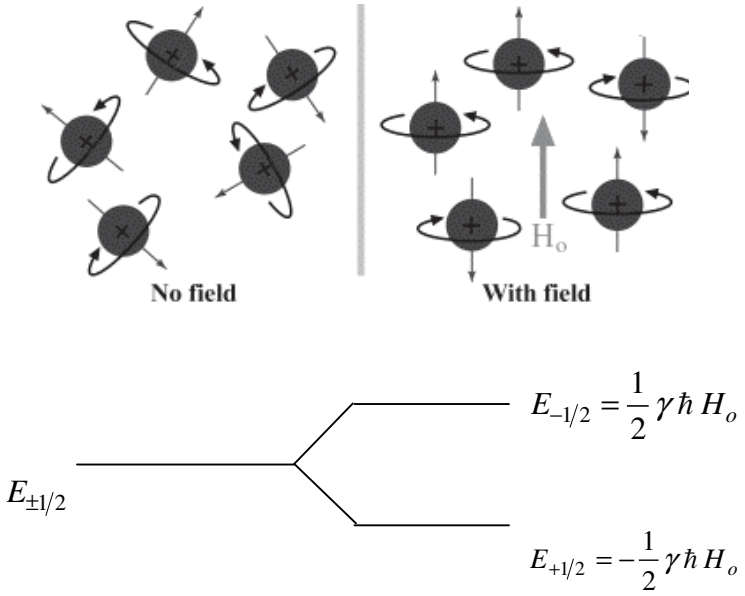

Figure 1.1 Schematic representation of alignment of atomic nuclei and energy levels for a nuclear spin (1/2) in the presence of an external magnetic field.

Figure 1.1 shows the distribution of atomic nuclei in the presence of an external magnetic field and its energy level diagram for a nucleus with spin I = 1/2. The energy

difference between two successive magnetic field split levels, $\Delta E = \gamma \hbar H_o$, is of the order of radio frequency (10^6 Hz). A typical NMR experiment involves either the detection of the energy required to excite the spins to higher energy level (Wide-line) or the exciting the spins to the higher state and subsequent detection of the energy given out by the spins. Hence, the typical energy involved in NMR experiment is of the order of a nano-electron volt.

In a NMR experiment, the nuclear spin system is irradiated by a radio frequency (RF) field (applied in the xy-plane), the frequency of which can be changed appropriately. When the resonance condition is satisfied, that is when $\omega_o = \gamma H_o$, nuclear spins in the lower energy state absorb energy and go to the higher energy state. If the transition causes a detectable change in the experiment, the fact that a resonance has occurred can be ascertained and the measurement of ΔE is reduced to a measurement of frequency. Any resonance experiment involves two steps: (1) 'induce' or 'drive' the resonance, (2) detect its occurrence. Details of detection are discussed later.

Once the nuclear spin system absorbs energy, it relaxes back to its initial energy state. To see how the nuclear spin system relaxes back, consider a macroscopic system, where N nuclear spins of spin I = 1/2 kept in a magnetic field H_o. Out of the N nuclei, N_+ nuclei are in the state with m = 1/2 and N_- nuclei are in the state with m = -1/2 at thermal equilibrium. With the application of a radio frequency field perpendicular to the static magnetic field H_o at 'Larmor frequency' ω_o, 'resonance' occurs, and the population changes, which can be represented by an equation

$$\frac{dN_+}{dt} = N_- W_{-\to+} + N_+ W_{+\to-} . \qquad (1.4)$$

Equation 1.4 is the rate of change of population of m = +1/2 state. $W_{+\rightarrow -}$ denotes the probability per second of inducing the transition of a spin with m = +1/2 to a state with m = -1/2 and $W_{+\rightarrow -}$ denotes the probability for the reverse process. From the time-dependent perturbation theory, the probability per second $P_{a\rightarrow b}$ that a time dependent interaction V(t) induces a transition from a state (a) with energy E_a to a state (b) with energy E_b is written according to Fermi's Golden Rule as [1]

$$P_{a\rightarrow b} = 2\pi\left|\left\langle b\left|V(t)\right|a\right\rangle\right|^2 \delta\left(E_a - E_b - \hbar\omega\right)/\hbar. \tag{1.5}$$

Since

$$\left|\left\langle b\right|V(t)\left|a\right\rangle\right|^2 = \left|\left\langle a\left|V(t)\right|b\right\rangle\right|^2$$

it follows that $W_{+\rightarrow -} = W_{-\rightarrow +} = W$. Using the variables $n = N_+ - N_-$ (the difference in the population of two levels), $N = N_+ + N_-$ and we can rewrite the above equation as

$$\frac{dn}{dt} = -2W\,n\,. \tag{1.6}$$

The rate of absorption of energy by the spin system can be written as

$$\frac{dE}{dt} = N_+ W\hbar\omega - N_- W\hbar\omega = nW\hbar\omega. \tag{1.7}$$

From Eqn. 1.7 it can be seen that 'n' has to be non-zero for absorption of energy by the spin system [2]. This means that there must be a population difference between the energy states for a net absorption of energy. From the solution of equation 1.6, that is

$$n = n_o e^{-2Wt},$$

where n_o is the value of 'n' at t = 0, it is seen that the population difference will eventually vanish and hence resonance also disappears under the action of induced radio

frequency transitions. The nuclear spins, which are in the excited state, can relax back to the thermal equilibrium state provided there is something else (a reservoir) that can accept energy from the spins. This reservoir is generally known as the "lattice". The spin system can continue giving energy to the "lattice" until the relative populations N_-/N_+ correspond to the temperature T of the "lattice". In fact, a characteristic time that can be associated with the thermal equilibration process between the spin system and the "lattice" is known as the "Spin-Lattice Relaxation (SLR) time" denoted as T_1. The "spin-lattice relaxation" can also be understood as the time required to magnetize an unmagnetized sample. The rate equation for the population difference 'n' in the presence of radio frequency field and thermal processes can be written as

$$\frac{dn}{dt} = -2nW + (n_o - n)/T_1 \ . \qquad (1.8)$$

In the steady state, Eqn 1.8 implies that

$$n = n_0 / (1 + 2W T_1). \qquad (1.9)$$

From Eqn. 1.9, it follows that the absorption of energy from the radio frequency field does not disturb the thermal equilibrium population values as long as $2WT_1 \ll 1$. The power absorbed by the nuclei can be increased by increasing the amplitude of the radio frequency field, as long as the above-mentioned condition is satisfied. Once W is large enough so that W ~ 1/2 T_1, the power absorbed levels off despite an increase in W. this effect is called 'saturation'. It is possible to measure T_1 by observing the saturation effect.

1.2 The Classical Picture of Motion

The equation of motion for the nuclear magnetic moment $\vec{\mu}$ is

$$\frac{d\vec{J}}{dt} = \vec{\mu} \times \vec{H} \tag{1.10}$$

or equivalently

$$\frac{d\vec{\mu}}{dt} = \vec{\mu} \times (\gamma \vec{H}) \quad . \tag{1.11}$$

The rotating frame of reference

Equation 1.10 can be understood by invoking the concept of rotating coordinates. In a frame (S′) rotating with respect to the laboratory frame (S) with an angular velocity $\vec{\omega}$, the Eqn. 1.10 can be rewritten as

$$\frac{\partial \vec{\mu}}{\partial t} = \gamma \vec{\mu} \times \left(\vec{H} + \vec{\omega} / \gamma \right) . \tag{1.12}$$

Equation 1.12 has the same form as Eqn. 1.11 provided the magnetic field H is replaced by an effective field $H_e = \vec{H} + \vec{\omega} / \gamma$. For a field H = $\vec{H}_o$ constant in time, the effective field H_e will vanish if a frame rotating with angular velocity $\omega_o = - \gamma H_o$ is chosen. In this frame $\partial\mu/\partial t = 0$, which means $\vec{\mu}$ is a constant vector. However, with respect to the laboratory frame (S), $\vec{\mu}$ is precessing with an angular velocity ω_o about the magnetic field $\vec{H}_o$. if the field $\vec{H}$ is the sum of the constant field $\vec{H}_o = \omega_o \hat{\kappa} / \gamma$ and a field $\vec{H}_1$ perpendicular to $\vec{H}_o$ and rotating around it with an angular velocity $\vec{\omega}$, then the effective field in the rotating frame (S′) is given as,

$$\vec{H}_o = \left(H_o + \omega / \gamma \right) \hat{\kappa} + H_1 \hat{i} \ . \tag{1.13}$$

In the rotating frame, the motion of the magnetic moment $\vec{\mu}$ is a Larmor precession around the effective field $\vec{H}_e$, of angular velocity $-\gamma \vec{H}_o$. The magnitude of the effective field $\vec{H}_e$ can be written as

$$\vec{H}_o = \left[\left(\vec{H}_o + \vec{\omega}/\gamma \right)^2 + \vec{H}_1{}^2 \right]^{1/2} = -\frac{1}{|\gamma|} \left[(\vec{\omega}_o - \vec{\omega})^2 + \vec{\omega}_1^2 \right]^{1/2} \gamma = -a/\gamma \,. \qquad (1.14)$$

The angle θ between $\vec{H}_e$ and the applied field $\vec{H}_o$, which goes from 0 to π is given as

$$\tan\theta = \frac{\omega_1}{(\omega_o - \omega)} \,. \qquad (1.15)$$

If at time t=0, the magnetic moment is aligned along $\vec{H}_o$, at a later time the angle between them will be

$$\cos\alpha = 1 - 2\sin^2\theta \sin^2(at/2). \qquad (1.16)$$

From Eqns. 1.15 and 1.16, it can be seen that a rotating field $\vec{H}_1$, generally small compared with the constant field $\vec{H}_o$ can reorient appreciably a magnetic moment only if its frequency of rotation ω is in the neighbourhood of the Larmor frequency ω_o.

1.3 Quantum mechanical Picture- Spin Hamiltonian

The complete Hamiltonian *H* of a molecular system is in most cases enormously complex and the determination of exact solutions of the equation of motion for the entire quantum mechanical system is a very difficult task. Fortunately, magnetic resonance experiments can be described by a drastically simplified Hamiltonian called the 'Spin Hamiltonian'. The nuclear spin Hamiltonian contains only nuclear spin operators and a few phenomenological constants that originate from the reduction process of the complete Hamiltonian. The Hamiltonian *H* for any particular spin system is the summation of

individual Hamiltonians that describe particular interaction characterized by H_λ, and can be written as

$$H = \sum_{\lambda} H_{\lambda} \ . \tag{1.17}$$

In general the Hamiltonians can be divided into two classes: (1) H_{ext}: Hamiltonians that describe interactions of the spins with external fields. For example, magnetic interactions of the nuclear spins with static external field (H_z) or with time dependent rf field (H_{RF}). (2) H_{int}: Hamiltonians that describe the direct and indirect interactions of the spins with internal fields. For example, dipolar (H_D), scalar (H_J) and quadrupolar Hamiltonian (H_Q) [3]. Here the Hamiltonians relevant to the work carried out in this thesis are described.

1.3.1 The Dipolar Hamiltonian H_D

The Dipolar Hamiltonian H_D for two nuclei (1 and 2) separated by a distance r can be written as

$$H_D = \frac{\mu_o \gamma_1 \gamma_2 \hbar^2}{4\pi}\left[\frac{\vec{I}_1 \cdot \vec{I}_2}{r^3} \frac{3\left(\vec{I}_1 \cdot \vec{r}\right)\left(\vec{I}_2 \cdot \vec{r}\right)}{r^5}\right], \tag{1.18}$$

where $\vec{I}_i$ is the spin angular momentum operator of nucleus i and γ_i is the gyromagnetic ratio of nucleus i (in $s^{-1}T^{-1}$). In matrix form the above equation can be written as

$$H_{DD} = hR \begin{pmatrix} \hat{I}_{1x} & \hat{I}_{1y} & \hat{I}_{1z} \end{pmatrix} \begin{pmatrix} \frac{r^2-3x^2}{r^2} & \frac{-3xy}{r^2} & \frac{-3xz}{r^2} \\ \frac{-3xy}{r^2} & \frac{r^2-3y^2}{r^2} & \frac{-3yz}{r^2} \\ \frac{-3xz}{r^2} & \frac{-3yz}{r^2} & \frac{r^2-3z^2}{r^2} \end{pmatrix} \begin{pmatrix} \hat{I}_{2x} \\ \hat{I}_{2y} \\ \hat{I}_{2z} \end{pmatrix}, \tag{1.19}$$

where $R = \frac{\gamma_1\gamma_2}{r^3}\frac{\mu_o}{4\pi}\frac{\hbar}{2\pi}$.

Equation 1.19 can be abbreviated and written as

$$\mathrm{H}_{DD} = hR\left(\vec{I}_1 \cdot D \cdot \vec{I}_2\right), \tag{1.20}$$

where D is the direct dipolar tensor. If the internuclear vector $\vec{r}$ lies along the z- axis, then the dipolar tensor becomes diagonal given by

$$D = \begin{pmatrix} 1 & 0 & 0 \\ 0 & 1 & 0 \\ 0 & 0 & -2 \end{pmatrix}. \tag{1.21}$$

This is called the principal axis system (PAS) of the dipolar tensor.

In order to discuss the NMR spectrum of two dipolar coupled spins in the solid state, generally Eqn. 1.19 is written in the spherical polar co-ordinate system as

$$H_{DD} = hR\left(A + B + C + D + E + F\right), \tag{1.22}$$

where

$$A = I_{1z} I_{2z} \left(1 - 3\cos^2\theta\right),$$

$$B = -\frac{1}{4}\left(I_1^+ I_2^- + I_1^- I_2^+\right)\left(1 - 3\cos^2\theta\right),$$

$$C = -\frac{3}{2}\left(I_1^+ I_{2z} + I_{1z} I_2^+\right)\sin\theta\cos\theta\, e^{-i\phi},$$

$$D = -\frac{3}{2}\left(I_1^- I_{2z} + I_{1z} I_2^-\right)\sin\theta\cos\theta\, e^{i\phi},$$

$$E = -\frac{3}{4} I_1^+ I_2^+ \sin^2\theta\, e^{-2i\phi},$$

$$F = -\frac{3}{4} I_1^- I_2^- \sin^2\theta\, e^{2i\phi}.$$

Each of the terms ‘A’ to ‘F’ contains a spin factor and a geometrical factor. The common factor hR is referred to as the dipolar coupling constant. If the eigenvalues of I_{1z} and I_{2z} are represented by m_1 and m_2, the spin part of ‘A’ and ‘B’ terms connect states with $\Delta m = 0$, ‘C’ and ‘D’ terms connect states with $\Delta m = \pm 1$ and ‘E’ and ‘F’ terms connect states with $\Delta m = \pm 2$ where $\Delta m = m_1 - m_2$.

The terms ‘C’ to ‘F’ which produce very weak responses at $\omega = 0$ and $2\ \omega_o$ are neglected and hence do not contribute to the line width. The geometrical factors in Eqn. 1.22 are affected by molecular motions. Isotropic tumbling of the molecule averages out the terms A to F, to zero in the case of isotropic fluids and do not affect the transition energies or intensities for the high-resolution NMR spectra of isotropic fluids. However, dipolar interactions do affect the relaxation times even for isotropic solutions. If intra-molecular interactions are considered, molecular tumbling will modulate terms ‘C’ to ‘F’, which will result in spin-lattice relaxation.

1.3.2 Method of moments

Line shape study is an important tool in the analysis of molecular and crystal structure. Theoretical line shape for a two spin system has been solved by Pake [4 - 5], three spin and four spin systems have also been anaylsed by several other authors [6 – 11]. The ^1H NMR spectrum of symmetric molecular subgroups like NH_4, $N(CH_3)_4$, CH_3 and NH_3, contain characteristic, symmetrically disposed lines about the central line depending on the size and shape of the molecular subgroups. The interaction between the nuclear spins of the neighboring molecular groups causes broadening in these lines and removes the structural details in the spectrum, making the task of calculating the line shape formidable. In such cases, Van Vleck (12) has shown that the second moment of the spectrum can be profitably used to get information about the structure and dynamics.

In general, the n^{th} moment of a line shape f (ω) about ω is given by

$$M_n = \frac{\int_0^{\infty} (\omega - \omega_o)^n f(\omega)\, d\omega}{\int_0^{\infty} f(\omega)\, d\omega}\ , \qquad (1.23)$$

where ω is the spectral coordinate in frequency units. If the absorption line is symmetric about ω_o, all odd moments about the center of the line vanish. The second moment of a line is just the mean square line width and is given by

$$M_2 = \frac{\left(\int_0^{\infty} \Delta\omega^2 f(\omega)\, d\omega \right)}{\left(\int_0^{\infty} f(\omega)\, d\omega \right)}, \qquad (1.24)$$

where $\Delta\omega = (\omega - \omega_o)$. The absorption line observed in diamagnetic solids is normally Gaussian and is characterized by its second moment. Second moment contains line broadening contributions from pair-wise interaction between spins. The effect of multispin correlations is given by the higher moments.

The Hamiltonian is truncated to exclude the satellite lines which are far removed from resonance and too weak to be observed. Despite the small magnitude of f (ω) for the satellites in Eqn. 1.24, the magnitude of the term $(\omega - \omega_o)^2$ produces a large contribution to the integral $< (\omega - \omega_o)^2 >$. Van Vleck's calculations show that the overall second moment, including satellites, is 10/3 times the second moment of the main line. Thus the satellite lines contribute 7/3 times the contribution from the main line to the second

moment. To avoid erroneous comparison with the observed second moment, the truncated Hamiltonian is used in calculation of the theoretical second moment.

For a polycrystalline sample, the rigid lattice second moment is given by the Van Vleck expression [4]

$$M_{2RL} = \langle \Delta\omega^2 \rangle_{RL} \propto \overline{(1 - 3COS^2\theta_{ij})^2} \ , \qquad (1.25)$$

where θ_{ij} is the angle between the static magnetic field H_o and the inter-nuclear vector r_{ij} as shown in the Fig. 1.2. The bar indicates the average over θ_{ij}. Van Vleck's expression for the second moment in terms of the coordinates of the nuclei is

$$\langle \Delta\omega^2 \rangle \ = \left(\frac{3}{4}\right)\left(\frac{I(I+1)\gamma^4\hbar^2}{N}\right)\sum_{i<j}\left(\frac{\mu_l^2}{r_{ij}^6}\right), \qquad (1.26)$$

where $\mu_l = (1\text{-}3\cos^2\theta_{ij})$, γ is the nuclear gyromagnetic ratio of spin I and N is the number of spins in the system at resonance.

For polycrystalline sample, the isotropic average of $(1\text{-}3\cos^2\theta_{ij})$ reduces to 4/5. Thus the expression for second moment, for identical spins, becomes

$$\langle \Delta\omega^2 \rangle \ = \left(\frac{3}{5}\right)\left(\frac{I(I+1)\ \gamma^4\hbar^2}{N}\right)\sum_{j}\left(\frac{1}{r_j^6}\right). \qquad (1.27)$$

However, experimentally the second moment M_2 of the absorption line is obtained by numerical integration of the observed first derivative using the expression

$$M_2 = \frac{1}{3}\frac{\int_0^{\infty}(\Delta\omega)^3 f'(\omega)\,d\omega}{\int_0^{\infty}(\Delta\omega) f'(\omega)\,d\omega}, \qquad (1.28)$$

where $\Delta\omega = (\omega - \omega_o)$, is the deviation from the center of the resonance line and $f''(\omega)$ is the amplitude of the derivative signal at ω.

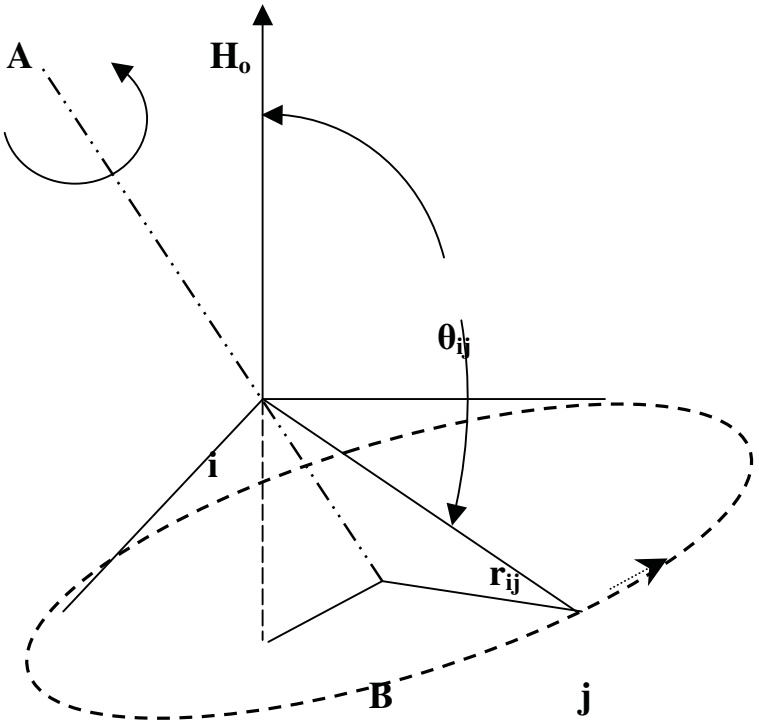

Figure 1.2 Motion of an inter-proton vector r_{ij} about an axis AB.

In the presence of molecular motion (reorientation of the symmetric groups), it is observed that the central portion of the absorption line is narrowed and the wings are broadened. However, it should be noted that the total second moment of a line does not change, but only the observed second moment changes. The observable part of the second moment decreases due to molecular motions.

1.4 Effects of molecular Motion

1.4.1 Line Narrowing

In many solids, there is often considerable motion of the whole molecule or molecular sub-groups about their symmetry axes. As mentioned earlier, we are interested in diamagnetic solids containing symmetric proton groups like NH_4, CH_3 and $N(CH_3)_4$. In such systems, line shape and broadening are determined mainly by dipole-dipole interaction. Molecular motions, which are fast compared to the line width, reduce the width of the resonance lines. If τ_c is the correlation time of the fluctuations and M_2 is the second moment, then the line narrowing occurs when $(M_2)^{1/2}\ \tau_c << 1$, where $(M_2)^{1/2}$ can be regarded as a measure of the line width.

At sufficiently low temperatures, these internal motions are inhibited ($\tau_c^{-1} << (M_2)^{1/2}$) and the second moment attains a rigid lattice value (M_{2RL}). From a study of the temperature dependence of line width or second moment, the motional parameters like correlation time and activation energy can be determined using the expression [4]

$$M_{2R} = M_{2HT} + M_{2RL}\left[\left(2/\pi\right)\ tan(\alpha)(M_2)^{1/2}\tau_c\right], \qquad (1.29)$$

and the Arrhenius equation

$$\tau_c = \tau_o \exp\left(\frac{E_a}{k_B T}\right) \qquad (1.30)$$

Here α is a numerical factor of the order of unity, M_{2R} is the resultant second moment and E_a is the activation energy. However, second moment studies can provide information on the motional parameters only over a limited temperature range, over which the second

moment transition occurs. A typical example to elucidate this variation of second moment is shown in Fig. 1.3 for solid benzene [13].

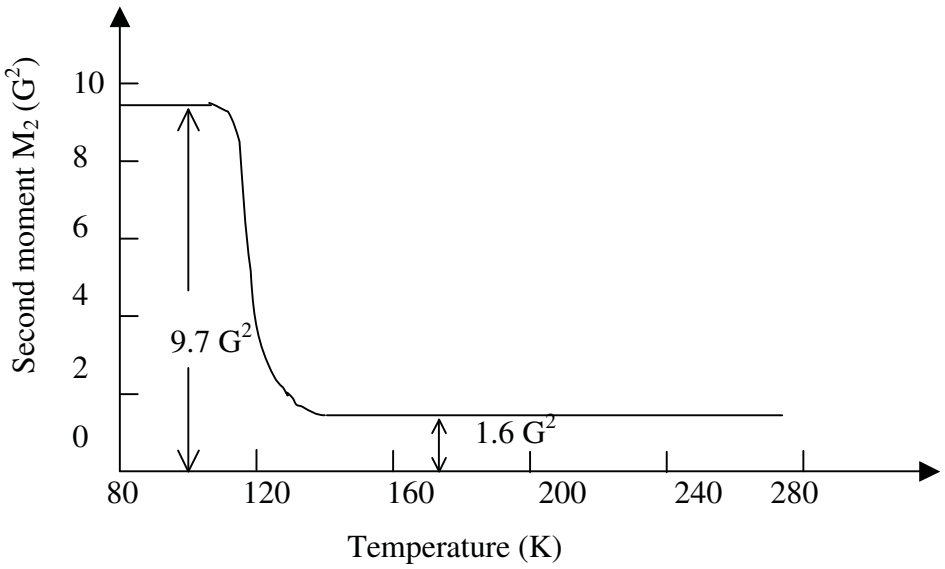

Figure 1.3 Variation of second moment with temperature in solid benzene [13].

1.4.2 Relaxation

The spin lattice relaxation involves an energy exchange between the spin system and the lattice. The following are some of the interactions, which can cause spin-lattice relaxation: (1) magnetic dipole-dipole interaction, (2) translational diffusion, (3) spin rotation interaction and (4) quantum rotational tunnelling. If these interactions have fluctuations at the Larmor frequency (ω_o), they can cause spin-lattice relaxation. The spin-lattice relaxation time (T_1) depends upon the magnitude and the rate of fluctuations of these interactions.

1.4.2.1 Dipole-dipole interaction

In diamagnetic solids (in the absence of quadrupole interactions), spin lattice relaxation is mainly caused by modulation of the dipole-dipole interaction caused by the internal

motions. Since the magnetic dipole-dipole interaction is mainly responsible for the relaxation in all our studies, the procedure to arrive at an expression for spin-lattice relaxation rate ($1/T_1$) due to this interaction (both between like spins and unlike spins) first derived by Bloembergen-Purcell and Pound (BPP) [14], using operator mechanism, is given below.

The dipole-dipole interaction between two spins I and I′ can be written as [3]

$$\hbar H_1 = \sum_q F^q A^q \ , \tag{1.31}$$

where the F^q are random functions of time and the A^q are operators acting on the spin variables with the convention $F^q = F^{-q}$; $A^q = A^{-q}$. $F^q(t)$ can be characterized by the auto-correlation function $G(\tau)$ which is an even and real function of the correlation time τ and can be written as

$$G(\tau) = \overline{F(t)F(t+\tau)}\,, \tag{1.32}$$

where the bar represents an ensemble average.

The Fourier transform of $G(\tau)$ is the spectral density denoted by

$$J(\omega) = \int_{-\infty}^{\infty} G(\tau)\exp(-i\omega\tau)d\tau \ . \tag{1.33}$$

If it is assumed that the correlation function is represented by $\exp\left(-\frac{|\tau|}{\tau_c}\right)$ [14], where τ_c is called the correlation time characteristic of the random motion, then the spectral density function can be written as

$$J(\omega) = \frac{2\tau_c}{1+\omega^2{\tau_c}^2} \ . \tag{1.34}$$

The above expression says that for a given frequency ω, J(ω) is maximum for $\tau_c = \frac{1}{\omega}$. Therefore, for a constant power available in the relaxation spectrum, the rate of relaxation transition induced is a maximum when the correlation time is of the order of $\frac{1}{\omega}$ (the Larmor period). J(ω) decreases and becomes zero for both very shorter and longer τ_c compared with $\frac{1}{\omega}$. Figure 1.4 shows a schematic picture of the spectral density as a function of ω. It can be seen that the power spectrum has a cut-off for a frequency $\omega_o = \frac{1}{\tau_c}$ and is uniform for $\omega < \omega_o$. If ω is much smaller than the Larmor frequency ω_o, then there is no power available for the transition and the relaxation rate $\frac{1}{T_1}$ is very small. If $\omega < \omega_o$, the power spectrum is spread uniformly over a very large band and since its total intensity is constant, J(ω) and $\frac{1}{T_1}$ will accordingly be small. An optimum condition exists for an intermediate value of $\omega_o \sim \frac{1}{\tau_c}$.

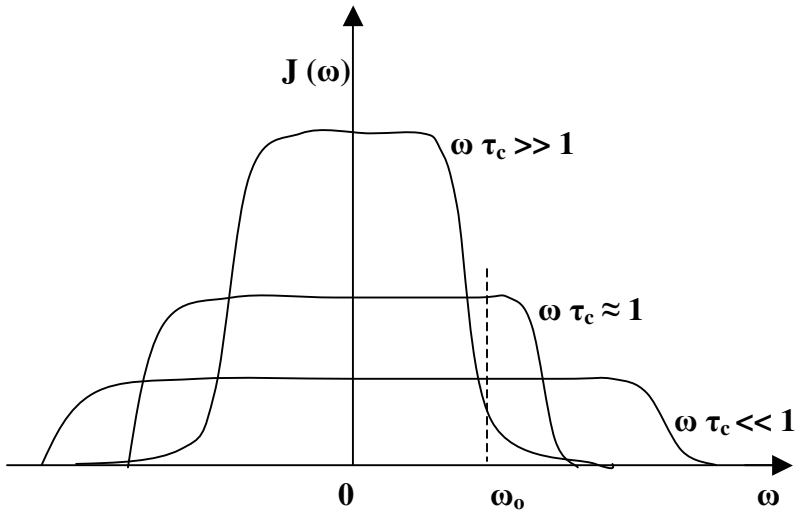

Figure 1.4 Distribution of spectral density as a function of frequency.

The random fluctuations are written as

$$F^1 = \frac{\sin\theta\cos\theta e^{-i\phi}}{r^3},$$
$$F^2 = \frac{\sin^2\theta e^{-2i\phi}}{r^3} \quad , \tag{1.35}$$
$$F^0 = \frac{(1-3\cos^2\theta)}{r^3},$$

where 'r' is the inter-nuclear distance, A^q's which are the operators acting on the system are given as

$$A^0 = \alpha\left(\frac{-2}{3} I_z I_z^{'} + \frac{I_+ I_-^{'} + I_- I_+^{'}}{6}\right),$$
$$A^1 = \alpha\left(I_z I_+^{'} + I_+ I_z^{'}\right) \ , \tag{1.36}$$
$$A^2 = \frac{\alpha I_+ I_+^{'}}{2},$$

where $\alpha = -\frac{\gamma_I \ \gamma_{I'} \hbar}{2}$.

The starting point to arrive at an expression for the relaxation rate is to know the rate of change of magnetisations namely I_z and $I_z^{'}$ with time. It has to be noticed that if the spins $\vec{I}$ and $\vec{I}_z^{'}$ are like spins only the sum $\langle\vec{I}\rangle + \langle\vec{I}^{'}\rangle$ is observed, where as $\langle\vec{I}\rangle$ and $\langle\vec{I}^{'}\rangle$ are observed separately if the spins are unlike.

Like spins

The main Hamiltonian $\hbar H_o$ in the case of like spins is given by

$$\hbar H_o = \hbar\omega_0\left(I_z + I_z^{'}\right). \tag{1.37}$$

the equation of motion of the longitudinal magnetization which is proportional to $\langle \vec{I} \rangle + \langle \vec{I}' \rangle$ cab be written in the form

$$\frac{d\left(\langle \vec{I} \rangle + \langle \vec{I}' \rangle\right)}{dt} = -\left(a_z - a_o\right) . \tag{1.38}$$

In Eqn. 1.38, $a_z = \mathrm{Tr}\,(A_z\,\sigma^*)$ and

$$A_z = \frac{1}{2}\sum_{q\,p} J_q\left(\omega_p^q\right)\left[A_p^q, \left[A_p^{-q}, I_z + I_z^{'}\right]\right]$$

$$\sigma^*(t) = \exp(i H_o t)\,\sigma(t)\exp(-i H_o t)$$

where $\sigma(t)$ is the average density operator of the system. For the case of dipolar coupling between two spins, A_z can be written as

$$A_z = \frac{1}{2}J^1(\omega_I)\left(\left[A^{-1}, \left[A^1, I_z + I_z^{'}\right]\right]\right) + h.c. + \frac{1}{2}J^1(2\omega_I)\left(\left[A^{-2}, \left[A^2, I_z + I_z^{'}\right]\right]\right) + h.c. \tag{1.39}$$

where ' *h.c.* ' denotes the Hermitian conjugate [3]. The commutators can be evaluated using the standard angular momentum commutation relations and in the high temperature approximation one finally gets

$$\langle A_z \rangle \cong \frac{2\alpha^2}{3} I(I+1)\left\langle I_z + I_z^{'}\right\rangle \left(J^1(\omega_I) + J^2(2\omega_I)\right). \tag{1.40}$$

Now Eqn 1.38 can be written as

$$\frac{d\left\langle \vec{I} + \vec{I}' \right\rangle}{dt} = -\frac{1}{T_1}\left(\left\langle \vec{I} + \vec{I}' \right\rangle - \left(\left\langle \vec{I} + \vec{I}' \right\rangle\right)_o\right), \tag{1.41}$$

with

$$\frac{1}{T_1} = \frac{3}{2}\gamma^4\hbar^2 I(I+1)\left(J^1(\omega_I) + J^2(2\omega_I)\right). \tag{1.42}$$

Using the expression for the spectral density, Eqn. 1.42 can be written as

$$\frac{1}{T_1} = \frac{3}{2}\frac{\gamma^4 \hbar^2 I(I+1)}{r^6}\left(\frac{\tau_c}{1+\omega_I^2 \tau_c^2} + \frac{4\tau_c}{1+4\omega_I^2 \tau_c^2}\right) \tag{1.43}$$

Eqn. 1.43 is generally known as the BPP equation. This equation is used widely in the investigations reported in this thesis.

Unlike Spins

The main Hamiltonian in the case of unlike spins is given by

$$\hbar H_o = \hbar\left(\omega_I I_z + \omega_s I_z^{'}\right). \tag{1.44}$$

As mentioned previously, in the case of unlike spins, one has to write the equations of motion of $\langle I \rangle$ and $\langle S \rangle$ separately as $\langle I \rangle$ and $\langle S \rangle$ are observed separately. Proceeding similarly as in the case of like spins, we get

$$\begin{aligned}\left\langle A_z^I \right\rangle = {} & \gamma_I^2 \gamma_S^2 \hbar^2 \langle I_z \rangle S(S+1)\left[\frac{J^0(\omega_I - \omega_S)}{12} + \frac{3}{2}J^1(\omega_I) + \frac{3}{4}J^2(\omega_I + \omega_S)\right] \\ & + \gamma_I^2 \gamma_S^2 \hbar^2 \langle S_z \rangle I(I+1)\left[\frac{-J^0(\omega_I - \omega_S)}{12} + \frac{3}{4}J^2(\omega_I + \omega_S)\right].\end{aligned} \tag{1.45}$$

An identical equation is obtained for $\left\langle A_z^S \right\rangle$ by interchanging the spins I and S. Finally the rate of change of magnetizations $\langle I_z \rangle$ and $\langle S_z \rangle$ can be written as

$$\frac{d\langle I_z \rangle}{dt} = -\frac{1}{T_1^{II}}\left(\langle I_z \rangle - I_o\right) - \frac{1}{T_1^{IS}}\left(\langle S_z \rangle - S_o\right), \tag{1.46}$$

$$\frac{d\langle S_z \rangle}{dt} = -\frac{1}{T_1^{SI}}\left(\langle I_z \rangle - I_o\right) - \frac{1}{T_1^{SS}}\left(\langle S_z \rangle - S_o\right). \tag{1.47}$$

From these equations, it follows that

$$\frac{1}{T_1^{II}} = \gamma_I^2 \gamma_S^2 \hbar^2 S(S+1)\left[\frac{1}{12} J^0(\omega_I - \omega_S) + \frac{3}{2} J^1(\omega_I) + \frac{3}{4} J^2(\omega_I + \omega_S)\right]$$

and

$$\frac{1}{T_1^{IS}} = \gamma_I^2 \gamma_S^2 \hbar^2 I(I+1)\left[-\frac{1}{12} J^0(\omega_I - \omega_S) + \frac{3}{4} J^2(\omega_I + \omega_S)\right]. \qquad (1.48)$$

Similar equation can be obtained for $\frac{1}{T_1^{SS}}$ and $\frac{1}{T_1^{SI}}$ by interchanging the indices I and S. It is important to note from Eqns 1.46 and 1.47 that the polarization of the spins I and S are coupled so that radio frequency field at frequency ω_I will affect $\langle S_z \rangle$ while acting upon $\langle I_z \rangle$.

For thermally activated random processes, the temperature dependence of the correlation time is given any the Arrhenius equation [14]

$$\tau_c = \tau_o \exp\left(\frac{E_a}{k_B T}\right), \qquad (1.49)$$

where E_a is the activation energy for the thermal process, k_B is the Boltzmann constant, T is the absolute temperature and τ_o, the pre-exponential factor, is the correlation time at infinite temperature. At low temperatures when $\omega\tau >> 1$

$$\frac{1}{T_1} = \frac{2C}{\omega_o^2 \tau_c^2} \ . \qquad (1.50)$$

At high temperatures when $\omega\tau << 1$

$$\frac{1}{T_1} = 5C\tau_c \ . \qquad (1.51)$$

At intermediate temperatures when $\omega\tau = 0.69$, T_1 exhibits a minimum and its value is given by

$$\frac{1}{T_{1\min}} = C\frac{1.42}{\omega_o} \quad . \tag{1.52}$$

In these equations, 'C' is the relaxation constant given by

$$C = \frac{3}{2}\frac{\gamma^4 \hbar^2 I\left(I+1\right)}{r^6} \tag{1.53}$$

and $$C = \frac{3}{2}\frac{\gamma_I^2 \gamma_S^2 \hbar^2 I\left(I+1\right)}{r^6} \quad . \tag{1.54}$$

Eqn 1.53 gives the relaxation constant in the case of dipolar interaction between like spins and Eqn 1.54 gives the relaxation constant in the case of dipolar interaction between unlike spins. 'r' is the inter-nucleus distance and the other symbols have been explained before.

By measuring the spin-lattice relaxation time (T_1) as a function of temperature, the motional parameters namely the pre-exponential factor and the activation energy for the relevant molecular motion can be determined.

1.4.2.2 Translational diffusion

Intra-molecular and inter-molecular interactions between the spins are responsible for relaxation. Intra-molecular interactions are modulated by reorientational motion while inter-molecular interactions are modulated by both translational motion as well as the rotation motion. In some solids, it is experimentally observed that, the line width becomes extremely narrow at higher temperatures, which cannot be explained based on motional averaging of the intra-molecular dipole-dipole interaction. A treatment of translational diffusion explains this behaviour. Bloembergen et al [14] and Torrey [15] together proposed a model using random walk method for translational diffusion of ions through lattice and this is well explained in Abragam [3].

The coefficient of diffusion given by the Stokes formula is [3]

$$D = \left(\frac{kT}{6\pi a \eta} \right), \tag{1.55}$$

where 'a' is the distance of closest approach, k is the Boltzman constant and η is the coefficient of viscosity at temperature T (K).

Similarly, the translational diffusion theory developed to explain the relaxation can be represented as [15, 16]

$$\frac{\partial \psi (r, t)}{\partial t} = D \ \Delta \Psi ,$$

where 'D' is the coefficient of diffusion. The solution of the above diffusion equation is

$$\Psi (r, r_o, t) = (4\pi Dt)^{-3/2} \exp\left(\frac{-(r - r_o)^2}{4Dt} \right) \tag{1.56}$$

In Eqn. 1.56, vector 'r' represents the distance (r_1-r_2) between two identical molecules, which diffuse relative to each other and 'r_o' is the equilibrium separation between them. Taking the relative displacements of molecules as 2D t instead of Dt (to prevent the spectral intensities $J_i(w)$ from becoming infinite), the effective motion can be represented by the equation

$$\Psi(r, r_o, t) = (8\pi Dt)^{-3/2} \exp\left(\frac{-(r - r_o)^2}{8\ Dt} \right). \tag{1.57}$$

The limiting value of 'r' and 'r_o' is d, the diameter of the molecule. This is the least distance of approach of the molecules. If the molecules are spherical, then d = 2a, where 'a' is the molecular radius. Considering these aspects, the expression obtained for correlation time can be written as

$$G(t)=\left(\frac{N}{d^3}\right)\int_0^{\infty}\left[J_{3/2}(u)\right]^2\exp\left(\frac{-2Du^2t}{d^2}\right)\left(\frac{du}{u}\right), \qquad (1.58)$$

where u = ρ d ; ρ is the orientation vector relating (r-r_o) and J(u) is the Bessel function. The Fourier transform of this correlation function gives the spectral density as

$$J(\omega)=\left(\frac{N}{dD}\right)\int_0^{\infty}\frac{\left[J_{3/2}(u)\right]^2}{u^3}\frac{du}{\left(1+\left(\omega^2\tau^2/u^4\right)\right)}=\left(\frac{N}{dD}\right)\int_0^{\infty}\left[J_{3/2}(u)\right]^2\left[\frac{u\,du}{\left(u^4+\omega^2\tau^2\right)}\right]. \qquad (1.59)$$

The correlation time for this kind of motion is given by

$$\tau=\left(\frac{12\,\pi\,a^3\eta}{k\,T}\right)=9\tau_2\ , \qquad (1.60)$$

where τ_2 is the correlation time for spin rotation mechanism and this equation is applicable for the homogeneous medium. For a inhomogeneous medium this equation has to be modified [17]. At higher temperature where diffusion is active, $\omega\tau << 1$. Thus the term $(1+(\omega^2\tau^2/u^4))$ reduces to unity and the integral reduces to (2/15) and hence

$$J(0)=\left(\frac{2\pi N\eta}{5kT}\right). \qquad (1.61)$$

Here N represents the density of spins per cubic centimeter. Similarly, it can be shown that [15]

$$J(1)=\left(\frac{8\pi}{15}\right)J(0) \qquad (1.62)$$

$$\textit{and} \qquad J(2)=\left(\frac{32\pi}{15}\right) J(0). \tag{1.63}$$

Hence, Considering these factors the relaxation rate due to translational diffusion can be written as [3, 15]

$$T_{1td}^{-1}\,\alpha\, J(\omega)=\left(\frac{3}{2}\right) I(I+1)\gamma^4\hbar^2\left[J(1)+J(2)\right] \tag{1.64}$$

and hence it can also be represented as

$$T_{1td}^{-1}=\left(\frac{8\pi N}{15a^3}\right) I(I+1)\gamma^4\hbar^2\left[\frac{\tau/2}{1+\left(\omega\tau/2\right)^2}+\frac{\tau}{1+\omega^2\tau^2}\right]. \tag{1.65}$$

1.4.2.3 Tunnelling reorientation

Many organic compounds containing symmetric groups have shown additional minima in the low temperature region of the plots of T_1 versus temperature along with classical minima [18 - 22]. In some compounds, T_1 exhibits minima only at lower temperatures, without showing classical minima at higher temperatures Also, some systems have shown finite T_1 value (~ ms) at lower temperatures, exhibiting a temperature independent down to helium temperatures [20]. This behaviour has been assigned to quantum rotational tunnelling.

In solids, both inter and intra-molecular forces constrain molecules and their internal groups to certain equilibrium positions related to their symmetry. When the hindering potential is quite low, the molecules exist in a number of torsional oscillator states. A coupling of the torsional oscillator states to the rest of the lattice exists which leads to a Boltzmann distribution of population among the torsional oscillator levels.

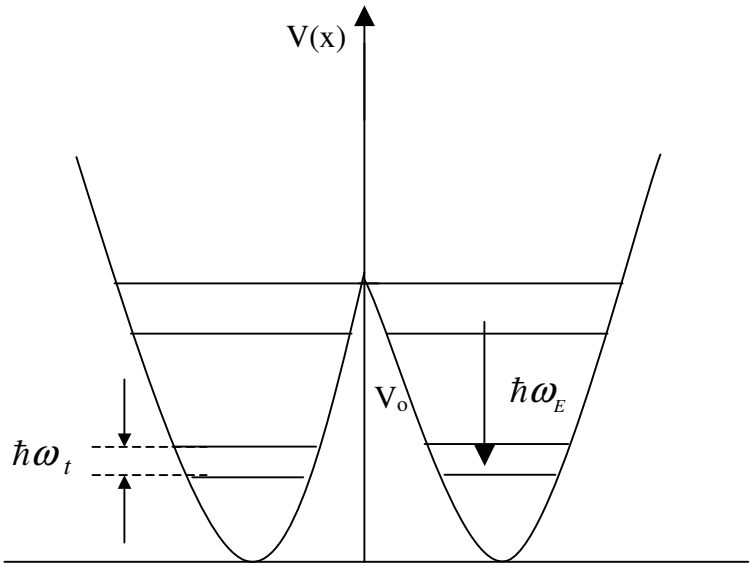

Figure 1.5 A schematic diagram of the tunnelling process in a two-level system.

When the atoms of a molecule can exist in configurations which are distinct and yet energetically identical, the molecule can flip (hopping from ground torsional state of one potential well to a free rotor state and then to the torsional state in another but equivalent potential well) from one configuration to the other, if it is supplied with sufficient energy to surmount the barrier between the configurations. This kind of hopping or random reorientation over the barrier height is a thermally activated process governed by the classical Arrhenius relationship and is efficient only at temperatures high enough in relation to the activation energy E_a [23]. It is well known from quantum mechanics that, the wave function of a particle is not confined only in its potential well, but there is a finite probability of the molecule changing from one configuration to another without being supplied the energy to surmount the barrier. Normally, effects due

to such tunnelling will be observable at low temperatures where effects of random reorientations due to thermal energy possessed by the molecules is suppressed sufficiently [24].

For the harmonic potential, the tunnelling frequency is

$$\omega_t = 2\omega_E \left[\frac{2V_o}{\hbar\omega_E \pi} \right]^{1/2} \exp\left[\frac{-2V_o}{\hbar\omega_E} \right] \qquad for\ V_o > \hbar\omega_E$$

where V_o is the barrier height and $\hbar\omega_E$ is the separation between successive pairs of energy levels corresponding to the harmonic oscillator frequency. ω_t depends on the ratio of the barrier height to the oscillator energy. Hund [25] showed that for $\hbar\omega_E$ =1000 cm^{-1}, the tunnelling period ranges from 10^{-9} to 10^{9} years for a variation $\left[\frac{2V_o}{\hbar\omega_E}\right]$ from 10 to 70. Although this is a case of translational tunnelling, its essential features are the same as for rotational tunnelling. It must be noted that a particle tunnelling between two equilibrium positions is meaningful only if initially (and at any other point of time) it is possible to find it sufficiently well localized in one of its equilibrium positions. The existence of this tunnel splitting was verified by microwave absorption measurements. Fig 1.5 shows the case of tunnelling in a two-well potential.

The general features of the tunnelling in NMR experiments are (a) structures in the NMR line shape (b) finite second moment value of the NMR absorption line compared to that of the rigid lattice value and (c) non-exponential behaviour in the magnetization recovery profile. In addition, another prominent and well-noticed feature of tunnelling is the occurrence of additional minima in the plot of spin lattice relaxation

time (T_1) as a function of temperature (T) at much lower temperatures along with or without classical minima at higher temperatures.

Quantum rotational tunnelling of symmetric groups like NH_4 and CH_3 has been observed in many samples using NMR technique [26-32]. In addition, some efforts have been made to study the effect of isotope dependence on tunnelling by Lalowicz et al [33], Cavagnat [34], Ingman [35], Heuer [36] and recently by Latonowicz et al [37]. NMR line shapes show extra peaks corresponding to tunnelling sidebands [38]. Theoretical models were proposed mainly by Haupt [39], Punkkinen [40] and Clough [41] to explain the tunnelling of the CH_3 and NH_4 groups. However, these models could not explain the temperature dependence of the T_1 in the entire temperature range and also the value of the T_{1min} at low temperatures. Sobol et al [42] attempted to fit the T_1 data in the entire temperature range using TART (Tunnelling Assisted Relaxation Theory) model and found discrepancy between the predictions and the experiment in the level crossing matching regions. They have also carried out frequency dispersion studies to find out the dependence of the tunnel frequency on the Larmor frequency. In $Ge(CH_3)_4$, the temperature dependence of the fast relaxation spectral line indicates that the Zeeman tunnelling relaxation processes cannot be the result of random thermally activated modulations [43, 44].

1. 5 Free induction Decay

At thermal equilibrium and at time t=0, in the presence of an applied dc field H_o, the sample containing the nuclear spins has a magnetization $M_z(0)$ parallel to the applied dc field and is given by $M_z(0) = \chi_o H_0$,

where χ_o is the susceptibility of the nuclei which can be written as

$$\chi_o = \frac{N\gamma^2\hbar^2 I(I+1)}{3k_B T}. \qquad (1.67)$$

Here N is the number of nuclear spins per unit volume of the sample, γ is the gyromagnetic ratio of the sample, I is the nuclear spin quantum number, k_B is the Boltzmann constant and T is the temperature of the sample.

There will not be any transverse magnetization in the sample at thermal equilibrium and at time t = 0. Such a magnetization can be created by applying a rotating field H_1 for a time τ and its frequency being equal to the Larmor frequency ω_o. After the application of the radio frequency pulse, the magnetization along the applied dc field, $M_z(\tau)$ and that perpendicular to the applied dc field, $M_+(\tau)$ can be written as [3]

$$M_z(\tau) = M_z(0)\cos(\omega_1\tau), \qquad (1.68)$$

and

$$M_+(\tau) = M_z(0)\sin(\omega_1\tau)\exp(i\omega_o\tau) \qquad (1.69)$$

After the radio frequency field is cut off, there results a precessing magnetization given by

$$M_+(t) = M_z(0)\sin(\omega_1\tau)\exp(i\omega_o t). \qquad (1.70)$$

The amplitude of the precessing magnetization M_+ (t) given in Eqn. 1.70. It becomes maximum when $\omega_1\tau = \pi/2$ and this is called a 90° pulse. The precessing magnetization in the xy-plane vanishes when $\omega_1\tau = \pi$ and this is called a 180° pulse. The precessing magnetization induces a voltage at the larmor frequency in the NMR sample coil which is picked up and detected and is known as the "fee induction" signal. The precessing magnetization, after some time, decays due to various reasons such as inhomogeneity of the dc magnetic field, the interaction between the nuclear spins etc. and this decaying signal is generally referred to as the "Free Induction Decay"(FID) signal.

1.6 Measurement of M_2 and T_1

1.6.1 Second moment (M_2)

The Wide line NMR absorption signal is acquired onto the computer through a ADC interface as described in the section 2.2.4 (Chapter 2). The derivative signal is acquired onto the computer over certain scan time, by keeping the frequency of the oscillator constant and varying the static magnetic field over certain range around the vicinity of the signal (using auto sweep facility) for the same scan time. The acquired signal is further processed and second moment is evaluated using the numerical integration method using the software ORIGIN (version 7.5).

1.6.2 Spin lattice relaxation time (T_1)

T_1 can be measured in various ways depending on the convenience and sample. The basic principle of measuring the SLR time is first to set certain initial condition (value of magnetization at t = 0) of the spin system by applying a pulse sequence, known as preparation pulses. Then the spin system is allowed to evolve under the influence of H_o

and subsequently the fraction of the magnetization which has relaxed back to the z-direction is detected by another pulse, which is known as monitoring pulse. Different methods used for measurement of T_1 in our experiments are presented here. Figure 1.6 shows different steps of growth of magnetization after the application the π/2 pulse.

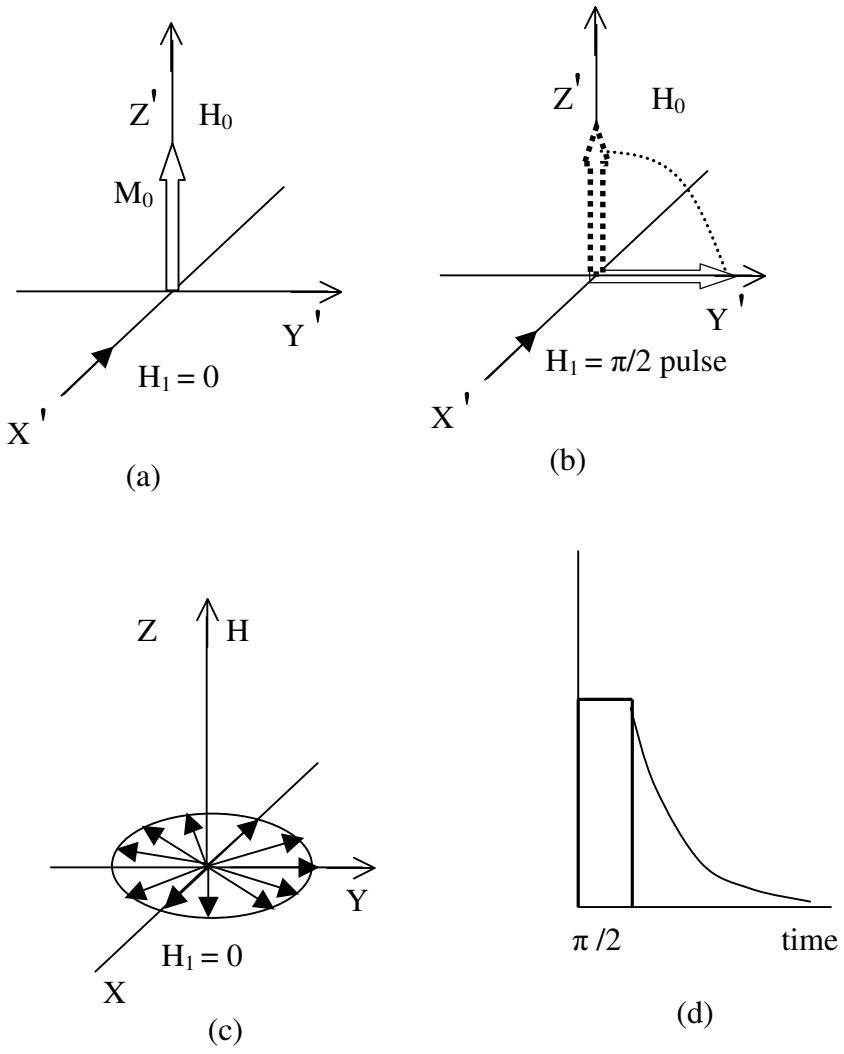

Figure 1.6 (a) Equilibrium magnetization M_o when external rf field $H_1 = 0$

(b) π/2 pulse tips M_o along Y axis

(c) Spin-spin relaxation process (dephasing of the spins)

(d) Fee induction decay (FID)

1.6.2.1 Inversion Recovery Method ($\pi - \tau - \pi/2$)

In this method, the maximum excursion from equilibrium is obtained by inverting the z-magnetization with a selective or non-selective π pulse [45] (an RF pulse, that rotates the magnetization vector by 180°). The recovery towards equilibrium is sampled after a delay τ by a π / 2 pulse, which creates transverse magnetization. For systems with isolated spins, one can write

$$M_z(\tau) = M_0\left[1 - 2e^{\frac{-\tau}{T_1}}\right] \tag{1.71}$$

The equilibrium magnetization M_o and spin lattice relaxation time T_1 have to be determined by monitoring the M_z as a function of delay τ. In some cases, where an ideal π pulse cannot be defined, one has to rewrite the Eqn. 1.71 as

$$M_z(\tau) = M_z(t=0)e^{\frac{-\tau}{T_1}} + M_0\left[1 - e^{\frac{-\tau}{T_1}}\right]. \tag{1.72}$$

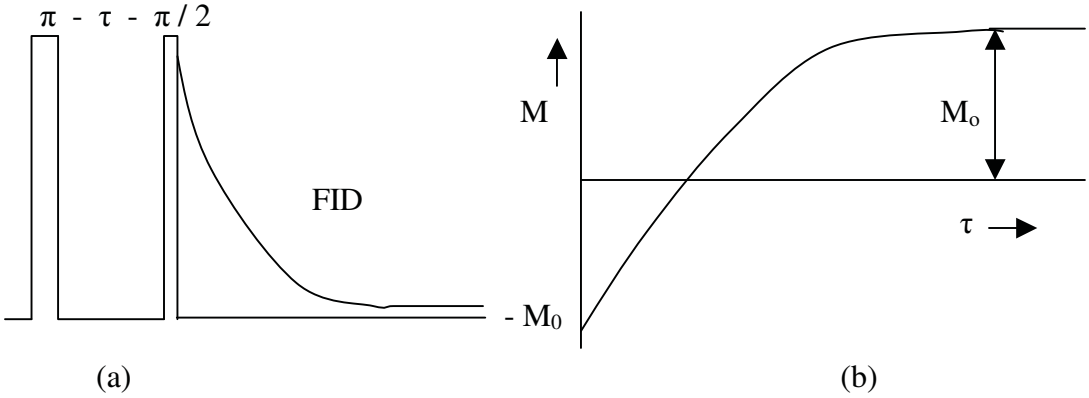

Figure 1.7 (a) The inversion recovery pulse sequence (b) the growth of magnetization, as function of '**τ'.**

In this case, three parameters have to be determined for an isolated spin: the equilibrium magnetization M_0, the initial magnetization after the inversion pulse $M_z(t = 0)$ and the spin lattice relaxation time T_1.

Figure 1.7 shows the inversion recovery pulse sequence and the evolution of the magnetization recovery. T_1 is experimentally determined by measuring M_z at various values of 'τ' and fitting that data to the Eqn. 1.71 using non-linear least square fit with two or three fit parameters. In the present investigations, ORIGIN (Version 7.5) is used for this purpose. This pulse sequence is generally used when T_1 is less than 1 sec.

1.6.2.2 Saturation Burst method

In this method, M_z is brought to the transverse plane by a comb of n π/2 pulses, then the growth of M_z back along the z-direction is monitored by another π/2 pulse as a function of the delay (τ) between the comb and the monitoring pulse. The separation of the pulses in the comb has to be greater than the dephasing time of the spins in the transverse plane. The magnetization in the transverse plane is given as

$$M_z(\tau) = M_0\left[1 - e^{\frac{-\tau}{T_1}}\right] \qquad (1.73)$$

If the tip angle of the magnetization M_z is θ, the expression for the steady state magnetization is

$$M_z = M_o \frac{(1 - e^{\frac{-\tau}{T_1}})\,Sin\ \theta}{(1 - \cos\ \theta \times e^{\frac{-\tau}{T_1}})} \qquad (1.74)$$

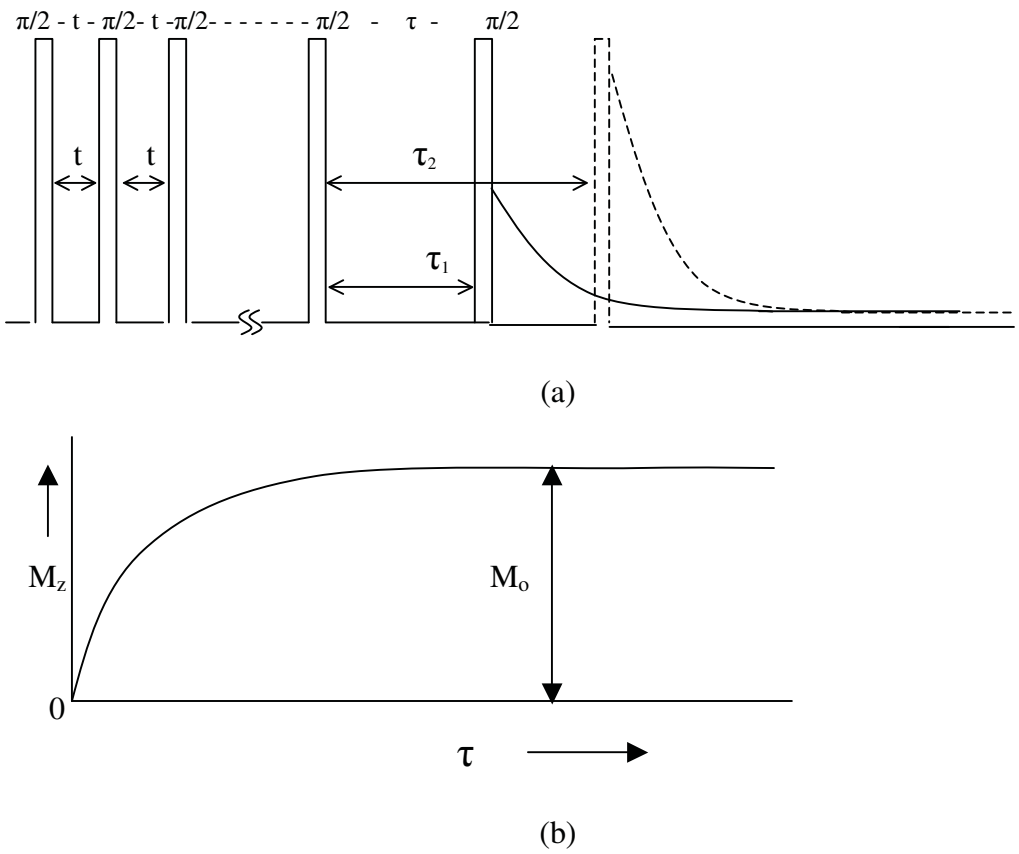

Figure 1.8 (a) The Saturation burst pulse sequence (b) the growth of magnetization.

This means that the magnetization recovery shape is a unique function of the tip angle so that both θ and T_1 can be obtained from the same experiment. Note that the range in which M_z changes is reduced to half. This pulse sequence is ideal whenever T_1 is greater than 1 sec and long waiting time between any two T_1 measurements is drastically reduced.

References

1. Sakurai. *Modern Quantum Mechanics* (Addison- Wesley Publishing Company Inc., Massachusetts, **1994**).
2. Slichter CP. *Principles of Magnetic Resonance* (Springer-Verlag, Berlin Heidelburg, New York, **1978**).
3. Abragam A. *The Principles of Nuclear Magnetism* (Oxford University Press, Oxford, UK, **1961**).
4. Andrew ER. *Nuclear Magnetic Resonance* (University Press, Cambridge, UK, **1958**).
5. Pake GE. *J. Chem. Phys.*, **16(4)**, 327, (1948).
6. Andrew ER and Bersohn R. *J. Chem. Phys*., **18(2)**, 159, (1950).
7. Gutowsky HS, Pake GE and Bersohn R.. *J. Chem. Phys*., **22(4)**, 643, (1954).
8. Bersohn R., and Gutowsky HS. *J. Chem. Phys.*, **22(4)**, 651, (1954).
9. Itoh J, Kusaka R, Yamagata Y, Kiriyama R and Ibamoto H. *J. Phy. Soc. Jpn.*, **8**, 293 (1953).
10. Itoh J, Kusaka R and Saito Y. *J. Phy. Soc. Jpn.*, **17**, 463 (1962).
11. Lalowicz ZT, Mcdowell CA and Raghunathan P. *J. Chem. Phys.,* **70(11)**, 4819, (1979).
12. Van Vleck JH. *Phys. Rev.*, **74(9)**, 1168 (1948).
13. Andrew ER and Eades RG. *Proc. Roy. Soc*., **A 218**,537 (1953).
14. Bloembergen N, Purcell EM and. Pound PN. *Phys. Rev.*, **73(7)** 679 (1948).
15. Torrey HC. *Phys. Rev.*, **92(4),** 962 (1953).
16. Hubbard PS. *Phys. Rev.,* **131(3),** 1155 (1963).
17. Sitnitsky AE, Pimenov GG and Anisimov AV. *J. Mag. Reson.*, **172,** 48 (2005).

18. Allen PS and Cowking A. *J. Chem. Phys.*, **47(11)**, 4286 (1967).

19. Allen PS and Clough S. *Phys. Rev. Lett.,* **22(25)**, 1351 (1969).

20. Koksal F, Rossler E and Sillescu H. *J. Phys. C: Solid State Phys.,* **15,** 5821(1982).

21. Wallach D and Steele WA. *J. Chem. Phys.,* **52**, 2534, (1970).

22. Allen PS and Howard CJ. *Mag. Res and Rel Phen, Colloq AMPERE*, 637 (1970).

23. Horsewill Progr. In Nucl. *Mag. Reson. Spectro*., **35**, 359 (1999).

24. Svare I and Tunstall DP. *J. Phys. C: Solid State Phys.*, **8**. L559 (1975).

25. Hund F. *Z. Phys.,* **43**, 805 (1927).

26. Svare I, Raaen AM and Fimland BO, *Physica B*, **128B** 144 (1985).

27. Svare I, Raaen AM and Thorkildsen G. *J. Phy. C: Solid State Phys.,* **11**, 4069 (1978).

28. Ylinen EE, Tuohi JE and Niemela LKE, *Chem. Phy. Lett.,* **24(3),** 447 (1974).

29. Clough S, Horsewill AJ, Johnson MR, Sutchliffe JH, and Tomsah IBT. *Mol. Phys.,* **81**, 975 (1994).

30. Ingman LP, Punkkinen M, Vuorimaki AH and Ylinen EE. *J. Phy. C: Solid State Phys.,* **18**, 5033 (1985).

31. Tuohi JE, Ylinen EE and Punkkinen M. *Phys. Scr.,* **13**, 253 (1976).

32. Ingman LP, Punkkinen M, Ylinen EE, and Dimitropoulos C. *Chem. Phys. Lett.,* **125(2),** 170 (1986).

33. Lalowicz ZT, Werner U and Muller Warmuth. *Z. Naturforsch,* **43a**, **219**,895 (1989).

34. Cavagent. D., Tevino SF and Magerl A. *J. Phys: Condens Matter,* **1**, 10047 (1989).

35. Ingman LP, Koivula E, Lalowicz ZT, Punkkinen M and Ylinen EE. *Z. Phys. B – Condens. Matter*, **81**,175 (1990).

36. Heuer A. *Z. Phys. B – Condens. Matter*, **88**, 39 (1992).

37. Latanowicz L and Medycki. *J. Phys. Chem. A,* **111(7)**, 1351(2007).

38. Horsewill AJ, Alsanoosi AM and Carlile. CJ. *J. Phys. C: Solid State Phys.*, **20,** L869 (1987).

39. Haupt J. *Z. Naturforsch,* **26a**, 1578 (1971).

40. Punkkinen M. *J. Mag. Reson.*, **19**, 222 (1975).

41. Clough S and McDonald P J. *J. Phys. C: Solid State Phys.,* **15**, L1039 (1982).

42. Sobol WT, Sridharan K R, Camerib. IG and. Pintar MM. *Z. Naturforsch,* **40a**, 1075 (1985).

43. Sridharan K R, Sobol WT and. Pintar MM. *J. Chem. Phys.*, **82(11)**, 4886 (1985).

44. Ligthelm DJ, Wind RA and Smidt J. *Physica B*, **100B,** 175 (1980).

45. Fukushima E and Roeder SBW. *Experimental pulse NMR: A nuts and bolts approach* (Addison- Wesley Publishing Company Inc., Massachusetts, 1981).

Chapter 2

NMR Instrumentation and Experimental Techniques

2.1 Introduction

NMR study of molecular dynamics and phase transitions in inorganic solids (containing symmetric molecular groups) is still an active and rewarding field of research. Commercial NMR spectrometers are not made in India and are expensive to import and maintain. For studying broad lines in solids and for relaxation time measurements, it is appropriate to develop and use own low cost, less sophisticated NMR spectrometers. A few laboratories in India and abroad use home made NMR spectrometers to study of molecular dynamics and phase transition in solids.

This chapter describes the details of both wide-line and pulsed NMR spectrometers developed and assembled for use in the present investigations. The principle of operation of various sub-units, along with the variable temperature insert and associated accessories are described in detail. The development of the NMR signal acquisition in the wide-line NMR spectrometer and computer controlled programmable Pulse Generator used in the pulsed NMR spectrometer are described in more detail.

2.2 Wide-line NMR spectrometer

The Phenomenon of nuclear magnetic resonance was first experimentally observed by Bloch [1] and Purcell [2] independently in 1946. In this technique, known as Continuous Wave NMR (CW NMR), the nuclear magnetic absorption can be described and detected as an additional load or a change in the quality factor Q of the resonant circuit. The Wide Line NMR- which is a frequency domain observation - gives the details of the absorption line shapes directly and is still a useful technique [3-5] to study broad lines in solids for which pulsed Fourier Transform (FT) Spectrometers have the limitation of inability to irradiate with uniform rf power over a wide range of frequencies.

The home made wide line NMR spectrometer used in the present work essentially consists of an electromagnet capable of producing a steady and homogeneous magnetic field, a sensitive low-level radio frequency (rf) oscillator, detector and signal acquisition units as shown in the Fig. 2.1.

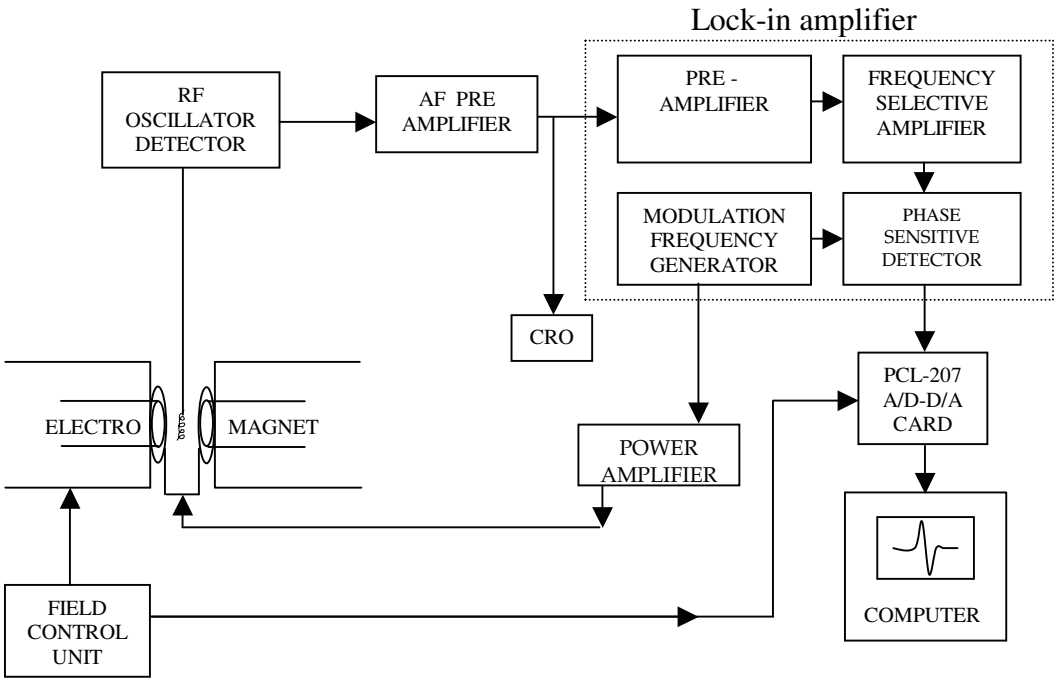

Figure 2.1 Block diagram of the home built wide-line NMR spectrometer.

2.2.1 Electromagnet

The electromagnet is the crucial part of the NMR spectrometer. The static magnetic field applied to lift the degeneracy of the nuclear spin energy levels should be homogeneous and stable. A commercial electromagnet (Bruker B-MIN 90/30 C5S) with automatic field sweep facility is employed for the present work. It has pole pieces of 30 cm diameter with a pole gap of 8 cm. The magnet is provided with copper tubes for water-cooling and can give fields up to 8000 mT in a pole gap of 8 cm at the rate of 20 mT/ampere, when

the coils are connected in parallel. The ratio of the pole face diameter to the pole gap, which is 30 cm / 8 cm ~ 4, ensures good homogeneity of the field. Before recording the NMR spectra, the most homogeneous portion in the magnetic field was located by observing 'wriggles' in proton resonance in glycerin on the cathode ray oscilloscope (CRO) and the samples were always adjusted to be in this region.

2.2.2 Oscillator

A number of rf oscillators used for NMR work have been described in the literature [2, 6-8]. Long relaxation times in certain solids leads to saturation. To avoid this, oscillators, which work at very low levels with good stability, should be used. Andrew [9] has reviewed different types of CW oscillators and Super Regenerative Oscillators used in NMR investigations. Two types of oscillators are commonly used for NMR study in solids, namely, Pound-Knight-Watkins (PKW) oscillator [10] and Robinson's oscillator [11].

A home made Robinson's oscillator (rf oscillator working in the frequency range 5-15 MHz) with conventional magnetic field modulation and phase sensitive detection technique is used for the observation of first derivative of the absorption signal [12]**.** The circuit diagram of the modified version of Robinson oscillator is shown in the Fig. 2.2. It uses three stages of rf amplifications constructed using pentodes E180f that has high gain bandwidth. The pentode EF95 with a low input capacitance (4 pf) is used as a limiter-detector and a low noise high gain EF86 is used as the audio amplifier. L_2, C_2 combination takes care of any direct modulation pick-up in the tank coil L_1 where the sample is placed. Rf level as low as 20 mV can be obtained with good frequency stability. The frequency of oscillation is read by a frequency counter (UNIVERSAL, Model HIL

2722) and has been found to be stable. The sample consisting of nuclear spins is placed in the tank coil [L_1] of the rf oscillator, which is projected between the pole pieces of an electromagnet. The size of the tank coil and hence the sample is about 12 mm in length and 10 mm diameter.

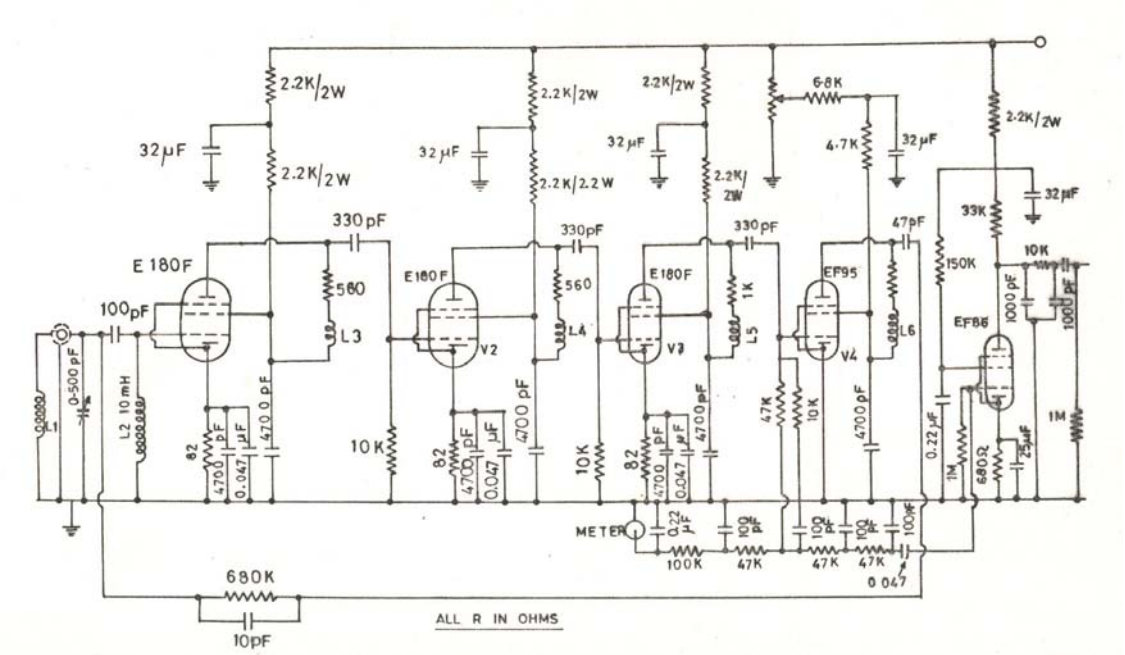

Figure 2.2 Circuit diagram of Robinson oscillator.

When the frequency of the rf oscillator is fixed and the static magnetic field is linearly varied through resonance, the sample begins to absorb energy from the rf field (applied at right angles to the static field) and one observes a resonance absorption as a function of the strength of the static field. The resonance absorption is given by a simple resonance condition $\omega_o = \gamma H_o$, where ω_o is the frequency of the applied rf magnetic field in radians, H_o is the strength of the static magnetic field in Tesla and γ is the gyromagnetic ratio of the nucleus. The intensity of the resonance absorption signal, the width and shape of the signal contain information about the structure and dynamics of the

system being investigated. A locally made lock-in-amplifier has been used for phase sensitive detection of the absorption signal.

2.2.3 Modulation and lock - in detection

A NMR spectrometer operates at a fixed frequency and the spectrum is normally scanned by the linear variation of the static magnetic field. When the separation between the two nuclear spin energy levels is equal to the quantum of energy 'hυ' of the incident photons, absorption takes place and one gets an absorption spectrum. The resonance absorption by the sample is indicated by a change in the detector current.

The direct detection of the NMR absorption is difficult due to following reasons:

a) *Low signal levels*: The decrease in the rf level as a result of absorption by the sample is extremely low which follows directly from the very nature of the NMR experiment. The population difference between the nuclear spin energy levels at thermal equilibrium is so small that only a small fraction of the spins actually contributes to absorption.

b) *Contribution of noise components to the output signal:* The signal is always accompanied with noise components at various frequencies. In other words, the signal will be actually buried in noise.

However, if the signal information can be made to appear at only one frequency, all other frequencies will be filtered out, thus bringing about a considerable improvement in the signal to noise ratio (S/N). This is accomplished by a technique known as "Phase Sensitive Detection" (PSD). Further, since it is difficult to have PSD operating at rf frequencies, the phase sensitive detection needs to be done at a much lower frequency. It is therefore necessary to use some kind of signal modulation with a low frequency ac voltage. Thus, modulation – phase sensitive detection is the most popular detection

scheme in NMR. The most widely used modulation in NMR experiments is the magnetic field modulation. The dc magnetic field H_o is modulated by a low frequency alternating voltage so that the magnetic field passes periodically through the resonance field. The output of the detector will then be an alternating voltage at the modulation frequency. This signal is amplified by a narrow band amplifier and can be either displayed on CRO or recorded after phase sensitive detection.

In an actual experiment, the magnetic field modulation is provided by the two Helmoltz coils placed on either side of the sample coil along the axis of the static magnetic field. The coils are driven by a low frequency (any low frequency < 200 Hz, which is not an integral multiple of line frequency) generator. A small ac magnetic field at the modulation frequency is thus superimposed on the dc field. Under such conditions, the rectified signal at the detector will be amplitude modulated at the modulation frequency.

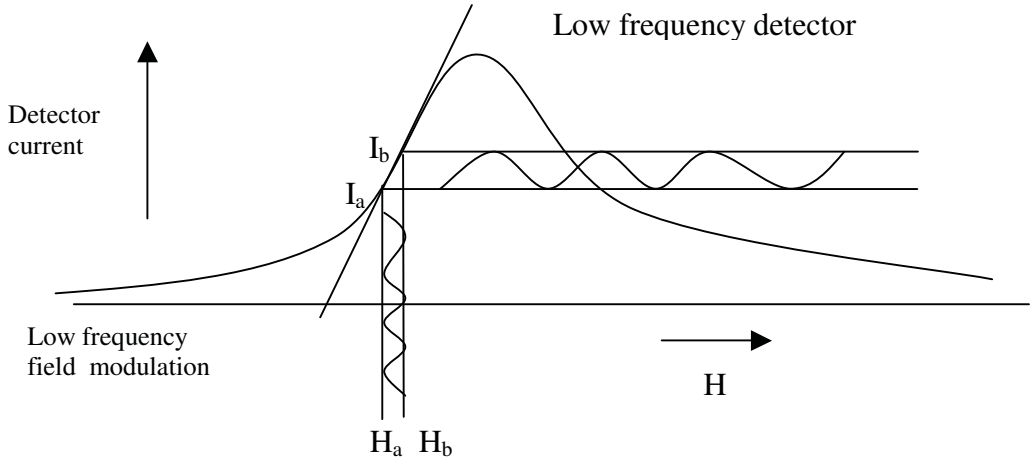

Figure 2.3 Effect of small amplitude field modulation on the detector output current. The static magnetic field is modulated between the limits H_a and H_b. The corresponding current varies between the limits I_a and I_b.

As the magnetic field approaches the resonant value, the sample begins to absorb energy from the rf field. This will cause a slight decrease in the coil Q (quality factor) and hence a decrease in the rf level. Thus, the resonant absorption will appear as a change in the detector current. If the amplitude of modulation is small compared to the line width, the amplitude of the NMR signal will be approximately proportional to the slope of the absorption curve at the center point of modulating field, i.e., to the first derivative of the absorption signal [13]. This can be understood with reference to the Fig. 2.3. The tangent to the absorption curve at a chosen point is taken to approximate the small portion of the curve traversed by the modulating magnetic field. Considering a small portion of absorption curve traversed by the modulating field, as the total field varies between the limits H_a and H_b, the detector current also varies sinusoidally between the limits I_a and I_b. If the amplitude of field modulation is small, then the excursion I_a - I_b will also be small and hence equal to the slope of the absorption curve (or the first derivative of the absorption).

$$\frac{I_a - I_b}{H_a - H_b} = \frac{\Delta I}{\Delta H} \qquad or \qquad \lim_{\Delta H \to 0} \frac{\Delta I}{\Delta H} = \frac{dI}{dH}$$

The input to the detector is thus the rf absorption modulated at the modulation frequency while the output of the detector will be a demodulated signal proportional to the first derivative of the rf absorption. Slope of the absorption curve is zero at resonance. At field values far from resonance, the output of the detector will be zero as shown in Fig. 2.4. At the inflection points where the slope is maximum, the amplitude of the output signal will also be maximum. Thus as the magnetic field is swept through the resonance, the output of the detector will be a signal at the modulation frequency whose amplitude is

proportional to the slope of the absorption curve. Since the output polarity of the PSD is governed by the sign of the slope, for small amplitude of modulation, the output signal appears approximately as the first derivative of the absorption signal. Use of modulation amplitudes approaching the line width leads to a distorted signal.

After detection, the signal at the modulation frequency undergoes narrow band amplification. At this point, further reduction in noise is achieved by PSD. A lock-in-amplifier is normally used for this purpose. Apart from field modulation and field sweep, we have also tried other uncommon and complex modulation and detection schemes [14] such as

(i) Frequency modulation with field sweep,

(ii) Field modulation with frequency sweep and

(iii) Frequency modulation with frequency sweep.

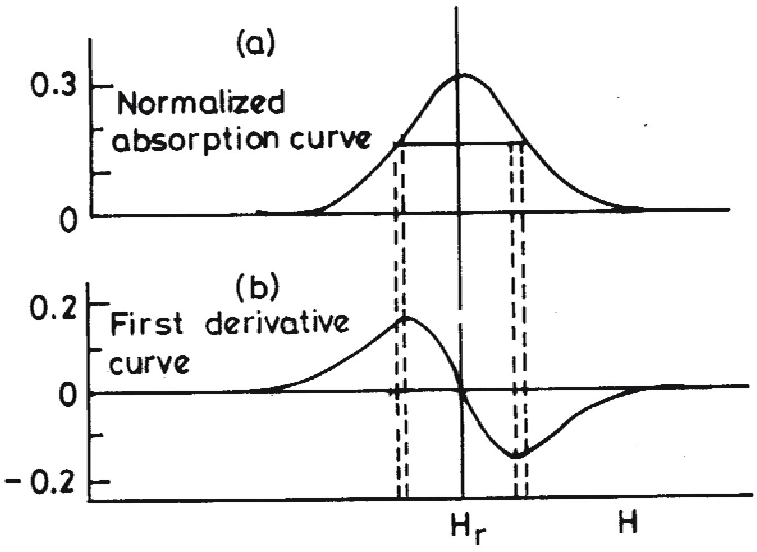

Figure 2.4 NMR line shapes (a) Absorption spectrum (b) First derivative spectrum.

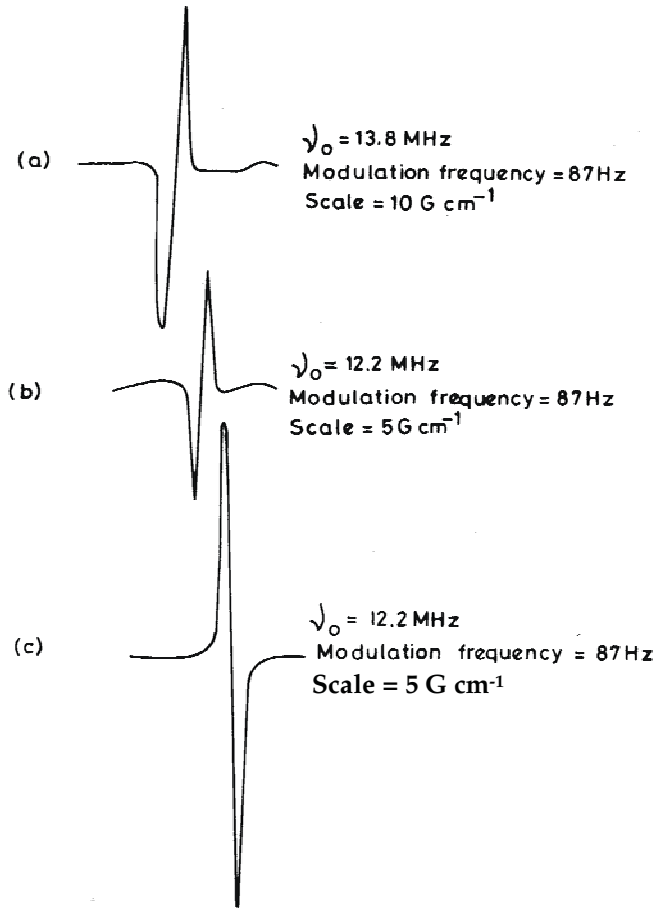

Figure 2.5 ^{1}H NMR signal in glycerin with (a) field modulation and field sweep (b) frequency modulation and field sweep (c) field modulation and frequency sweep.

All the detection schemes employed leads to a derivative signal to be observed at the output of the PSD. This is evident from the simple resonance condition. Thus, whether we employ a field modulation or frequency modulation, the resulting amplitude modulation of the amount of rf absorption by the sample leads to a derivative signal when a PSD is used along with modulation. As can be seen from the recorded signals [Fig. 2.5], all the detection schemes more or less lead to the same shape and intensity (S/N ratio) of the signal. In scheme (i) and (ii) indicated above, there is hardly any change in the frequency of the oscillator during the time over which the signal is recorded. However the frequency modulation and frequency sweep experiment did not give raise to a good

signal. This is because simultaneous modulation and sweep results in the drastic instability of the oscillator frequency and hence the performance of the oscillator. The oscillator frequency changes by an order of few kHz during the recording time, thus bringing about a distortion in the recorded signal. Thus, this scheme of modulation and detection is thus found to be rather impractical.

Lock in amplifier

Lock in amplifier is just a narrow band detection system that is capable of measuring signals buried in noise. Lock-in-amplifier functions by comparing the input signal against a reference signal and ignoring other input components, which are not synchronous with the reference. A locally make Lock in amplifier (EMCO, Model EE201) is used for the present experimental work. The block diagram of the lock in amplifier is given in the Fig. 2.6. A broad band amplifier first amplifies the signal input and a portion of the signal spectrum centered about the desired signal frequency is selected and amplified by a tuned amplifier. The output of the tuned amplifier is applied to the mixer whose output is proportional to the cosine of the phase angle between the signal and reference voltages. The output of the mixer is passed through the time constant and dc amplifier circuit where the upper side band produced in the mixing process is rejected and the lower side band, including the zero frequency component corresponding to the exact signal frequency is amplified.

The heart of the lock-in-amplifier is the Phase Sensitive Detector (PSD), which detects only that part of the input signal, which has the same phase and frequency as that of the reference signal. The PSD output that is proportional to the input signal is rectified and filtered by a selected RC combination and then recorded.

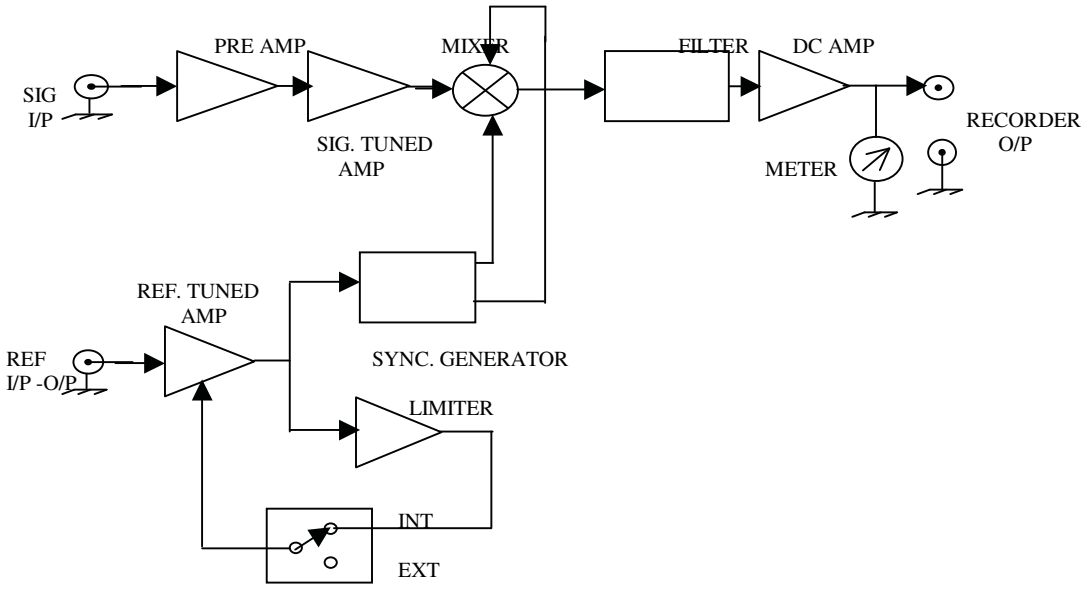

Figure 2.6 Block diagram of the Lock-in amplifier.

The derivative signal may be either increasing or decreasing on the low field side depending upon the phase adjustment of the phase detector or polarity of the recorder connection. The sense of recorded signal is totally irrelevant to its interpretation (one is a mirror image of the other). Recorded spectra of either phase are found in the literature. In the present work, a low frequency ac signal at 87 Hz, derived from the in built oscillator in the lock-in amplifier, is power amplified using a power amplifier (Phillips, Model LMD 8120) and then fed to the Helmholtz coils for magnetic field modulation. The same ac signal at 87 Hz is used as a reference signal for the lock-in amplifier. The detected signal from the oscillator-detector is further amplified using an audio amplifier. A R-C coupled triode amplifier made of ECC 83 (ECC 83 Level AC Microvoltmeter Type TM 3B) is used for this purpose. The circuit diagram of the audio amplifier is given in the Fig. 2.7. The amplified signal is then fed to the lock-in amplifier for phase sensitive detection.

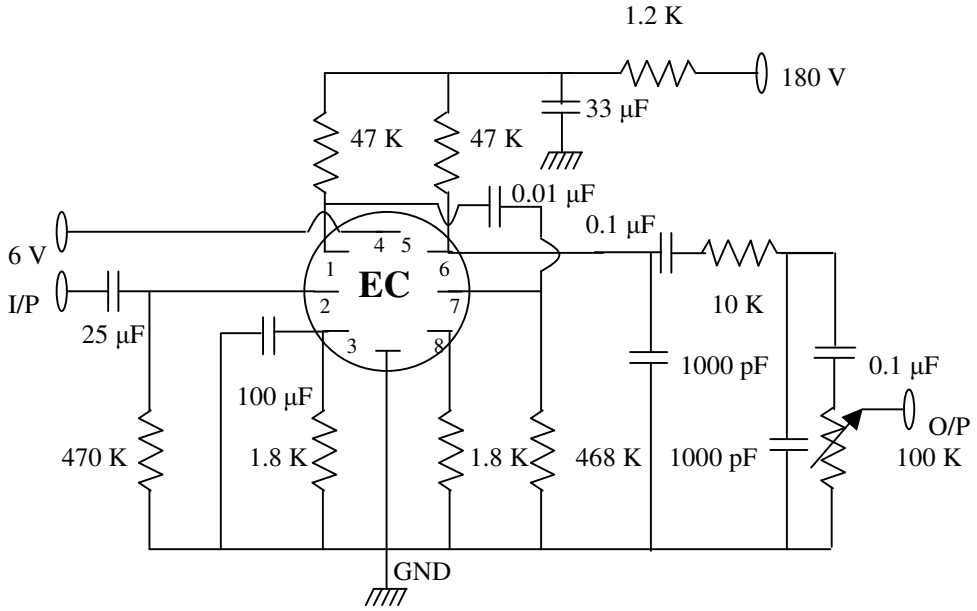

Figure 2.7 Circuit diagram of the audio amplifier built with ECC83 (All R in Ω).

2.2.4 Signal acquisition and Automation

Customarily, NMR signals are recorded using a pen recorder. However, pen recorders are not only cumbersome to use but are expensive. With the availability of a variety of digital signal processing interface cards, it is easier and efficient to acquire the signal on to a computer through Analog-to-Digital (ADC) interface. In the present NMR spectrometer, the output of the lock-in-amplifier is acquired onto the computer through a ADC interface by employing a Dynolog make 12-bit PCL-207 AD/DA interface card. PCL-207 is a low-cost AD/DA multifunction data acquisition card for IBM PC/XT/AT and compatible computers. It uses hardware based successive approximation method providing 25,000 samples per second acquisition rate. The true 12-bit conversion gives an overall accuracy of 0.015% reading ± 1 bit. The output channels provide fast settling time with high accuracy. A high quality multiplexer in the input stage provides 8 single ended analog inputs. Standard input and output ranges are user selectable and independent of each other. PCL-207 also provides powerful and easy to use software driver routines which

can be accessed by the basic CALL statements. With these driver routines, application programs become much easier.

The A/D interface card is inserted in the CPU of the computer and is connected to outside environment through a terminator board. The terminator card is a double-sided PCB and can be used either in the single-ended mode of operation or differential mode of operation. The terminator card is used in the single-ended mode of operation, as only two signal tapings need to be used for NMR signal acquisition. The magnetic field tap signal from the field sweep unit is connected to channel 0 and the output of the lock-in amplifier is connected to channel 1 of the terminator board. To test the working of the A/D card a test program written in 'C' language need to be executed. This execution displays the input and analog voltages of the interface card and their ratings. After ensuring the working of the A/D card, a Demo 01 program, which activates the A/D card by software triggering, is executed to verify whether the card is capable of accepting the analog inputs and providing digital outputs. This ensures that the A/D card is interfaced successfully.

The block diagram of the PCL-207 AD/DA card is shown in Fig. 2.8. The base address is selectable by a 8-way DIP switch provided on the interface board. PCL 207 requires 16 consecutive address locations in the I/O space. Valid addresses are from Hex000 – Hex3f0. When the software routine addresses the DIP switch address, the card is enabled. The reference voltage generator produces the desired reference voltages, which are jumper selectable. In the D/A operation, the digital input from the PC bus is fed to a latch through the data buffer. The latched digital value is fed to the DAC logic for D/A conversion. The analog output is fed to the buffer and finally to the 20 pin FRC connector. In the A/D operation, any one of the 8 channels present on the 20 pin FRC can

be selected by the MUX. For impedance matching, the input signal is buffered and then fed to the ADC. The ADC can be software triggered by outputting the required data through the specific address register. The converted data can be read through 2 latches, one containing the higher byte and the other lower byte. The data is fed to the PC bus through the data buffer [15].

There are two ways to accomplish the PCL-207 functions in application programs. The first method is to use PCL-207 driver routines and let the driver handle the I/O port interface. The second method is to use I/O port instructions in the application program directly. The former method gives greater flexibility in dealing with special application requirements. In the present work, this programming method is employed so that high-level languages viz., BASIC or C, which support input and output instructions, can be used. A simple program in GW BASIC is used to acquire the NMR absorption signal as a function of the magnetic field swept through the resonance. The program used in the present study is given in the Appendix 1. As the magnetic field is swept through resonance, the digitized data of the first derivative signal of nuclear absorption is stored and the plotting of the data points gives the signal as a function of the actual magnetic field swept through the resonance.

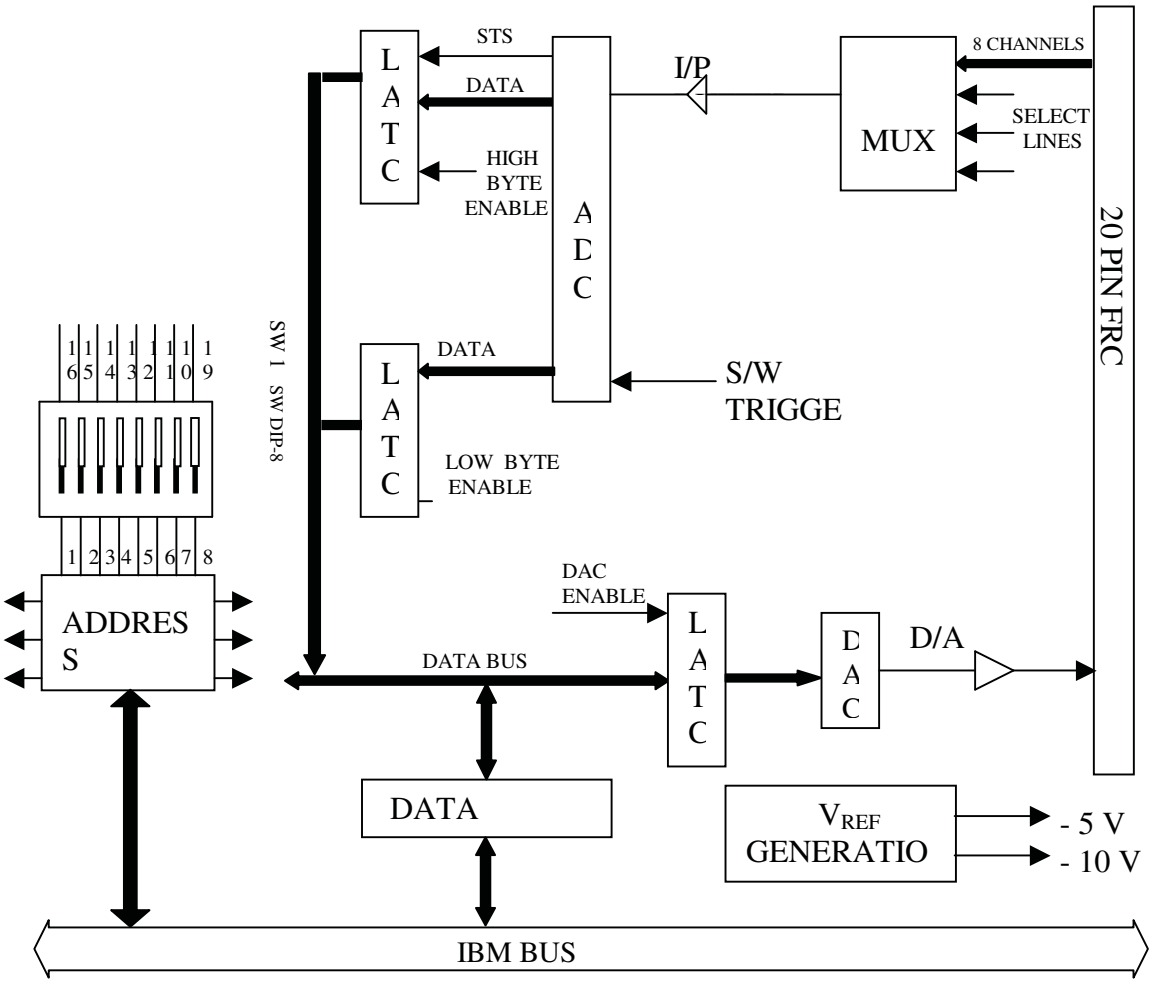

Figure 2.8 The block diagram of the PCL-207 AD/DA card.

For accurate field calibration, the signal tap from the field sweep unit needs to be reduced to acceptable voltage level of the ADC input. At 10 Ampere of magnet current, the sweep voltage level is about 30 V. Hence a simple potential divider circuit given in Fig. 2.9 is incorporated to reduce this voltage to the selected ADC input voltage range (– 5 V to +5 V). Appropriate scaling incorporated in the program facilitates the calibration of the magnetic field on the x-axis, so that direct measurement of the line width is possible on-screen without obtaining the hard copy of the signal. This method thus eliminates the calibration run which is usually required when the signal is recorded using pen recorders. For weak signals in some samples, single acquisition of the nuclear

absorption as a function of magnetic field may not yield good S/N ratio. In such cases, the signal needs to be acquired a number of times and applying signal averaging would give rise to improvement in S/N ratio.

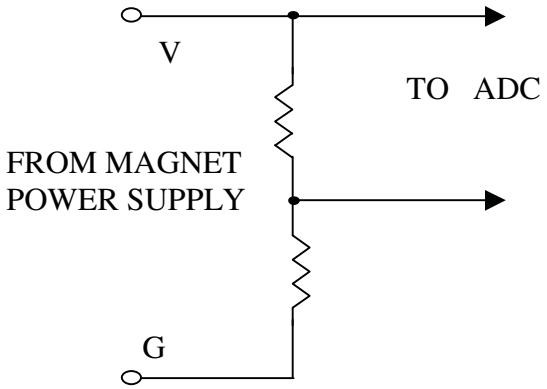

Figure 2.9 Circuit diagram of the potential divider.

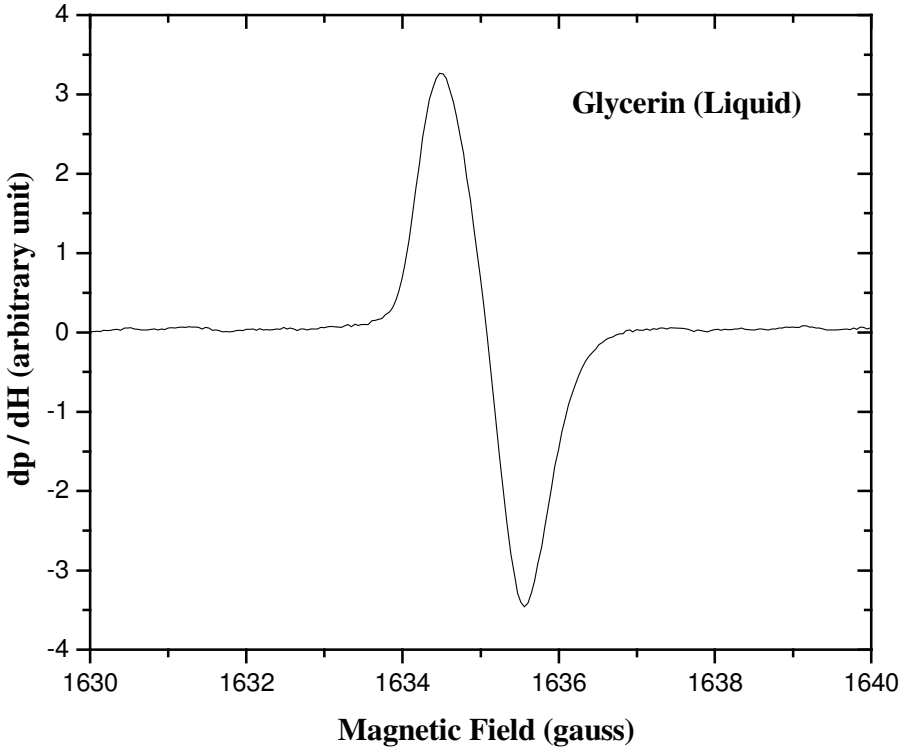

Figure 2.10 The ^{1}H NMR signal in standard sample of glycerin at 7 MHz.

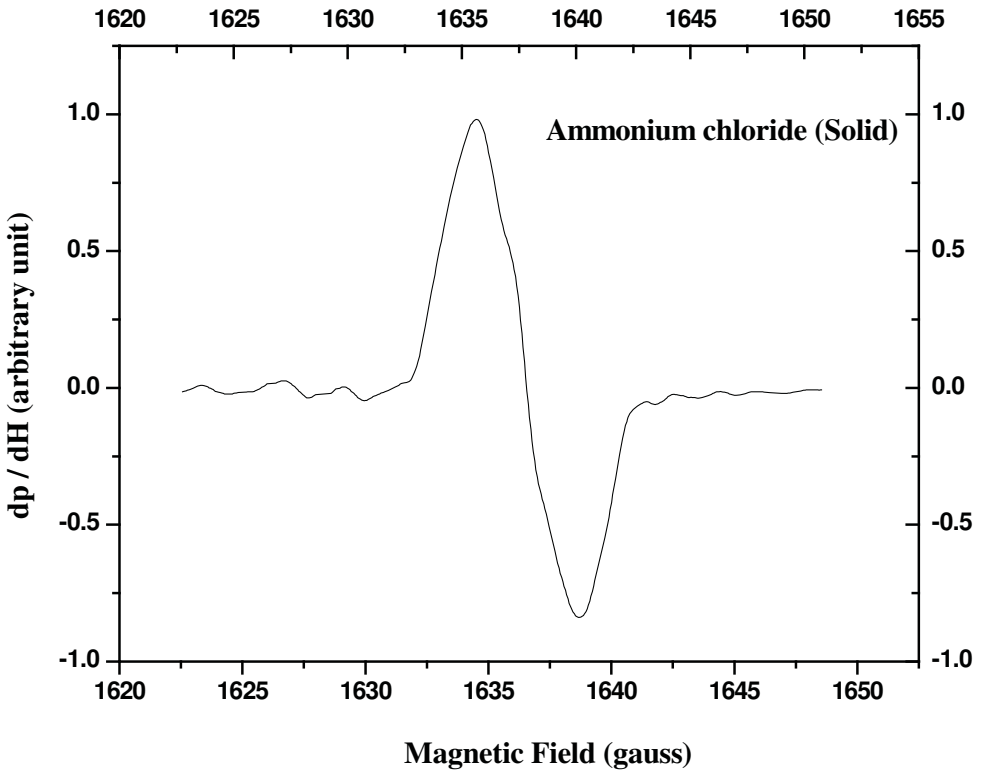

Figure 2.11. The ^{1}H NMR signal in a solid NH_4Cl at 7 MHz.

The magnetic field calibration has been verified by acquiring the signal of a known sample a number of times. Figure 2.10 shows the ^{1}H NMR signal for the standard sample of glycerin. Figure 2.11 shows the ^{1}H NMR signal in a solid NH_4Cl at 7 MHz. The measured line width is in good agreement with the value reported in the literature [16].

2.3 Pulsed NMR spectrometer

Ever since Ernst and Anderson [17] in 1966 devised the first pulsed Fourier Transform NMR spectrometer, NMR techniques- particularly the pulsed NMR techniques- have seen a tremendous growth in past few decades. In the pulsed NMR experiment, a very

short high-power pulse, of the order of a few microseconds, is applied to the sample to excite a band of frequencies about the Larmor frequency. For relaxation time measurements, it is suitable to employ a home made, less sophisticated pulsed NMR spectrometer compared to modern commercial high-resolution NMR spectrometers.

Pulsed NMR experiments are not only more informative, but they require more complex circuitry for power transmission and signal detection. While the circuitry for continuous wave NMR spectrometer is straight forward, the pulsed NMR spectrometer has a number of requirements, some of which could be even mutually exclusive. The block diagram of the home-assembled pulsed NMR spectrometer operating in the frequency range 10 - 30 MHz is shown in Fig. 2.12.

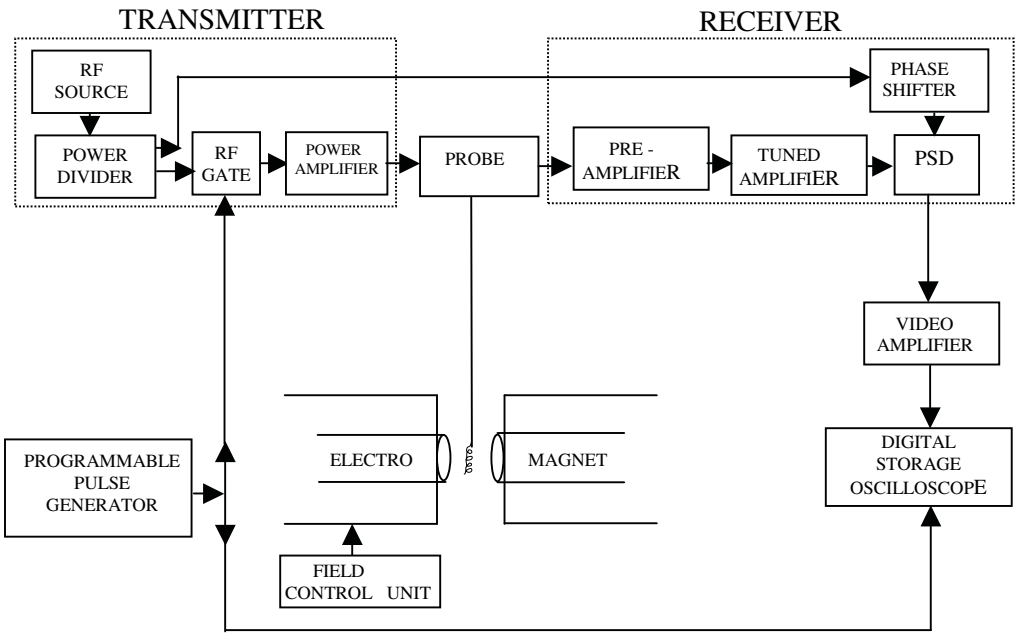

Figure 2.12 Block diagram of the home built pulsed NMR spectrometer.

The minimum requirements of a pulsed NMR spectrometer are as follows:

1. A pulse programmer to provide necessary pulse sequences.
2. A transmitter (power amplifier) capable of delivering short (1-20 μs) powerful (100 -1000 V) rf pulses. The rf pulse should have short rise and fall times (< 0.2 μs, typically).
3. A matching network (probe) to match the transmitter to the sample coil and the sample coil to the receiver.
4. A receiver (~ 80 dB gain) capable of recovering quickly (~ 10 μs or less) from transmitter overloads.
5. A signal averaging instrument to improve the signal to noise ratio and to measure the FID amplitude.

2.3.1 PC BASED PROGRAMMABLE PULSE GENERATOR (PPG)

Many pulsed NMR spectrometers have been described in the literature [18-21]. Some of them employ microprocessors for pulse sequence generation and data acquisition. Early pulsed NMR spectrometers employed a rather complicated digital pulse sequence generator using a large number of digital IC's. The pulse widths and delay between the pulses were set by thumb working screws. Later when microprocessors became available, microprocessor based pulse programmers were used. The sequence parameters were set by the assembly language programming. Microprocessor based pulse programmers are cumbersome to use and not very handy for operation. Programmable Pulse Generator (PPG) built around Intel microprocessor peripheral 8253 without using a controlling microprocessor has also been used some times [22]. With the availability of fast

computers and add on cards, the complexity of the pulse programmer has now been reduced to a single board. We have used a programmable pulse generator built using a PCI DIOT card.

PCI DIOT 48 digital input output card manufactured by Electro Systems Associates Pvt. Ltd. is used in the present work. It is a PCI based digital input / output timer card for IBM compatible Computers [23]. This card contains two 8255 programmed peripheral interface (PPI) which provide 48 programmable I/O lines and one 8253 programmable interval timer with 3 programmable counters/timers. The card can be plugged into any one of the free PCI slots of the system. The card was installed using a driver provided with the card.

The component layout of the PCI DIOT card is shown in Figure 2.13. The card uses a PCI Bridge (U8) to interface two 8255's at U5 & U6 and one 8253 at U3 to the PC through PCI Bus. The two 8255's provide six programmable 8- bit I/O ports. The 24 I/O lines of U5 are brought to J2, a 26-pin berg connector. The 24 I/O lines of U6 are brought to J3, a 25-pin D-Type connector and also to J4, a 26- pin berg connector. The 74LS245 at U9 is a Bi-directional buffer for data bus. The Programmable Interval Timer (PIT) 8253 at U3 has three 16-bit programmable timers/counters and can operate up to 2.0 MHz. We have replaced this 8253 by 8254 to operate the timer at higher frequency (up to 8 MHz). The OUT, GATE and CLK lines of the PIT are brought to J1, a 15-pin D-Type connector. The jumpers JP1, JP2 and JP3 can be used for connecting external or system clock to the clock inputs of timers of 8254. In the present work, we have used system clock for both Timer 0 and Timer 1 and the jumpers JP2 and JP3 are used for connecting required system clock to the clock inputs of timers of 8254. The GATE 0, GATE 1,

GATE 2 signals of the 8254 are user controllable. For the Timer 0, the system clock frequency divided by 16 (i.e., 2 MHz) is used to get the required different pulse sequences.

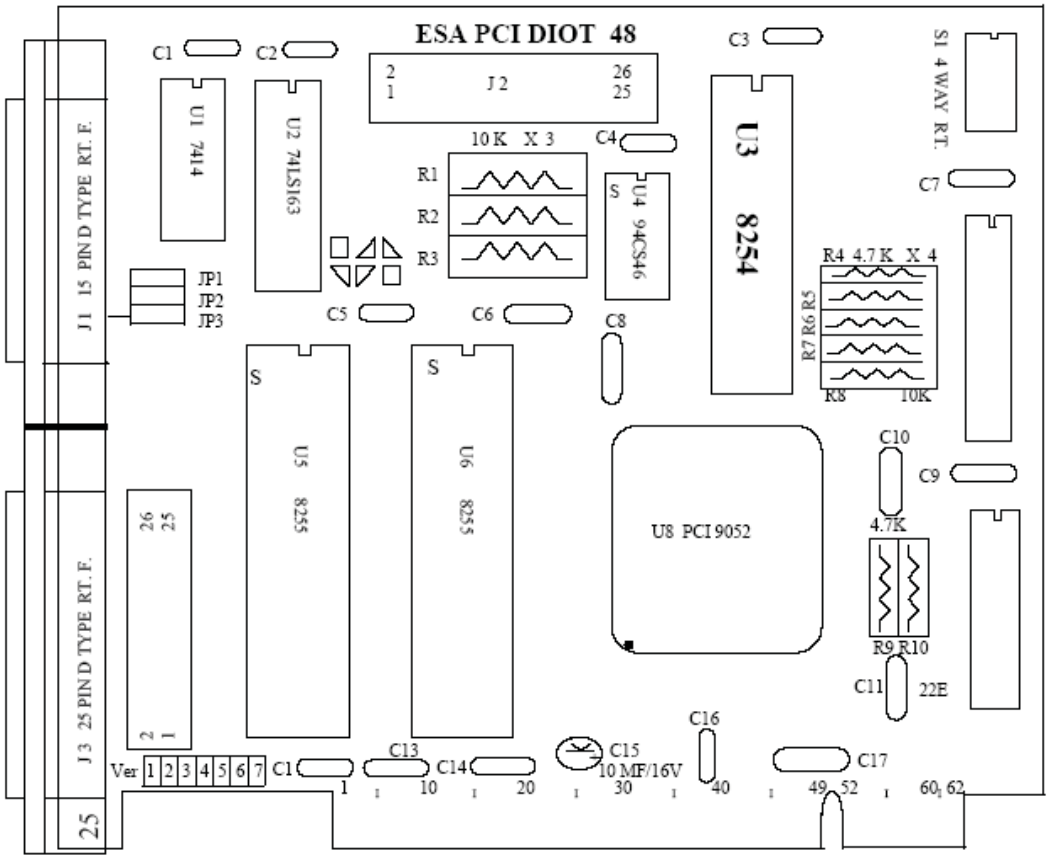

Figure 2.13 The component layout of the PCI DIOT – 48 card.

In the present PC based PPG, we have generated four types of pulse sequences (as shown in Fig. 2.14), and the timer is programmed for one type of sequence at a time. For the Timer 1, the system clock frequency divided by 8 (i.e., 4 MHz) is used to get the triggering pulse, which is required to trigger the Digital Storage Oscilloscope (DSO) for data acquisition. This triggering pulse would start at the end of the last pulse, i.e. at the end of the second pulse in the two pulse sequence, at the end of third pulse in the three

pulse sequence, at the end of monitoring pulse in the saturation burst sequence. The pulse width, the delay between the pulses, and the repetition time of the sequence are all independently programmable. Both the timers 0 and 1 are programmed in Mode 0 using 'C' language to generate the required pulse sequences along with the triggering pulse. The timer 0 output gives the pulse sequences which are used for rf mixer and the timer 1 output, which gives the triggering pulse is used for DSO triggering.

A program written in 'C' is employed for generating the required pulse sequences (given in the Appendix 2). The pulse widths are variable from 1 μs to 127 μs, the delay between the pulses are variable from 1 μs to a few seconds and the repetition time of the sequence is variable from 1s to several tens of seconds. The rise and fall times of the pulses are even less than 10 ns. This PPG is easily programmable even for other complex pulse sequences.

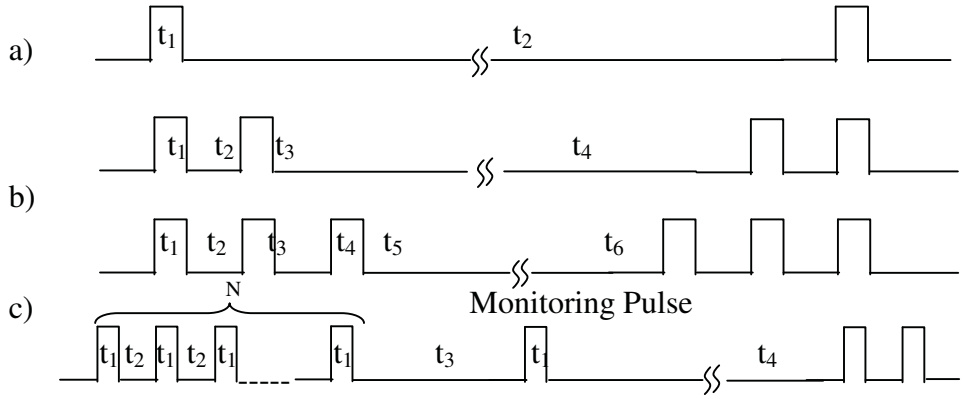

Figure 2.14 Schematic representation of the different pulse sequences (a) Single pulse (b) Two pulse (c) Three pulse and (d) Saturation burst sequences.

Buffer circuit

To have a good transfer from RF to LO ports in the DBM (Double Balanced Mixer), about a 40 mA current is required. So the PPG output has to be buffered to drive the DBM. We have used 74LS128 I C as the current buffer, which is a quad dual input NOR buffer and can source or sink more than 40 mA of current. The schematic diagram of the buffer circuit is given in Fig. 2.15.

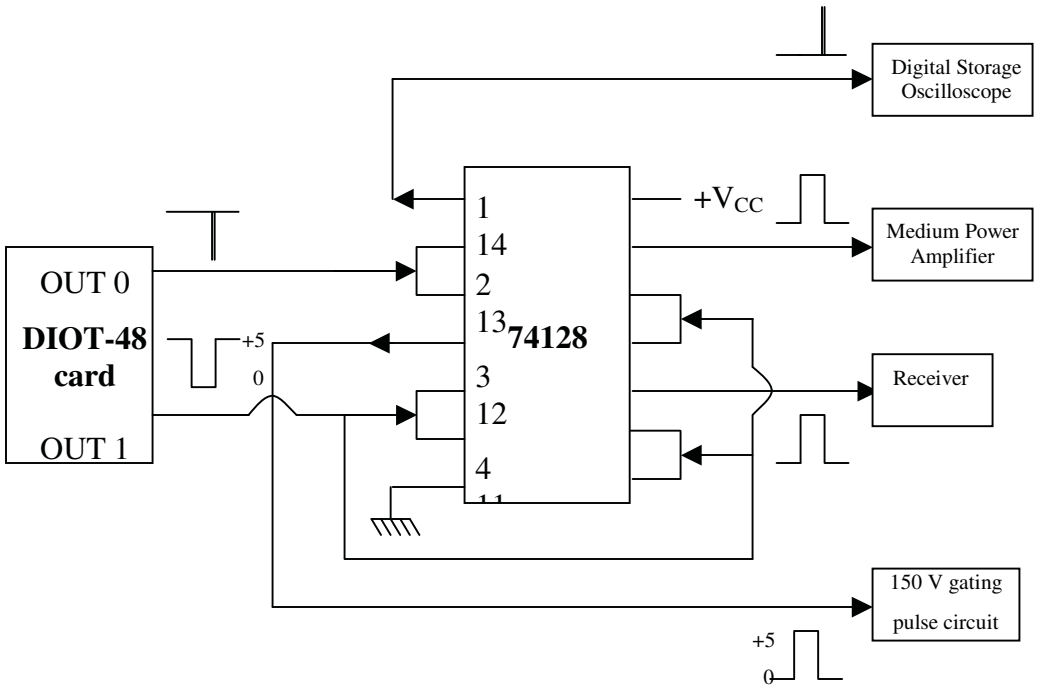

Figure 2.15 Schematic representation of the buffer circuit.

2.3.2 Transmitter

The block diagram of the gated transmitter is given in Fig. 2.16. The gated transmitter has three stages (i) the rf gate (ii) the medium power amplifier and (iii) a high power amplifier.

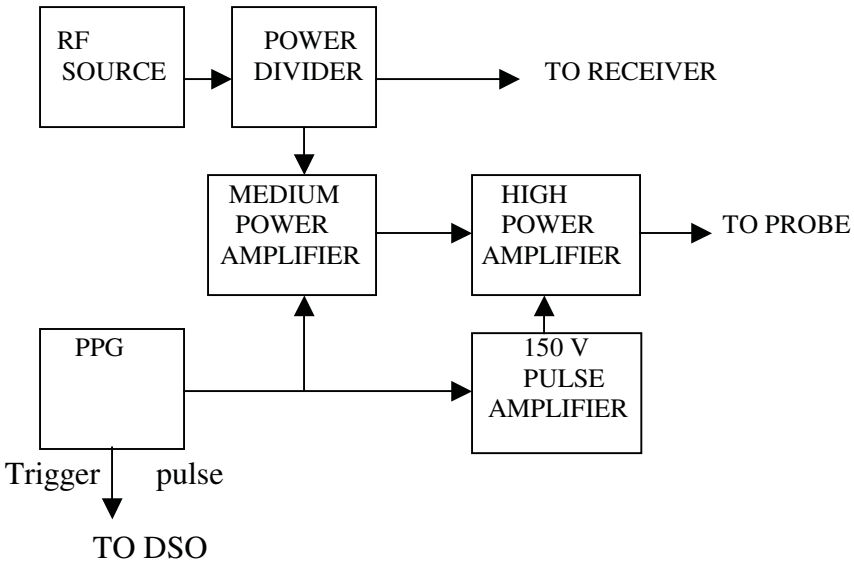

Figure 2.16 Block diagram of gated transmitter.

2.3.2.1 The RF unit

The rf unit consists of a signal source (Systronics standard signal generator, Model 1103) capable of working between 1-72 MHz. The rf signal is amplified by a wide band amplifier (United Systems AH-520, 1-100 MHz) and is given to a power divider (NH 50-201 RA) which gives two in-phase isolated (50 dB) outputs. One of these outputs is used as the rf input to the transmitter and the other as the reference for the phase sensitive detector. The output from the rf unit is gated and power amplified before coupling to the sample.

2.3.2.2 Medium Power Amplifier

A DBM (United systems, Model UDM IC /2K) and a medium power amplifier (United systems, Model RF UTX 1-100) are used for gating and initial amplification of the gated rf to a voltage of about 20-30 Vpeak-peak ($V_{p\text{-}p}$) into 75 ohms. These units are custom built to our specifications. The block diagram of the medium power amplifier is given in the Fig. 2.17.

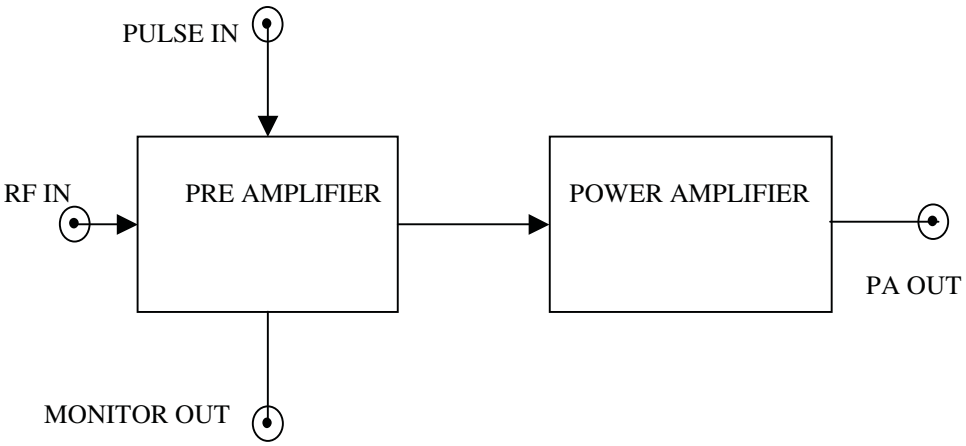

Figure 2.17. Bock diagram of medium power amplifier.

Double Balance Mixer (DBM)

DBM is used for mixing of the RF with the dc pulses from the PPG. DBMs have become a standard component in communication systems, NMR spectroscopy, microwave links etc. If used properly, DBMs allow system designers to achieve minimum distortion with a high degree of isolation from interfering signals [24].

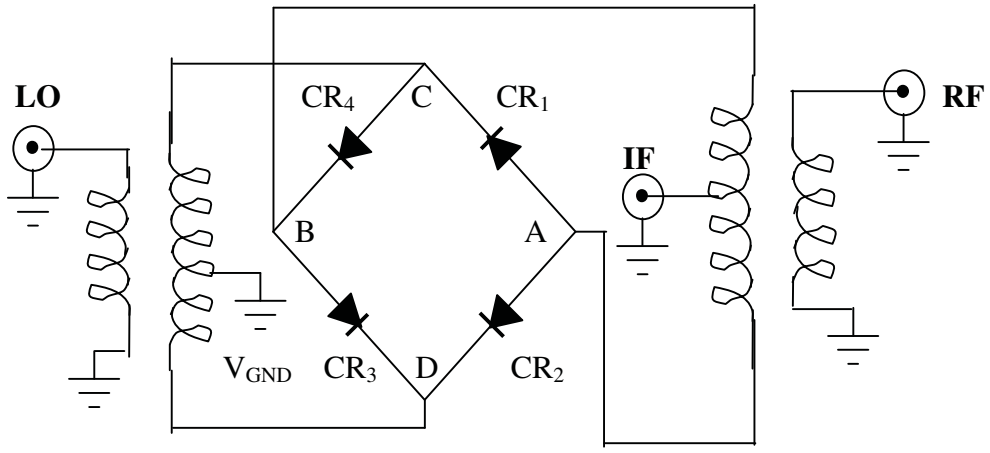

Figure 2.18. Schematic representation of a typical DBM.

Figure 2.18 is a schematic representation of a typical DBM. The three ports of the mixer are generally named as Local Oscillator (LO) port, the Radio Frequency (RF) port and Intermediate Frequency (IF) port. The LO port is the transformer coupled port whose transformer secondary is signal grounded. The RF port is the transformer coupled port whose transformer secondary is center tap and is used as the IF port. DBM works in any combination of signals and ports but the IF port is the only one, which will go to DC. If CR_1, CR_2 and the LO transformer are symmetrical, then the voltage at point A is same as the center-tap of the transformer, which is at ground. Similarly if CR_3 is equal to CR_4, the voltage at B is the same as V_{GND}. Therefore, there is no voltage across A and B and hence, no voltage across the RF or IF port. Thus the isolation among LO, RF and IF ports is obtained. If CR_4 is equal to CR_1 and CR_2 is equal to CR_3, the voltage at C will be equal to that at D. There will be no voltage difference between C and D and thus no RF will appear at the LO port. Similarly, it can be seen that voltage at the IF port is the same as the voltage at C and D, i.e., zero; thus there is no RF output at the IF port. Since the IF port is DC coupled to the diodes, the DBMs can be used as high-isolation fast switches. Typically, 10 to 20 mA current will change the insertion loss between LO and RF to as low as 3dB or less. We have used this feature to generate pulsed RF from a Continuous wave RF. The gated RF (mixed RF) of $5V_{peak\text{-}peak}$ is amplified by using the medium power amplifier to 20 $V_{peak\text{--}peak}$ in to 75 ohm load.

2.3.2.3 High Power Amplifier

The output of the medium power amplifier is further amplified by a rf amplifier using a National Electronics 3E29 dual tetrode working in the push-pull configuration as shown in Figure 2.19. Since the push-pull amplifier has an input impedance of 600

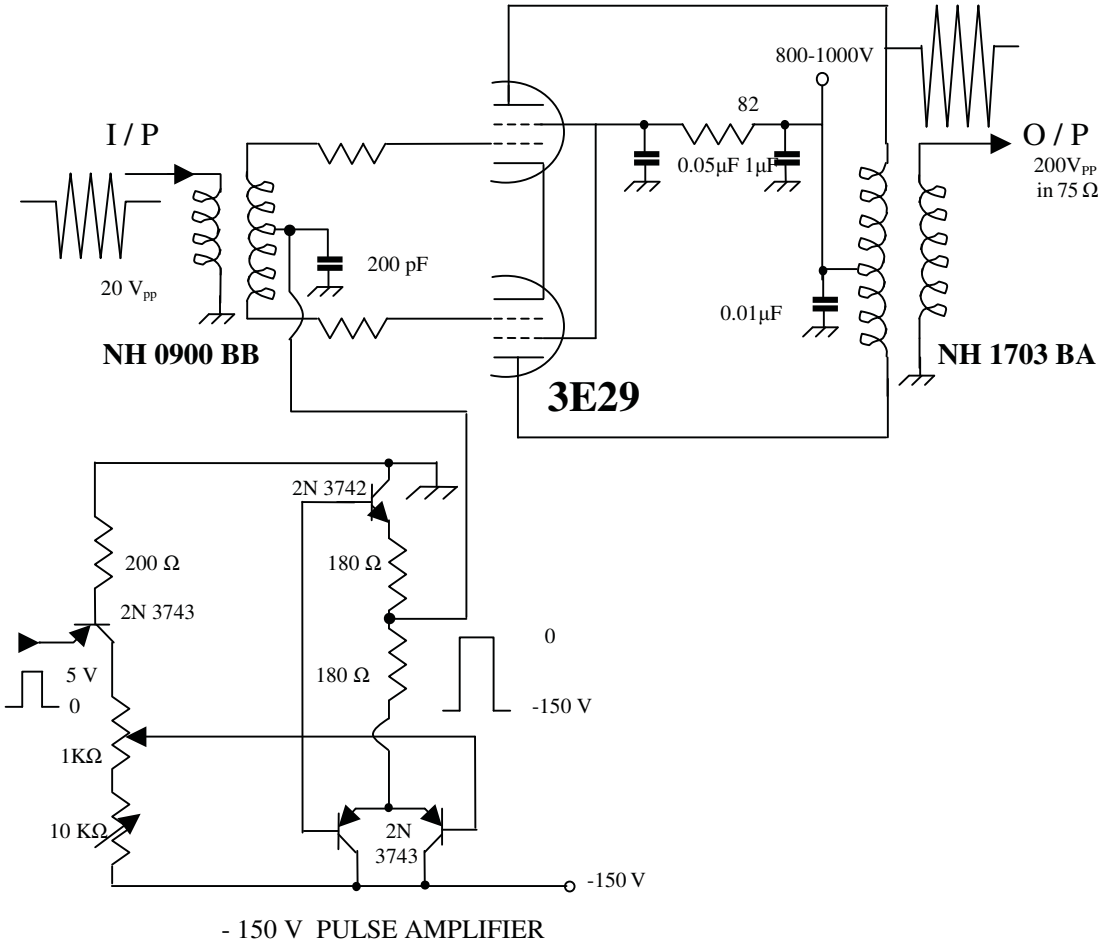

Figure 2.19 High Power Amplifier.

ohms, the grids are gated through the wide band transformers North Hills NH 0900 BB (100 KHz – 30 MHz) by the synchronous pulses, which are amplified by a pulse amplifier. The pulse amplifier coverts the TTL output from the PPG buffer and switch the grid biasing voltage from 150 V to the conducting region during the pulse ON period. The output of the push-pull amplifier is taken through another wide band transformer (North Hills NH 1703 BA) having the output impedance of 75 ohms. The transmitter rf pulse is variable from 100-300 Vp-p.

2.3.3 NMR probe Circuit

The most important part of the pulsed NMR spectrometer is the matching network (probe), which couples the power from the transmitter to the sample coil (where sample containing nuclear spins is placed) during pulse ON period and converts the precessing magnetization into a detectable signal at the input of the receiver immediately following the pulse. The probe should also decouple the receiver from the transmitter during the pulse ON period. We have used two matching circuits (1) Series tuned LCR network and (2) Parallel tuned LCR network in the present studies, where a single coil is used as a transmitter and receiver [25]. The single coil series tuned LCR network is simpler and has several advantages over other networks [26] described in the literature, in terms of maximum power efficiency. Crossed diodes and $\lambda/4$ transmission lines which appear as short circuit to high voltages and open circuit to the small signals section is used to protect the receiver from transmitter pulse overload.

2.3.3.1 Series resonant circuit

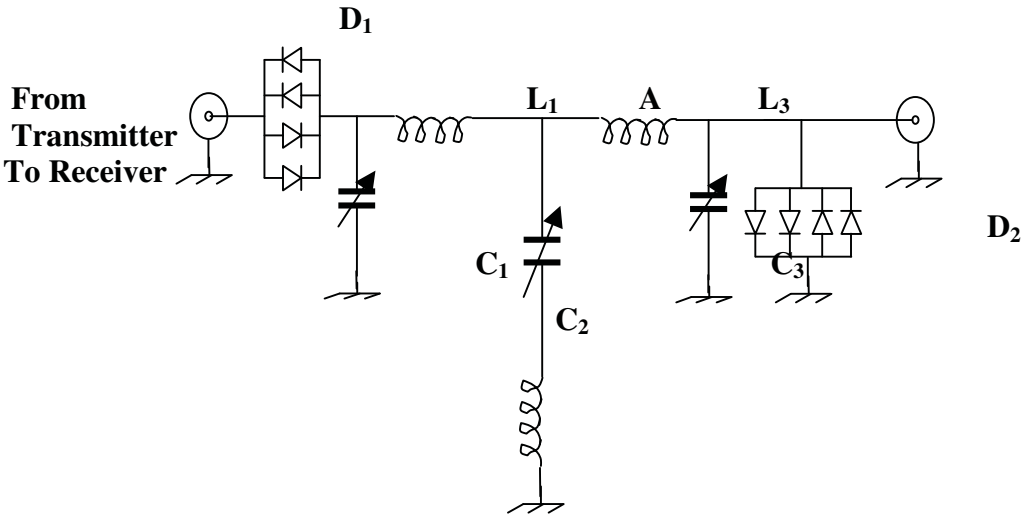

Figure 2.20. Series tuned parallel matched probe.

This matching network (Figure 2.20) consists of three resonant circuits: the transmitter output circuit (L_1, C_1), the sample coil circuit (L_2, C_2) and the receiver input circuit (L_3, C_3). Each resonant circuit is tuned independently to the Larmor frequency.

The crossed diodes bank D_1 at the input act as a short circuit to the large amplitude transmitter pulses and an open circuit to the subsequent very small Free Induction Decay (FID) signal voltages induced in the coil L_2. The series combination L_2C_2 represents a low impedance path in parallel with that of L_3C_3, so that the entire transmitter voltage is dropped across L_2 and a very little voltage is fed into the receiver section during pulse ON period. Moreover, since another crossed diode bank (D_2) represents short circuit to ground, the voltage at A is dropped across L_3 before reaching the receiver. After the transmitter pulse, D_2 acts as an open circuit to the low voltage induced resonant signals, thereby forcing the signal into the receiver through L_3C_3 pair. Thus, the circuit ensures an efficient transfer of power from the transmitter to the sample coil and also a good protection of the receiver from destructive overloads.

2.3.3.2 Parallel resonant circuit

The parallel resonant circuit given in Fig. 2.21, consists of a series resonant tank circuit (L_1C_1), in series with a capacitor C_2. The function of the crossed diodes is similar as in the case of series resonant circuit described in the earlier section. In addition, the presence of the quarter wave network before the diode pair offers high impedance for transmitter pulses thus protecting the receiver from further overload. The input and output impedances of the tuned coil is chosen to be equal to 50 ohms. C_2 provides transformation of the high impedance parallel resonant circuit to a lower impedance (50 ohms) to match the output impedance of a transmitter and the input impedance of the

receiver. C_2 is chosen to be as small as possible in order to minimize the degradation of the L/C ratio and in turn the quality factor Q of the circuit. The conditions for tuning the circuit are given in the literature [26].

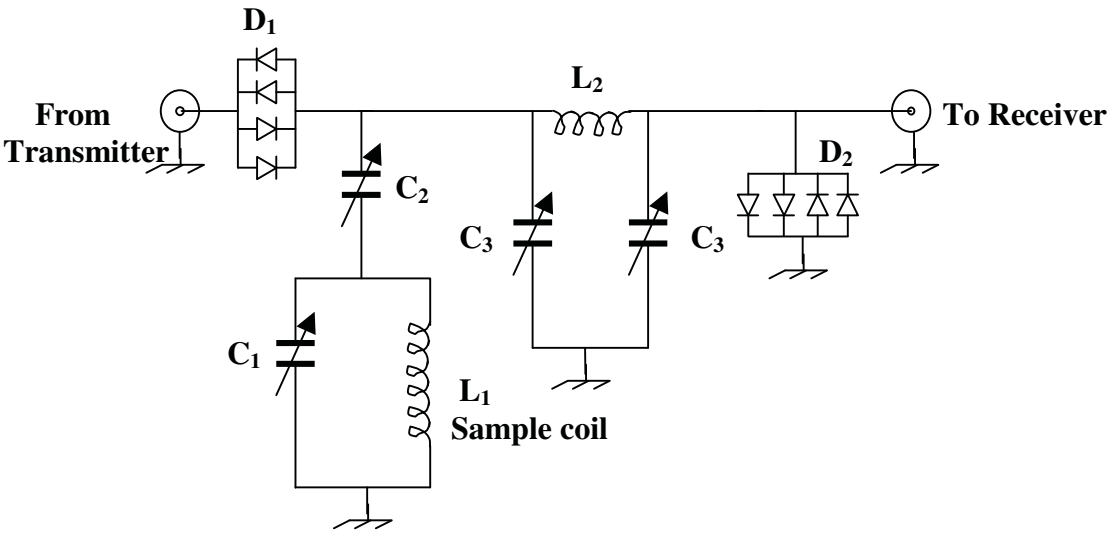

Figure 2.21 Parallel tuned series matched probe.

The λ/4 circuit acts as a impedance transformer network. The circuit, which consists of an inductor L_2, and two capacitors C_3 (connected as a π section) are chosen to offer an impedance of 50 ohms at the designed frequency. Tuning the capacitor C_3 maximizes the signal strength.

2.3.4 Receiver

For pulsed NMR application a receiver should be of variable high gain, low noise, fast recovery and must produce stable gain and low distortion over the working frequency. Since the NMR signal picked up by the sample coil is very weak (~ microvolts), the detection circuit should have fast recovery time and be very sensitive. There are several designs available in literature [19, 27-30]. The block diagram of the receiver used in the present investigations is given in Fig. 2.22. The receiver unit consists of a low noise

preamplifier (LNA), a wide band amplifier, a phase sensitive detector and a video amplifier. A receiver amplifier with a total gain of about 80 dB and recovery time of about 2 μs, custom built to specification by United System Engineers Pvt. Ltd. is used for the present investigations.

The NMR signal from the probe, connected through the rf IN port of the receiver, gets amplified through a low noise amplifier (LNA) followed by high pass filters (HPF). Then it goes through several stages of attenuators. The input stage step attenuators are employed in the circuit to avoid the overloading of the receiver when the signals are strong and thus boost the signal handling capacity. Since the noise power of an amplifier is proportional to the bandwidth, appropriate stage filters are used to reduce the bandwidth. However, signal drift, low sensitivity to the component tolerance and some times the physical size of the components restrict the achievement of good bandwidth narrowness of the filters. Phase Sensitive Detection (PSD) technique can be used for this purpose as it permits extremely narrow bandwidth (~1.001 Hz) and has the advantage of rejecting discrete frequency noise. For some experiments we have also used a MITEQ receiver (Model AU-1447-BNC) amplifier, which has wide bandwidth of 0.3 – 200 MHz with gain of 56 dB.

Phase Sensitive Detector

After initial amplification, the signal is synchronously detected using the reference signal. A double balanced mixer (DBM) is used as the PSD. The circuit diagram of the DBM is given in Figure 2.18. The signal is fed to the RF port, the reference RF (from the power divider) is connected to the LO port and the detected output signal is taken through the IF port.

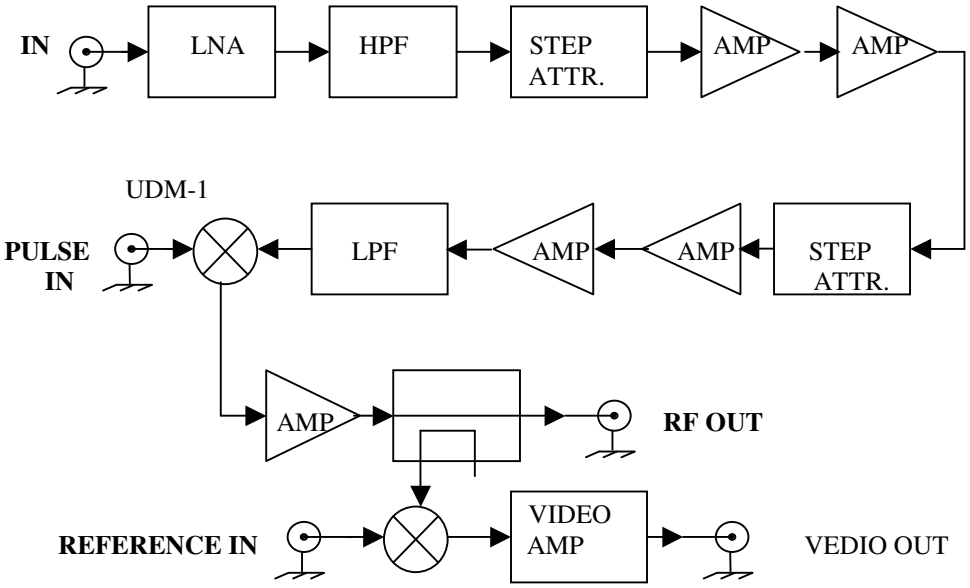

Figure 2.22 The block diagram of the receiver.

It is known that the detected signal has other frequency components along with the dc component. A RC filter is used to filter the noise and other unwanted components in the signal. A digital storage oscilloscope (Agilent, Model 54622A, 100 MHz, 200 samples/s) is used for averaging and hence for the measurement of the amplitude of the FID signal.

2.4 Temperature variation setup

2.4.1 High temperature assembly (300 -410 K)

Two heating elements of 75 ohms in the form of soldering tips are inserted to the attachment of the sample coil. These two heating elements are connected to the variable transformer (0 - 240 V, 4 A). Figure 2.23 shows the high temperature setup. By varying the voltage to the heating elements, the temperature of the sample can be varied from 300 to 430 K. This is indirect heating and hence the ac pickup noise is avoided and the sample

gets heated uniformly. A double walled high vacuum glass dewar is used to cover the sample (closed at one end) which helps in maintaining the temperature. After setting the voltage for the corresponding temperature, sample attains the temperature in 45 minutes with accuracy better than ±1K. The Platinum -100 (Pt-100) sensor is used to monitor the sample temperature.

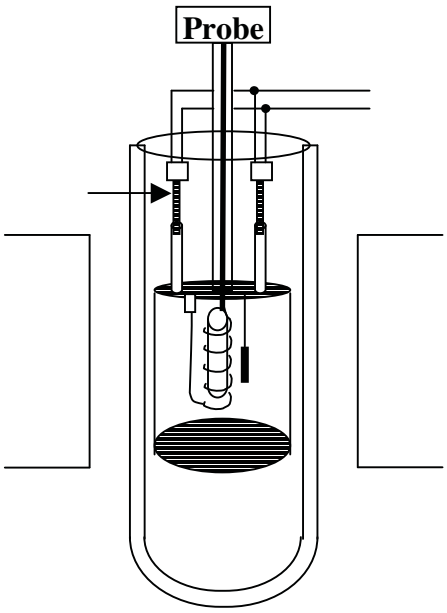

Figure 2.23 Variable temperature assembly (high temperature) (300 – 410 K).

2.4.2 Liquid Nitrogen Assembly (300-77 K)

A gas flow cryostat shown in the Fig. 2.24 is used for making low temperature experiments using liquid nitrogen as a coolant. The line width/second moment measurements are carried out as a function of temperature from 300 K down to 77 K using a wide-line NMR spectrometer described in the earlier section 2.2. The gas flow cryostat consists of a L shaped double walled silvered glass dewar and a straight double

walled silvered glass dewar. The two dewars are connected by ground glass joints. The silver coating of the dewar is done by Rochelle salt process. The dewars are evacuated to a pressure of about 10^{-5} Torr and sealed. The sample is kept inside the L shaped dewar and positioned at the center of the pole pieces of the magnet. The liquid nitrogen is boiled off by a heater coil immersed in a 55 liter stainless steel storage dewar using a dimmerstat. By varying the voltage applied to the heater, the rate of flow of liquid nitrogen can be varied and hence the sample temperature is controlled with an accuracy of $\pm$ 1 K. Temperature from 300 to 150 K can be varied in this way. To vary temperature from 150 K to 114 K, cold finger technique is employed where the sample is covered with a brass cone and is dipped in the liquid nitrogen taken in the glass dewar. The 77 K data is obtained by directly immersing the sample tube in liquid nitrogen dewar. The Platinum-100 (Pt-100) sensor is used to monitor the sample temperature.

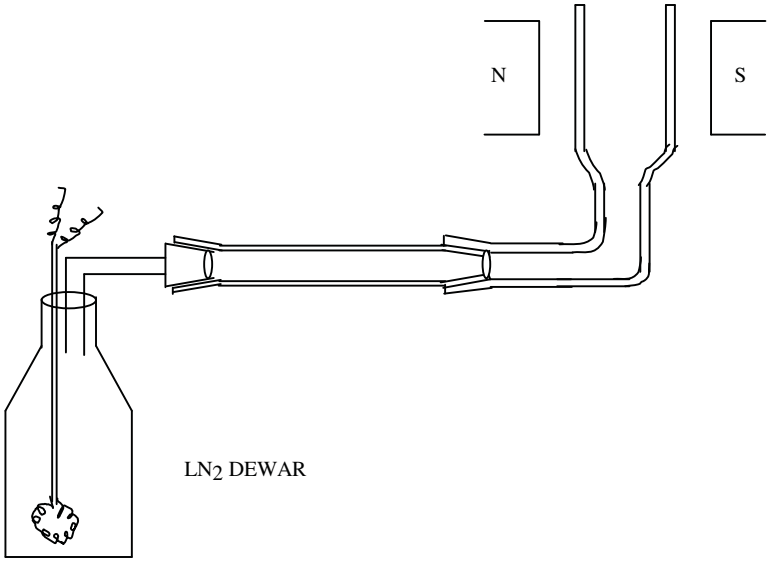

Figure 2.24. Variable temperature assembly using Liquid Nitrogen in the temperature range 300 -77K.

2.4.3 Liquid Helium Assembly (300 - 4.2 K)

To make measurements below 77 K, a liquid helium assembly is employed. The liquid helium assembly consists of a continuous flow cryostat (CF200, Oxford Instruments), a gas cooled transfer tube (GFS 300, Oxford Instruments), temperature controller (ITC-503, Oxford instruments), flow control console (VC31, Oxford Instruments) and a gas flow pump (GF3, Oxford Instruments).

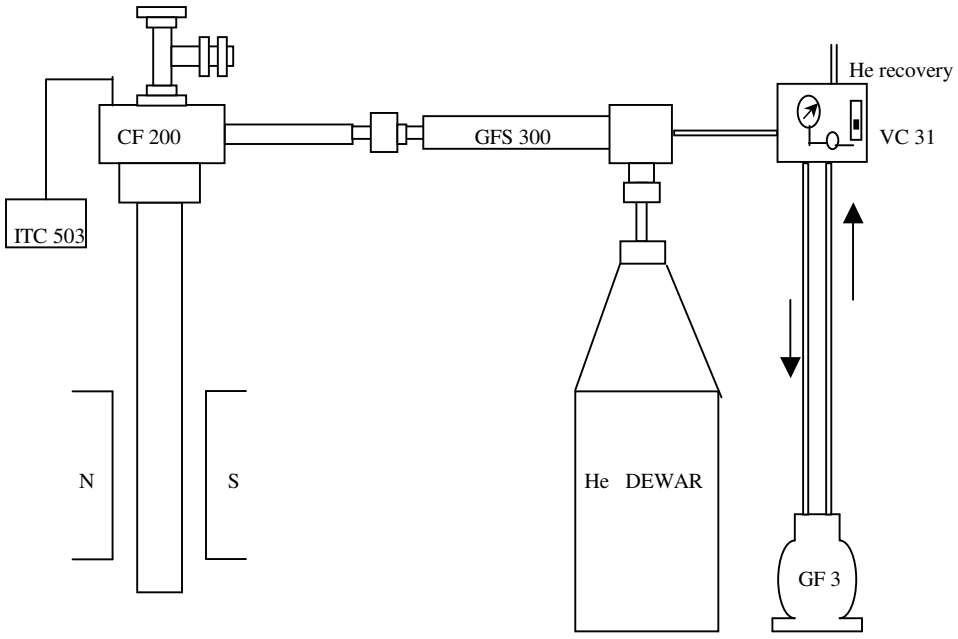

Figure 2.24. Variable temperature assembly using Liquid Helium in the temperature range 300 - 4.2 K.

The continuous flow cryostat is used for controlled transfer of helium from the storage vessel to the cryostat. The sample is top loaded into the cryostat (25 mm inner bore) sample chamber. The sample chamber is initially evacuated to rotary vacuum and the sample chamber is connected to the helium gas recovery line. Here, helium gas acts

as exchange gas and keeps the temperature of the sample uniform. The temperature-controlled region extends up to 10 cm from the bottom of the sample space. The sample coil is connected to the probe through a seamless thin walled SS tube (high thermal resistance, high electrical conductivity) to keep the evaporation of the coolant very low.

Coolant is delivered to the cryostat by the vacuum-insulated transfer tube (GFS300) inserted into the siphon entry arm. The helium return line from the transfer tube is connected to a gas flow pump (GF3, diaphragm pump) through the flow control console (VC31). The gas flow pump creates a slight pressure difference between the cryostat and the helium storage vessel, thus sucking the helium into the transfer tube. The coolant cools the sample space via heat exchanger and returns back to the siphon entry arm where it enters the transfer tube. A PTEF seal on the transfer tube ensures effective sealing between the entering and exhausting stream of gas. The exhausting gas is recovered into the recovery line as the gas flow pump pushes it. The temperature of the sample is controlled using Intelligent Temperature Controller (ITC) (Oxford Instruments, model 503), which regulates the power fed to a heater provided at the bottom of the cryostat.

References

1. Bloch F, Hansen WW and Pakard M. *Phys. Rev*., **70**, 474 (1946).
2. Purcell EM, Torrey HC and Pound RV. *Phys. Rev*., **69**, 37 (1946).
3. Bhat SV, Amit Rastogi and Sudershan YS., *Solid State Commu.,* **89(7)**, 633 (1994).
4. Kavun VYa, Gerasimenko AV, Slobodyuk AB, Didenko NA, Uvarov NF and Sergienko VI. *Russ. J. Electrochemistry*. **43 (5),** 537 (2007).
5. Kavun VYa, Sergienko IVI and Uvarov NF. *J. Struct. Chem*., **44(5),** 796 (2003).
6. Rollin BV, *Rep. Prog. Phys*., **12,** 22 (1949).
7. Pound RV. *Phys. Rev.,* **72(6)**, 527 (1947a).
8. Hopkins NJ. Rev. Sci. Instrum., **20(6),** 401 (1949).
9. Andrew ER. Nuclear Magnetic Resonance (University Press, Cambridge, UK, 1958).
10. Pound RV and Knight WD. Rev. Sci. Instrum., **21(3),** 219 (1950).
11. Robinson FNH. J. Sci. Instrum., **36,** 481 (1959).
12. Abragam A. The Principles of Nuclear Magnetism (Oxford University Press, Oxford, UK, 1961).
13. John E.Wertz and James R. Bolton, *Electron Spin Resonance-Elementary theory and Practical applications* (Chapman & Hall, 1986).
14. Sasidhar N, Mallikarjunaiah KJ and Damle R. *J. Instrum. Soc. India*. **32(1)**, 1 (2002).
15. PCL –207 User's Manual, Dynalog (India) Limited, 1996.
16. Gutowsky HS, Pake GE and Bersohn R. *J. Chem. Phys.,* **22(4),** 643 (1954).
17. Ernst RR and Anderson WA. *Rev. Sci. Instrum.,* **37(1)**, 93 (1966).
18. Khol LD and Veillet P, *Rev. Sci. Instrum*. **45(6)**, 759 (1974).
19. Karlicek RE (Jr)., and Lowe IJ, *J. Mag. Reson*., **32**, 119 (1978).

20. Shenoy KR, Ramakrishna J and Jeffrey KR, *Pramana*, **14**, 363 (1980).

21. Ader RE, Lepley AR and Sanngio DC. *J. Mag. Reson.,* **29**, 105 (1978).

22. Ramanuja MN and Ramakrishna J. *Ind. J. Pure and Applied phys.,* **31**, 375 (1993).

23. ESA PCI-DIOT card, User's Manual, 2000.

24. Mini-circuits Division of Scientific components, Broklyn, NY. *RF/IF designer's handbook* (1992).

25. Gilbert Clark W and McNeil JA. *Rev. Sci. Instrum.,* **44(7)**, 844 (1973).

26. Fukushima E and Roeder SBW. *Experimental pulse NMR: A nuts and bolts approach* (Addison- Wesley Publishing Company Inc., Massachusetts, 1981).

27. Gilbert Clark W. *Rev. Sci. Instrum.,* **35(3)**, 316 (1964).

28. Lowe IJ and Tarr CE. *J. Phys. E: Sci.Instrum.,* **1,** 320 (1968).

29. Addci DJ, Homung PA and Torgeson DR. *Rev. Sci. Instrum.,* **47(12)**, 1503 (1976).

30. Hoult DI. *Prog. NMR. Spectrosc.,* **12**, 41 (1978).

Chapter 3

NMR Studies in Diammonium Hexafluorozirconate $(NH_4)_2ZrF_6$

3.1 Introduction

NMR is one of the most powerful local probes to investigate mobility and internal motions in solids and is therefore used to study molecular dynamics, (i.e., determination of associated correlation times (τ_c) and activation energies (E_a)), phase transitions (if any) and mobility of conducting species in variety of inorganic solids. The temperature dependence of the spin lattice relaxation time gives information on the dynamics of the molecular groups present. The theory developed by Bloembergen, Purcell and Pound, known as BPP theory [1] has been quite successful in explaining the observed spin lattice relaxation time measurements. Many of the ammonium based inorganic solids exhibit superionic conduction. The diffusion of ammonium ions in these superionic solids is known to be a major contribution to ionic conductivity. Our interest is to study ammonium ion dynamics in these compounds using NMR second moment and spin-lattice relaxation time (T_1) measurements. Different types of motion like the reorientation, torsional oscillations, the spin rotation [2], diffusion [2-4], tunnelling [5-9], etc., are observed at different temperature ranges. Deviations in the T_1 behaviour from the BPP theory indicate relaxation mechanisms other than molecular reorientational dynamics. For example, quantum rotational tunnelling process is invoked to explain T_1 results in $(NH_4)_2PtBr_6$ [10-12] and order- disorder effects in NH_4Cl [13]. tunnelling has been invoked to explain multiple T_1 minima [5,14,15] and additional sidebands [5] at low temperatures in many ammonium compounds.

Ammonium salts of the type A_2BX_6, (A = NH_4, N $(CH_3)_4$ etc, B = Se Pt, Pb, Te, Sn, Ti and X = Cl, Br, I) with antifluorite structure, consists of a large anion compared to the cation, which is not highly charged. It is found that the ammonium ion performs

isotropic reorientation about the symmetry axes and contributes to the ^1H spin lattice relaxation through the intra molecular dipole- dipole interaction [16-17]. In these compounds, the motion of the NH_4 ion is hindered by a low potential barrier (0.6 - 4.0 kcal/mol) [18] and the activation energy increases with decreasing lattice dimension [19]. The cations, like NH_4, $N(CH_3)_4$ etc. in these compounds, occupy the spacious cages formed by MX_6^{2-} octahedra located at the corners and the face centers of the cubic structures resulting in low activation energies. Proton magnetic resonance in systems like NH_4Br, NH_4I, NH_4SCN, $(NH_4)_2CrO_4$ and NH_4NO_3 at 1.8 K gives evidence of quantum mechanical tunnelling [5]. Proton spin lattice relaxation behaviour of ammonium ion in $(NH_4)_2GeF_6$ at 8 MHz below 15 K is explained by quantum tunnelling [14]. T_1 studies at low temperatures, in various deuterated compounds are also explained by tunnelling. Study of quantum tunneling in various compounds using inelastic neutron scattering has been reviewed by Prager [20], while that using NMR has been reviewed by Srinivasan [21], Clough [22 - 24] and Horsewill [25 - 26]. The study of the absorption spectra and relaxation times of proton have given useful information on the tunnel splitting of NH_4 ion at low temperatures [5, 27 - 28]. It has been shown that the tunneling of NH_4 affects the spin lattice relaxation time (T_1) in various striking ways [29 - 32]: (1) observation of non-exponential relaxation, (2) multiple T_1 minima at low temperatures. Mechanism of the spin lattice relaxation at low temperatures is complicated because of the coupling between the librational mode of NH_4 ion and the phonon system.

Tuohi et al [33] have observed anomalous T_1 behaviour in $(NH_4)_2PbCl_6$ which are attributed to quantum tunneling. Svare [7] has developed a theory to explain the temperature dependence of average tunnel frequency in $(NH_4)_2PbCl_6$ in the range 15 to

40 K. He has found that very short life- time (2 ps) in the first excited torsional state of NH_4 as reason for temperature dependence of tunnel frequency. Temperature dependence of the average tunnel splitting (ω_t) of the ammonium ion in $(NH_4)_2PbCl_6$ has been determined as a function of temperature by observing the tunneling minima in proton spin lattice relaxation time which is found to vary from 47.6 MHz (at 4.2 K) to 12.5 MHz (at 50.6 K) [34 - 35]. Non-exponential recovery has been observed in the T_1 measurements in NH_4NO_3 below 20 K and spin conversion was observed below 4 K [36]. Proton T_1 and $T_{1\rho}$ have been studied by Svare et al [37] in powders of $(NH_4)_2MCl_6$ where M = Pd, Pt, Te, Ru, Ti, Ir and Re from 40 to 300 K. The activation energies E_a for NH_4 motion are found to lie in the range (0.6 – 4.5 kcal/mol) and E_a is a linear function of the lattice dimension for the cubic hexachlorides. These very extensive NMR investigations of the ammonium hexahalozirconates have suggested that it would be instructive to investigate Diammonium hexafluorozirconate (Ammonium zirconate), in which the reorientation of both cation and anion groups are present.

In the present study, proton and fluorine spin lattice relaxation time (T_1) measurements are undertaken in Ammonium ziroconate for the following reasons: (1) the two possible reorienting groups like NH_4 and ZrF_6 are well suited for NMR studies. (2) The importance of proton-fluorine dipolar interactions can be understood. Spin lattice relaxation time measurements, as a function of temperature would provide more reliable activation energies for the processes governing the relaxation in explaining the superionic conductivity and translational diffusion properties. Further Ammonium zirconate is a promising candidate for technological applications viz., in organometal catalyst compositions, to increase the polymerization activity with silica-gel supported

chromium oxide catalysts, as fluorinating agent, for curable resin composition, as an excellent corrosion resistant material and in making lithographic printing plates [38].

In the present study, commercially available ammonium zirconate from Aldrich Chemical Co., (39,729-6) is used directly without further purification. The compound is finely powdered and vacuum-sealed into glass ampoules of 5 mm diameter in helium atmosphere and then used for NMR measurements.

3.2 Earlier studies

Allan Zalkin et al have reported the room temperature crystal structure of Ammonium zirconate [39]. The crystal structure of Ammonium zirconate indicates that, it consists of Zr_2F_{12} units extended in infinite chains along the c-axis and ammonium ions are hydrogen bonded in a complex three dimensional network to these chains. Each Zr atoms are coordinated to eight F atoms. A triangle of three F atoms, at the center of the Zr_2F_{12} group, is sandwiched between two Zr atoms [39]. $(NH_4)_2ZrF_6$ has also been studied using wide line NMR, dc conductivity, IR, Raman and other techniques [28, 40-49]. The infrared and Raman active NH_4-vibrations in ammonium zirconate [40] are found to occur at relatively high wave numbers, which is characterized by moderate to weak hydrogen bonds [50]. Kavun et al [47] have estimated the activation energy for the transition of ions to local (diffusion) motions using the formula $E_a = 155\ T_c$ kJ/mol. T_c in this equation is taken to be the temperature (in Kelvin) of the beginning of the NMR spectrum narrowing or the appearance of a narrow component. Lalowicz et al [28] have carried out the proton NMR line shape calculation and analysis at 4.2 K for ammonium

zirconate and attributed their results to the tunneling rotations of the ammonium ion. Figure 3.1 shows the projection of the crystal structure of the ammonium hexafluorozirconate and the ORTEP plot. The characteristic parameters of ammonium hexafluorozirconate are given in Table 3.1.

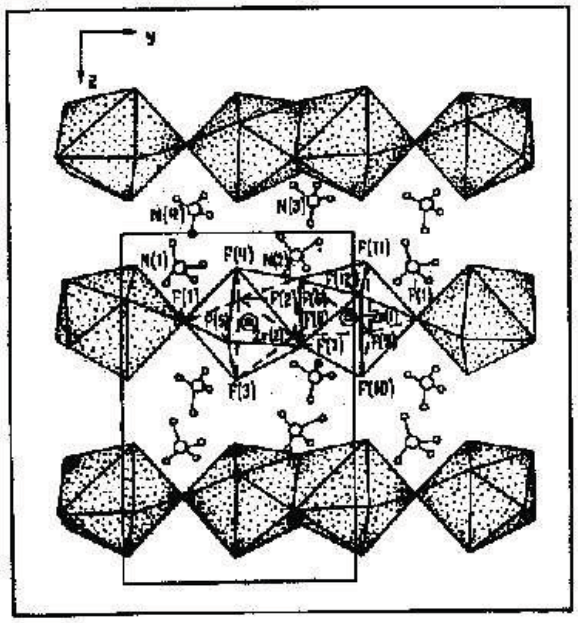

(a)

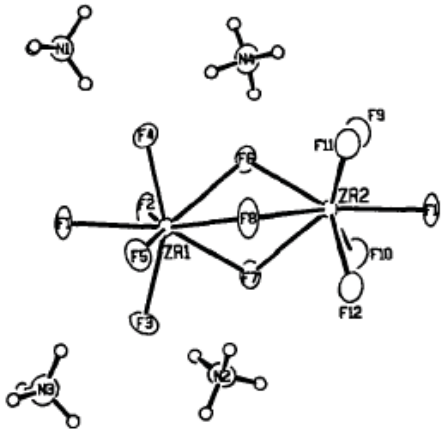

(b)

Figure 3.1 (a) Projection of the crystal structure of $(NH_4)_2ZrF_6$ on the yz-plane [41]. (b) ORTEP drawing showing the atomic numbering scheme. 50% probability ellipsoids are shown [39].

Table 3.1 Characteristic parameters of Ammonium zirconate [39]

Structure	Orthorhombic
Space group	$Pca2_1$
Cell dimension	a = 13.398 Å
	b = 7.739 Å
	c = 11.680Å
Density	2.65 g cm^{-3}
Zr-F (1)	2.02 Å
Zr-F (2)	2.343 Å

3.3 Results and discussion

Spin lattice relaxation time

Figure 3.2 shows the variation of ^{1}H and ^{19}F NMR spin lattice relaxation times (T_1) at 21.34 MHz with inverse temperature (1000/T) over the entire temperature range studied. The magnetization recovery profiles for both the nuclei (^{1}H and ^{19}F) are found to be exponential within experimental errors throughout the temperature region studied.

3.3.1 Analysis of ^{1}H NMR T_1

At room temperature, T_1 value is about 38 ms and on increasing the temperature, T_1 starts decreasing up to 395 K, above which it reduces sharply to less than a millisecond. In the same temperature region, FID duration also increases several times as the temperature is increased from 388 K to 410 K. On decreasing the temperature from room temperature, initially T_1 increases and shows a maximum of about 48 ms around 240 K. Below 240 K, T_1 decreases and follows through a minimum of about 6.6 ms around 160 K and

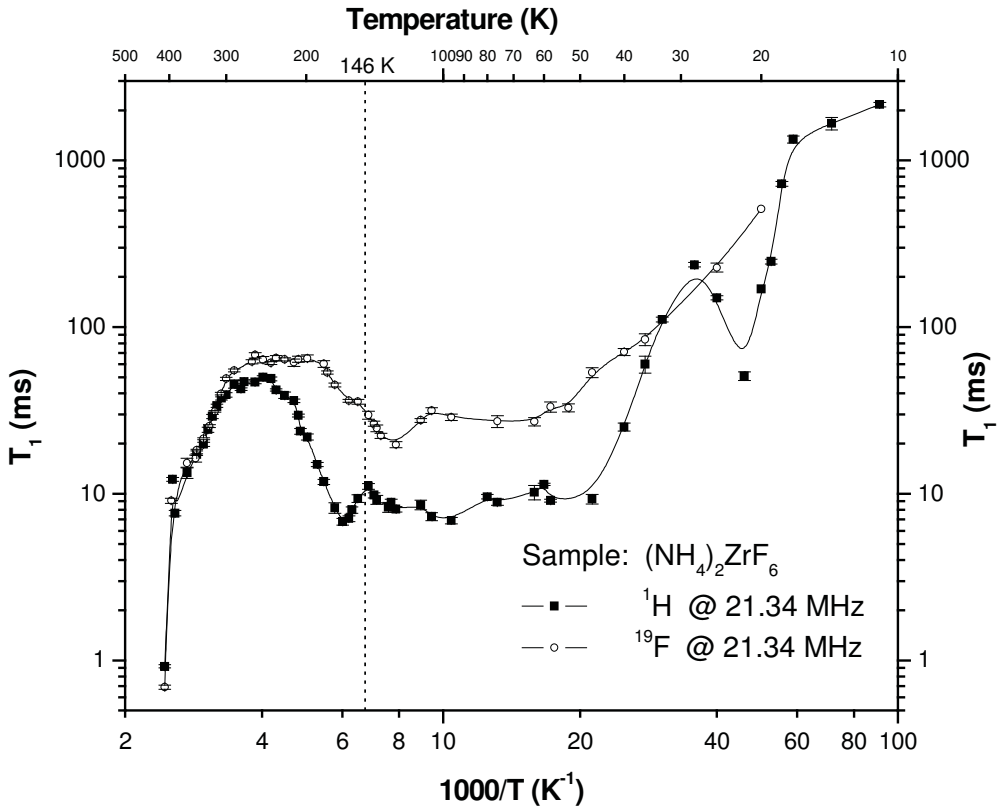

Figure 3.2 ^{1}H, ^{19}F NMR T_1 data at 21.34 MHz (with error bars) of Ammonium zirconate in the entire temperature range studied. The solid line is guide to the eye.

then increases to about 11 ms at 146 K. Below this temperature, T_1 decreases to about 8.8 ms and remains constant (within experimental error) till about 50 K. Below 50 K, T_1 again increases and below 30 K, it shows another minimum of 51 ms around 22 K. Below 20 K, T_1 increases monotonically to a few seconds till the lowest temperature of measurement (11 K) in the present investigation. The T_1 data are analyzed in three parts: the High Temperature (HT) region (410 - 240 K), the Intermediate Temperature (IT) region (240 - 146 K) and the Low Temperature (LT) region (146 – 11 K).

3.3.1.1 High Temperature (HT) region (410 - 240 K)

Before the T_1 analysis, we present some details of second moment studies [41] of both proton and fluorine for better comparison as shown in Fig. 3.3 in the same compound Ammonium zirconate. In the temperature region 135-290, the ^1H NMR spectra of Ammonium zirconate showed a single and comparatively broad line [41]. Above 295 K, a narrow component appears in the center of the spectrum and the second moment also decreases to 2.3 G^2 from 5.5 G^2. Above 370 K, ^1H NMR line width starts decreasing and finally reaches to a negligible value (0.15 G) around 400 K.

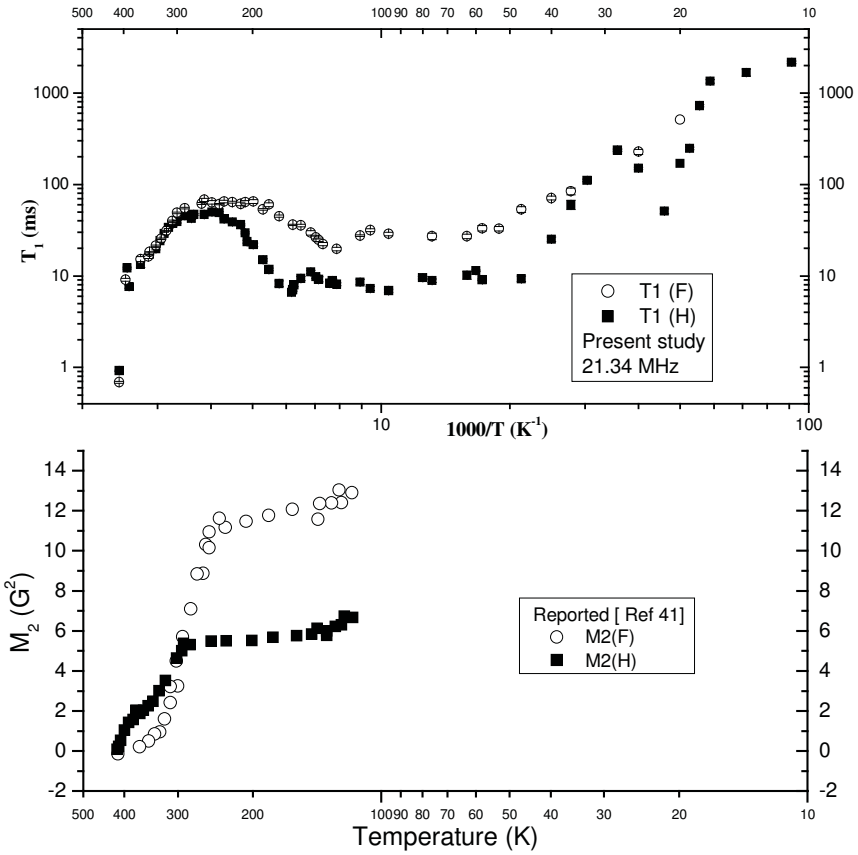

Fig 3.3 NMR Spin lattice relaxation times and second moments [41] of both proton (closed squares) and fluorine (open circles) for Ammonium zirconate in the entire temperature region of measurements.

Both decrease in T_1 and narrowing of the NMR signal shows the diffusion of both NH_4 and F ions through the lattice. High ionic conductivity above 400 K observed by Kavun et al [47] supports this. ^{1}H NMR line width above 400 K, measured by the same authors, reaches a limit of modulation width, as discussed above, indicating the diffusion of ammonium ions. The observed maximum in T_1 in the present study around room temperature may be attributed to the competition between diffusion and reorientational motion of the NH_4 ions.

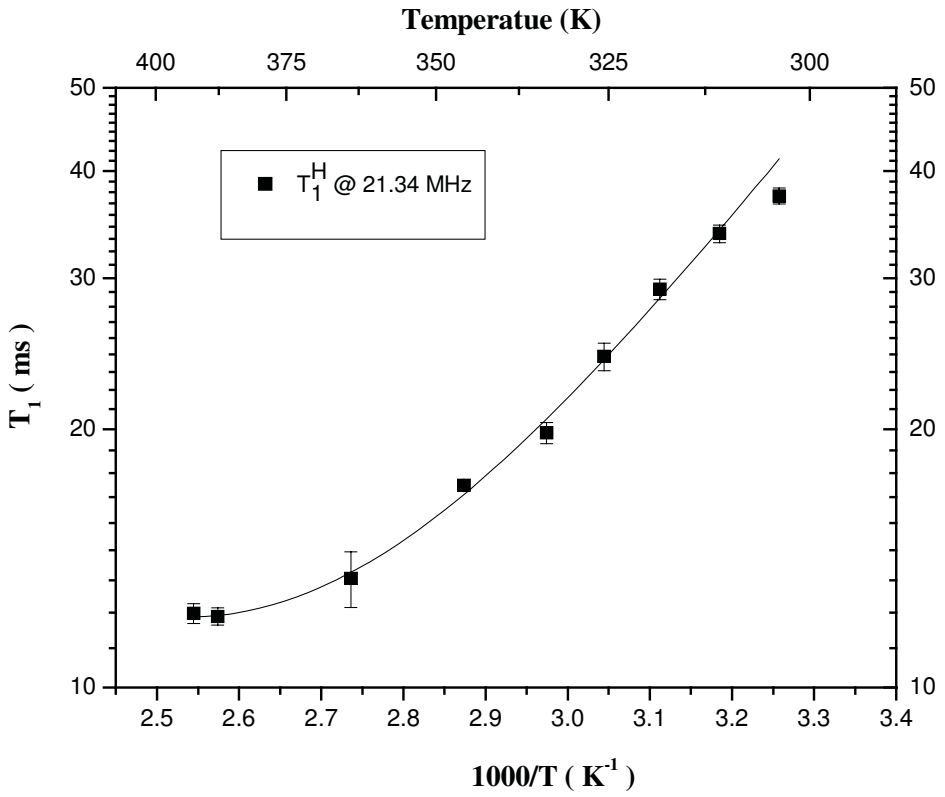

Figure 3.4 ^{1}H NMR T_1 data at 21.34 MHz for Ammonium zirconate in the high temperature region (> 300 K). Solid line shows the fit of T_1 data to Eqn. 3.1.

The spin lattice relaxation caused by translational diffusion using the random walk method by Torrey [51] has been described in Chapter 1. At high temperatures, when $\omega_o\tau << 1$, the relaxation rate due to translational diffusion is given by the Eqn. (1.65)

$$T_{1\,td}^{-1} = \left(\frac{8\pi N}{15a^3}\right) I(I+1)\gamma^4\hbar^2 \left[\frac{\tau/2}{1+\left(\omega\tau/2\right)^2} + \frac{\tau}{1+\omega^2\tau^2}\right]. \qquad (3.1)$$

The present high temperature T_1 data (> 300 K) is fit to the Eqn. (3.1) and is shown in the Fig. 3.4. The best fit parameters corresponding to the translational diffusion of the NH_4 ion are given in the Table 3.2. The activation energy E_a obtained for the translational diffusion is 23.2 (1) kJ/mol and the pre-exponential factor τ_{co} is 8.8 (1) x 10^{-12}s. These parameters compare with those reported for $(NH_4)\,SnCl_3$ [34].

Table 3.2 Motional Parameters for ammonium zirconate. The values given in parenthesis represent errors.

Mechanism	Ea (kJ/mol)	τ_{co} (s)
NH_4 diffusion	23.2 (1)	8.8 (1) x 10^{-12}
NH_4 reorientation	13.6 (0.3)	19 (1) x 10^{-14}

3.3.1.2 Intermediate temperature range (240 - 146 K)

Assuming that the NH_4 ion reorients in such a way that each proton spends the same amount of time at any of the hydrogen sites in the NH_4 tetrahedron, the proton relaxation time can be expressed using BPP approach as [1, 4, 52]

$$\left(T_1^{-1}\right)^H = \frac{27\,\gamma^4\,\hbar^2}{40\,r^6}\left[\frac{\tau_H}{1+\omega_H^2\,\tau_H^2} + \frac{4\,\tau_H}{1+4\,\omega_H^2\,\tau_H^2}\right], \qquad (3.2)$$

where 'τ_H' represents the correlation time of the NH_4 motion and is assumed to obey the

Arrhenius equation given by

$$\tau = \tau_0 \exp\left(E_a / RT\right) \ . \qquad (3.3)$$

Here τ_0 and E_a are called pre-exponential factor and activation energy of the ammonium motion respectively. In Eqn. 3.2, $\gamma = 2.675 \times 10^4$ G^{-1} s^{-1} is the nuclear gyromagnetic ratio of proton and 'r' is the inter proton distance in the NH_4 tetrahedron.

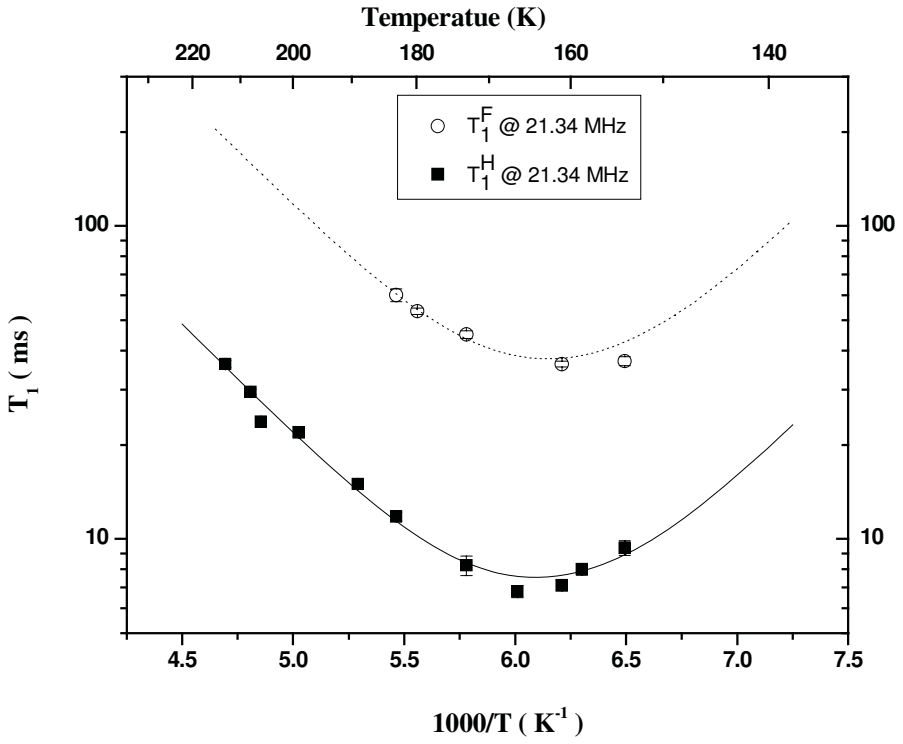

Figure 3.5 ^1H and ^{19}F T_1 data in the temperature range 220 – 146 K. Solid line represents the BPP fit to ^1H T_1 data and dotted line shows the simulated graph of BPP curve for ^{19}F T_1 data.

The BPP model as given in Eqn. 3.2 fits well to the present experimental ^1H T_1 data in the temperature region 240 to 146 K as shown in the Fig. 3.5. The pre-exponential factor and activation energy found from the best fit are 19 (± 1) x 10^{-14} s and

13.6 (± 0.3) kJ/mol respectively. The ^1H second moment studies in the same compound [41] suggests that the activation energy corresponding the reorientation of the ammonium ion should be less than 17 kJ/mol. The activation energy obtained from the present investigation 13.6 kJ/mol and agrees with the reported prediction [41]. The observed motional parameters are in the same order of magnitude with other $(NH_4)_2MCl_6$ compounds [37, 53].

3.3.1.3 Low Temperature (LT) region (146 – 11 K)

The T_1 behaviour below 146 K, can be explained based on the quantum rotational tunneling of the ammonium ion. Lalowicz et al have also attributed the line shape of the proton NMR signal at 4.2 K to quantum rotational tunneling [28].

Theory

At lower temperatures, the rotational tunneling of the NH_4 ion becomes dominant. The observation of low activation energy for the reorientation of the NH_4 ion along with tunnelling at low temperatures has been reported by several authors [54 - 55]. The low hindering barrier in the case of NH_4 ion gives more freedom to the cation and at low temperatures, it facilitates tunneling [56 - 57]. The Haupt's model [58] was modified by Koksal [54] to estimate the relaxation rate for the methyl group tunneling. Later Punkkinen [32] extended this model for ammonium ion. The four proton spins in an ammonium ion combine to form a five-fold degenerate A state ($I_{tot} = 2$), three sets of three – fold degenerate T states ($I_{rot} = 1$) and a doubly degenerate E state (($I_{tot} = 0$). The states are further split by the static magnetic field.

Assuming a very narrow tunnel-splitting distribution for ω_T and ω_E and that the torsional ground state is well separated from the first excited state, the relaxation rate can be given by [32],

$$\left(\frac{1}{T_1}\right)_{AT} = C_{AT}\left[\frac{\tau_T}{1+\overline{\omega}_T^2(\tau_T)^2}+\frac{\tau_T}{1+\left(\overline{\omega}_T \pm \omega_o\right)^2(\tau_T)^2}+\frac{\tau_T}{1+\left(\overline{\omega}_T \pm 2\omega_o\right)^2(\tau_T)^2}\right] \qquad (3.4)$$

for the transitions between A and T states, where $\overline{\omega}_T$ is the average tunnel frequency for the A-T transitions. The three terms on the right- hand side correspond to the transitions Δ m = 0, ± 1 and ± 2. Similarly, for the transitions between A and E states, the relaxation rate is given by

$$\left(\frac{1}{T_1}\right)_{AE} = C_{AE}\left[\frac{\tau_E}{1+\overline{\omega}_E^2(\tau_E)^2}+\frac{\tau_E}{1+\left(\overline{\omega}_E \pm \omega_o\right)^2(\tau_E)^2}+\frac{\tau_E}{1+\left(\overline{\omega}_E \pm 2\omega_o\right)^2(\tau_E)^2}\right] \qquad (3.5)$$

the three terms in the relation corresponding to the transitions Δ m = 0, ±1 and ±2. $\overline{\omega}_E$ is the average tunnel frequency for the A-E transitions.

The tunneling frequencies used in the Eqns. 3.4 and 3.5 can be approximately estimated from the value of observed $T_{1(min)}$ (when $\omega_t >> \omega_o$) using the relation [36]

$$\frac{T_{1(\min)}(obs)}{T_{1(\min)}(class)} \approx \frac{\overline{\omega}_T}{\omega_o}\,. \qquad (3.6)$$

This relation has been used in NH_4ClO_4 by Guttler and Von Schutz [29]. The relation (3.5) is reasonable if tunnel motion is considered to have a power spectrum centered around $\overline{\omega}_t$ instead of around $\omega = 0$ similar to the classical random motion.

In case of ammonium ion, an estimate of tunnel frequency can be made form the classical value of the T_{1min} using the relation [32]

$$\overline{\omega}_t \approx 25.13\times10^9 T_{1(\min)} \ , \tag{3.7}$$

where $\overline{\omega}_t$ is in Hz when T_1 is in s. An empirical relation between the activation energy and the tunnel frequency can approximately given as [57]

$$\overline{\omega}_t \approx 26.5\times10^{12}\exp\left(-10.4\sqrt{E_a}\right), \tag{3.8}$$

where $\overline{\omega}_t$ is in Hz when E_a is in kcal/mol.

Using the relations (3.6) or (3.7), an approximate estimate of tunnel frequency can be made and used in the equations (3.4) and (3.5) to give the best fit for the T_1 data at low temperatures and calculate the quantum parameters corresponding to the A-E or A-T transitions respectively.

When $\overline{\omega}_t \geq \omega_o$, the relations (3.5) and (3.6) can be modified as

$$\left(\frac{1}{T_1}\right)_{AT} = C_{AT}\left[\frac{\tau_T}{1+\overline{\omega}_T^2(\tau_T)^2}\right] \tag{3.9}$$

for A-T transition and

$$\left(\frac{1}{T_1}\right)_{AE} = C_{AE}\left[\frac{\tau_E}{1+\overline{\omega}_E^2(\tau_E)^2}\right] \tag{3.10}$$

for A-E transition. τ_T and τ_E follow the usual Arrhenius behaviour.

T_1 is found to be temperature independent, from 146 K down to 50 K, which suggests that only the ground tunnel state is occupied. Similar T_1 behaviour has been observed in many compounds at lower temperatures [34, 54, 59].

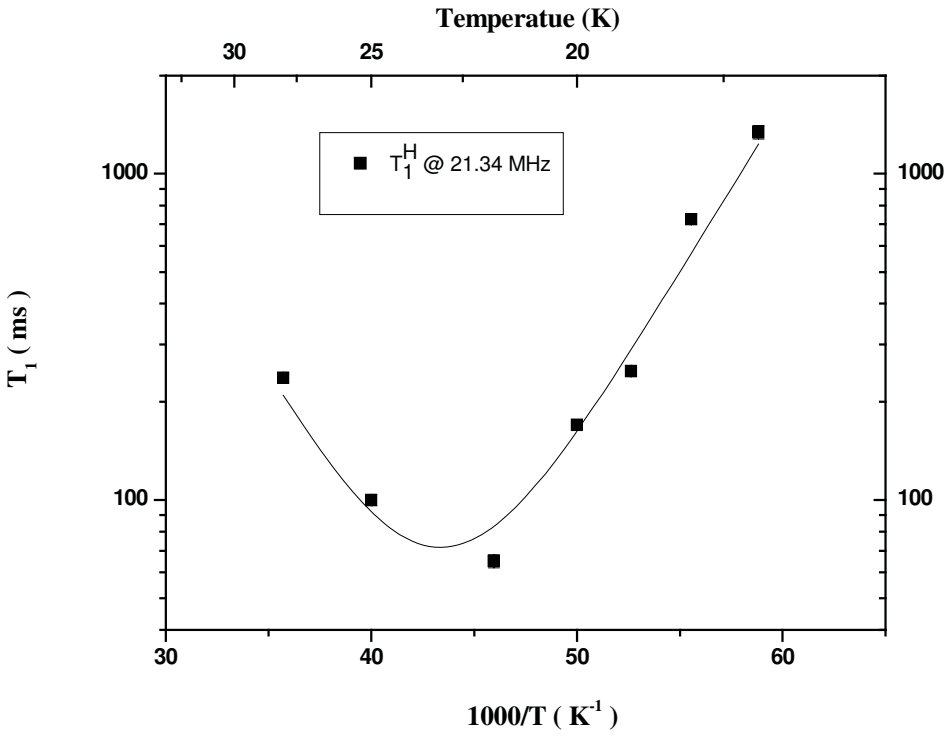

Figure 3.6 ^{1}H NMR T_1 data at 21.34 MHz for Ammonium zirconate in the temperature region (30 – 16 K). Solid line shows the fit of T_1 data to Eqn. 3.9.

We have tried to fit the T_1 data below 28 K to the Eqn. of the form 3.10. and is shown in Figure 3.6. The tunnel frequency is estimated to be 405 MHz. The tunnel frequency measured in a few ammonium hexahalo metallates are found to vary over a wide range from 1.4 MHz to 600 MHz. [57]. The energy of the torsional splitting is estimated as 1.98 kJ/mol and the pre exponential factor is 8.38 x 10^{-15} s. On comparing the tunneling parameters with that of NH_4SnBr_3, The observed tunnel frequency is higher than that of 'A-T' splitting and lower than that of 'A-E' tunnel splitting and activation torsional splitting between the ground state and the first excited state which is 1.98 kJ/mol, fairly in agreement with that of ' A-T' tunneling.

3.3.2 Analysis of ^{19}F NMR T_1

^{19}F spin lattice relaxation time also shows similar behaviour as that of proton T_1 and is about 3 times more than that of proton. At room temperature T_1 value is about 48 ms and on increasing the temperature, it starts decreasing up to 395 K, above which it reduces sharply to less than a millisecond similar to proton T_1. In the same temperature region, FID duration also increases a few times as the temperature is increased from 388 K to 410 K. On decreasing the temperature from room temperature, initially T_1 increases and shows a relatively broad maximum (as compared to that of proton) of about 60 ms around 220 K. Below 200 K, T_1 decreases and follows through a shallow minimum of about 35 ms around 160 K (at which proton minimum is also observed). Below 160 K, Fluorine T_1 again goes through another minimum of 19.7 ms and then increases to about 31 ms at 106 K. Below this temperature, T_1 remains constant (within experimental error) till about 50 K and on further reducing temperature T_1 again increases monotonically to about 500 ms at 20 K. Below 20 K signal could not be measured due to poor signal to noise ratio till the lowest temperature of measurement (11 K).

3.3.2.1 High Temperature (HT) region (410 - 240 K)

In the temperature range 120-200 K, the ^{19}F wide-line NMR signal [41] has shown a single asymmetric line and in the range 210 - 275 K the spectrum has shown a number of components width different widths and above 275 K the additional peaks have disappeared. The complexity of the ^{19}F NMR spectrum are due to polymeric nature of $(NH_4)_2ZrF_6$ makes it difficult to understand the NMR data. With further increase in temperature, the width of the line has decreased and around 340 K a new transformation

of the signal starts and completes above 400 K by the formation of an asymmetric narrow line with fine structure. The phase transformation of Ammonium zirconate in the temperature range 410 - 415 K has not changed the line shape. Hence, the analysis of the ^{19}F T_1 is similar to that of proton. Both decrease in T_1 and narrowing of the NMR signal may be attributed to diffusion of both F ions through the lattice. High ionic conductivity above 400 K observed by Kavun et al [47] supports this. Sub lattice movement of F ions is also observed above 400 K [47]. The observed maximum in fluorine T_1 in the present study around room temperature may be attributed to the competition between diffusion and reorientational motion.

3.3.2.2 Intermediate temperature range (200- 106 K)

^{19}F T_1 data in this temperature region also appears to follow the BPP model and fit of the linear portion of the ^{19}F T_1 data in this region gives the activation energy of 13 (± 1) kJ/mol and is attributed to reorientation of the ammonium group. Hence it is concluded that, the ammonium ion reorientations are rate determining and the fluorines relax to the lattice mainly by the random modulations of the H - F dipole-dipole interactions due to NH_4 motion. Several authors have observed similar behaviour in a number of compounds, for example, Watton et al [53] in $(NH_4)_2TiF_6$, McDowell et al [60] in $(CH_3)_3NPF_5$ and explained their results in the similar manner. Indeed, Kavun et al have also observed that in the present compound, ^{19}F second moment reaches the rigid lattice limit at much higher temperature of about 250 K. Fig 3.4 shows the BPP fit to ^1H T_1 data and simulated graph of BPP curve for ^{19}F T_1 is also shown.

3.3.2.3 Low temperature range (106 - 20 K)

Fluorine T_1 data in this temperature range is also attributed to the onset of ammonium ion motion as second moment studies in the same compound have shown that the fluorine motions freeze at much higher temperatures at least in the NMR time scale.

3.3 Conclusion

The present investigation reveals that in Ammonium zirconate, ammonium ion plays a major role in relaxation mechanism in the present temperature range of study. At higher temperature, the compound shows diffusion of both ammonium and fluorine sub lattice. Sharp increase of FID duration and sudden increase of relaxation rate around 395 K, is supported by other techniques such as wide-line NMR line shape, second moment as well as the conductivity studies. Further, this investigation reveals the reorientational motion of the ammonium ion is responsible for fluorine relaxation also. Another important observation is that even at low temperatures the fluorine nuclei are being relaxed due to quantum rotational tunneling of the ammonium ion. Superionic conductivity in the sample is interpreted as due to the NH_4 ion and fluorine sublattice motion.

References

1. Bloembergen N, Purcell EM, Pound RV. *Phys. Rev.*, **73 (7),** 679 (1948).
2. Hubbard PS. *Phys. Rev.,* **131,** 1155 (1963).
3. Torrey HC. *Phys. Rev.,* **76**, 1059 (1949).
4. Abragam A, *The Principles of Nuclear Magnetism*. Oxford University Press; New York, **1961**.
5. Ikeda I and McDowell. *Mol. Phys.,* **25**, 1217 (1973).
6. Punkkinen M, Tuohi JE and Ylinen EE. *J. Magn. Reson.,* **22**, 527 (1976).
7. Svare I. *J. Phys. C: Solid State Phys.,* **12**, 3907 (1979).
8. Prager M, Raaen AM and Svare I. *J. Phys. C: Solid State Phys.,* **16,** L181 (1983).
9. Pelzl J and Dimitropoulos C. *Z. Naturforsch*, **49a**, 232 (1994).
10. Armstrong RL, Van Drial HM and Sharp AR. *Can. J. Phys.*, **52**, 369 (1974).
11. Tegenfeldt J and Odberg L. *J. Phy. Chem. Solids*, **33**, 215 (1972).
12. Watton A, Sharp AR, Petch HE and Pintar MM. *Phys Rev.*, **5B**, 4281 (1979).
13. Kodama T. *J Magn. Reson*., **7**, 137 (1972).
14. Ylinel EE, Tuohi JE and Niemela LKE. *Chem. Phy. Lett.,* **24**, 447 (1974).
15. Ingman LP, Koivula, Lalowicz ZT, Punkkinen M and Ylinen EE. Z. *Phys. B Cond. Matt,* **81,** 175 (1990).
16. De Wit GA and Bloom M. *Can. J. Phys.*, **47**, 1195 (1969).
17. Murthy BVS. *Ph.D. thesis*, Department of Physics, Indian Institute of Science, Bangalore, India, **1993.**
18. Bonori M and Terenzi M. *Chem. Phy. Lett.*, **27**, 281 (1974).
19. *Watton A. J. Chem. Phys.,* **65**, 3653 (1976).
20. Prager M and Heidemann A. *ILL Report*, **87PR15T**, Table 13 (1987).

21. Srinivasan R. *MTP International Review of Science*, Physical Chemistry, Series 2, butterworths, London, **4**, 209 (1975).

22. Clough S. *Physica*, **136B**, 145 (1986).

23. Clough S, Horsewill AJ, Johnson MR, Mohammed MA and Newton T. *Chem. Phys.,* **152**, 343 (1991).

24. Clough S. *Encyclopedia of NMR*, Eds. Grant DM and Harris RK, **6**, 3933 (1996).

25. Horsewill AJ. *Spectrochim. Acta,* **48A**, 379 (1992).

26. Horsewill AJ, *Prog. Nucl. Magn. Reson. Spectr.* **35**, 359 (1999).

27. Watton A and Petch EA. *Phys. Rev.*, **B7**, 6 (1973).

28. Lalowicz ZT, McDowell CA and Raghunathan P. *J. Chem. Phys.,* **70**, 4819 (1979).

29. Guttler W and Von Schutz JU. Chem. Phys. Lett., **20,** 133 (1973).

30. Riehl JW, Wang R and Bernad HW. *J. Chem. Phys.,* **58**, 509 (1973).

31. Nijman AJ, Sprik M and Trappeniers NJ. *Physica,* **98B**, 247 (1980).

32. Punkkinen M. *J. Magn. Reson*., **19**, 222 (1975).

33. Tuohi JE, Ylinen EII and Niemela LKE. *Magn. Reson. And Rel. Phenomena*, **2**, Proc. 18th Ampere congress, Nottingham, 1974, eds Allen PS, Andrew ER and bates CA. North- Holland Publ.Co., Amsterdam, 399 (1975).

34. Senthil Kumaran S. *Ph.D. thesis*, Department of Physics, Indian Institute of Science, Bangalore, India, **1997**.

35. Punkkinen Ma and Clough S. *J. Phys. C: Solid State Phys.*, **8**, 2159 (1975).

36. Svare I and Tunstall DP. *J. Phys. C: Solid State Phys.,* **8**, L559 (1975).

37. Svare I, Raaen AM and Thorkildsen G. *J. Phys. C: Solid State Phys.*, **11**, 4059 (1978).

38. United States Patents: 20030171524, 6730746, 3130188, 5932512, 6838533, 6716569 and 4,391,652.

39. Allan Zalkin, David Eimerl and Velsko SP. *Acta Cryst.*, **C44**, 2050 (1988).

40. Annalize Kruger and Heyns AM.: *Vibra. Spectro.,* **14**, 171 (1997).

41. Kavun VYa, Sergienko VI, Chernyshov BN, Bukvetskii BV, Dedenko NA, Bakeeva NG and Ignat'eva LN. *Russ. J. Inorg. Chem*. **36 (4),** 570 (1991).

42. Lane AP and Sharp DWA. J. Chem. SOC. (A), **2942** (1969)

43. Kavun VYa, Didenko NA, Slobodyuk AB Tkachenko IA, Gerasimenko AV, Uvarov NF and Sergienko VI. *J. Struct. Chem.* **46 (5),** 839 (2005).

44. Voit EI, Voit AV, Kavun Vya and Sergienko VI. *J. Struct. Chem.,* **45(4),** 610 (2004).

45. Gordienko PS, Vasil'ev AM and Epov DG. *Russ. J. Physical Chem.,* **56,** 542 (1982).

46. Epov DG and Mikhailov MA. *Russ. J. Inorg. Chem*. **22(4),** 534 (1977).

47. Kavun VYa, Uvarov NF, Slobodyuk AB, Goncharuk VK, Kotenkov AYu, Tkachenko IA, Gerasimenko AV and Sergienko VI. *Russ. J. Electrochem.,* **41 (5),** 501 (2005).

48. Rodriguez AM, Martinez JA, Caracoche MC, Rivas PC and Lopez Garcia AR. *Hyperfine Interactions*, **14**, 227 (1983).

49. Rodriguez AM, Martinez JA, Caracoche MC, Rivas PC, Lopez Garcia AR and Spinelli S. *J. Chem. Phys.,* **82 (3)**, 1271 (1985).

50. A. M. Heyns, K. R. Hirsch, and W. B. Holzapfel. *J. Chem. Phys.,* **73 (1)**, 105 (1980).

51. Torrey HC. *Phys. Rev.,* **92(4),** 962 (1953).

52. Blinc R and Lahajnar G. *J. Chem. Phys.* 4**7 (10)**, 4146 (1967).

53. Wattton A, Koster E, Sandu HS and Petch HE. *J. Chem. Phys.* **70 (11)**, 5197 (1979).

54. Köksal F, Rössler E and Sillescu H. *J. Phys. C: Solid State Phys.*, **15**, 5821 (1982).

55. Allen PS and Snell AJ. *J. Phys. C: Solid State Phys.,* **6**, 3478 (1973).

56. Tuohi JE, Ylinen EII. *Phys. Scr.,* **13**, 253 (1976).

57. Svare I. *J. Phys. C: Solid State Phys.,* **10**, 2679 (1977).

58. Haupt J. *Z. Naturforsch*, **26a**, 1578 (1971).

59. Senthil Kumaran S, Ramesh KP and Ramakrishna J. *Mol. Phy.,* **99(16)**, 1373 (2001).

60. McDowell CA, Raghunathan P and Williams DS. *J. Magn. Reson.*, **32**, 57 (1978).

Chapter 4

NMR Studies in Tetramethylammonium (TMA) Salts

NMR is a powerful technique for providing information about the reorientation and phase transitions. Temperature dependence of spin lattice relaxation time is useful in the study of structure and dynamics of the molecular groups present. Nature of molecular motions can be understood by interpreting the relaxation behaviour using suitable well-established models. Deviation of the observed results from the expected behaviour is also an useful information, which leads to the newer relaxation mechanisms. The observations of change of slope and discontinuities in T_1 along with the presence of hysterisis in T_1 have been recognized as the signature of different kinds of phase transitions [1-9].

Tetramethylammonium salts have captured the attention of both physicists as well as chemists for quite some time, because of their symmetry and interesting dynamics. Successive replacement of hydrogen by CH_3 groups in ammonium ion according to the formula $(CH_3)_x NH_{4-x}$ (x = 1…4), leads to a cation with a larger ionic radius, which may result in strong phase transitions due to changes in symmetry as well as the tolerance factor [10]. Substitution of the CH_3 leads to additional symmetry elements and hence increased reorientation motions [11]. Tetramethylammonium metal salts are known to exhibit phase transitions, hindered reorientational motion of the symmetry groups like CH_3 as well as whole cation $(CH_3)_4N$ and quantum rotational tunneling of the CH_3 groups. Moreover, Tetramethylammonium salts are of general interest in preparative chemistry. Their enhanced solubility in aprotic solvents in comparison to the corresponding alkali metal salts as well as their increased reactivity (which is due to a lower degree of solvation of their anions in solutions of non-polar solvents) make them powerful and versatile synthetic reagents [12].

This chapter contains the results of proton (and fluorine) NMR second moment as well as spin lattice relaxation time studies in Tetramethylammonium Selenate ($[(N(CH_3)_4]_2SeO_4$) and Tetramethylammonium Hexafluorophosphate ($N(CH_3)_4PF_6$).

4.1 Tetramethylammonium Selenate $((CH_3)_4N)_2SeO_4$

4.1.1 Introduction

A_2BX_4 (A = K, Rb, NH_4, $N(CH_3)_4$ B = S, Zn, Cd, Ba, Cr, Hg, Se and X= Cl, Br, I, O etc) compounds are widely investigated and are still interesting to study, as they exhibit interesting incommensurate-commensurate phase transitions with temperature, ferroelectric properties and complex reorientational dynamics [13-17]. Recently, Horicuchi et al [18] have correlated their NMR results with single crystal x-ray results and Differential Scanning Calorimetry measurements to understand the nature of phase transitions in the similar compound $((CH_3)_3CNH_3)_2ZnCl_4$. The knowledge about the crystal chemistry of tetraalkylammonium salts is still limited [12], at least in tetraoxo complex salts $(N(CH_3)_4)_2XO_4$, which are of the pseudo A_2B-type. Tetramethylammonium Selenate (TMA-Selenate) is particularly interesting to study, not only for its interesting molecular reorientational dynamics but also due to its use in preparative chemistry [12].

4.1.2 Earlier studies

Sato et al [19] and Malchus et al [12] have prepared the compound TMA-Selenate. However, Malchus et al have reported that the compound prepared by Sato et al is not TMA-Selenate as they claim, but it is the hydrated one of TMA-Selenate. Two modifications (at 261 and 310 K) are characterized by X-ray diffraction methods and reported that, the compound crystallizes in a tetragonal lattice system with a = 13.95 and

c = 12.90 Å and also observed three heat anomalies at 127, 279 and 290 K through DTA. Sato et al have also reported ^{1}H NMR T_1 results in the temperature range 400 -200 K. Malchus et al [12] also have synthesized the same compound by adopting a different preparation method and carried out the temperature dependent single crystal XRD measurements and found a disagreement with that of Sato et al [19]. According to XRD analysis of Malchus et al, the compound crystallizes in cubic face centered crystal system ($Fm\bar{3}m$) with a = 11.11 Å and the complex ions are packed in a Li_2O_2-type arrangement. Further, in contrast to Sato et al, they have not reported any phase change in the temperature range 103 - 300 K. Coupled thermogravimetric and differential thermal analysis measurements [12] revealed the decomposition of the selenate in two exothermic steps beginning at 503 ± 3 K and the third step is found to occur at 673 K resulting in a reddish-brown residue. IR and Raman studies by the same authors [12] have proved that, the $N(CH_3)_4^+$ tetrahedron is regular and in a fixed orientation, while the selenate ion, however, is orientationally disordered. To unravel the difference in XRD results, Malchus et al have carried out powder XRD study after exposing their compound to moisture and found that it compares well with the powdered XRD pattern reported by Sato et al [19]. Hence they have concluded that Sato et al might have studied the sample which was exposed to atmosphere and hence it might be the hydrate of tetramethylammonium selenate and not the $((CH_3)_4N)_2SeO_4$ [12]. Thus, these studies lead to a controversy regarding the structure of this compound [12, 19]. Present study is an attempt to resolve this controversy. Figure 4.1 shows the unit cell of the refined model and the ORTEP plots of the complex ions and the characteristic parameters of TMA- Selenate are given in Table 4.1.

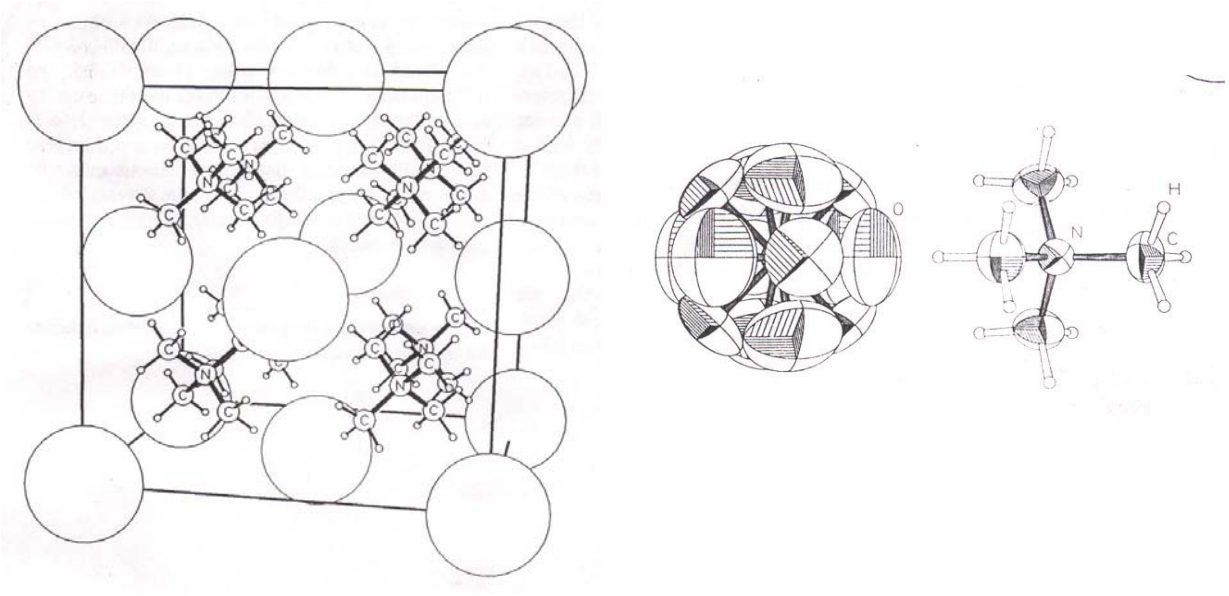

(a) (b)

Figure 4.1 (a) Unit cell of TMA- Selenate (spheres represent the disordered Selenate ions) (b) Complex ions of TMA- Selenate (ORTEP plots with 50% probability level) [12]

Table 4.1 Characteristic parameters of TMA-Selenate [12]

Structure	Cubic
Space group	$Fm\bar{3}m$
Cell dimension (a)	11.107 Å
Density	1.421 g cm^{-3}
Se-O (1)	1.63 Å
Se-O (2)	1.63 Å
N-C	1.49 Å
C-H	1.02 Å
C-N-C	109.5º
N-C-H	114º
Phase transitions	573 K 127 K, 279 K and 290 K [19]

Table 4.2. X-ray powder diffraction data of TMA-Selenate

d (Å) [Reported 12]	d (Å) [Present study]
6.416	6.418
3.928	3.925
3.350	3.348
2.779	2.782
2.485	2.490
2.138	2.140
1.965	1.964
1.878	1.880

4.1.3 Sample preparation and characterization

Different methods have been reported in the literature for the preparation of the TMA-Selenate [12, 19]. TMA-Selenate is synthesized by mixing tetramethylammonium hydroxide (Aldrich, 33,163-5) and Selenic acid (Aldrich, 30,843-9) in stoichiometric proportions [19]. Cylindrical crystals formed upon slow evaporation of the solvent, over a few months, are dried under vacuum before using them for further studies because of their hygroscopic nature. The Powder XRD measurements are carried out at room temperature using Panalytical diffractometer and the observed experimental d-spacings compare well with those reported by Malchus et al (Table 4.2) [12]. The compound is finely powdered and vacuum-sealed into glass ampoules of 5 mm diameter in helium atmosphere for NMR studies.

^{1}H NMR spin lattice relaxation time (T_1) measurements are carried out, as a function of temperature in the range 389 – 6.6 K, at 21.34 MHz using a home made

pulsed NMR spectrometer described in Chapter 2 and inversion recovery pulse sequence is used for T_1 measurement over the entire temperature range.

4.1.4 Results and discussion

A plot of T_1 versus 1000/T is shown in Figure 4.2. Initially T_1 decreases with decrease in temperature from 389 K giving rise to a broad minimum of about 9 ms centered around 280 K. On further decrease in temperature, T_1 increases with a decrease in signal intensity and hence we could make measurements only up to 170 K and the signal vanishes completely around 150 K. On cooling the sample much below 150 K, the signal reappears at about 85 K and the signal intensity builds up enabling T_1 measurements from 72 K down to 6.6 K, which is the lowest temperature of measurement in the present study.

4.1.4.1 High temperature region (389 - 170 K)

Sato et al [19] have made T_1 measurements at 20 MHz in the temperature range 400 - 200 K. They have observed two minima: a shallow one (19 ms around 400 K) and another deep one (11 ms around 280 K), which are attributed to TMA and CH_3 group reorientations respectively. A theoretical fit of T_1 was extrapolated above 400 K to emphasize the shallow minimum. On the contrary, the present investigations reveal only one broad minimum of about 9 ms around 280 K and on high temperature side of the minimum, T_1 increases monotonically up to 250 ms at 389 K. The high temperature (389 -170 K) T_1 data can be explained using Bloembergen-Purcell-Pound (BPP) model modified for TMA group by Albert et al [5].

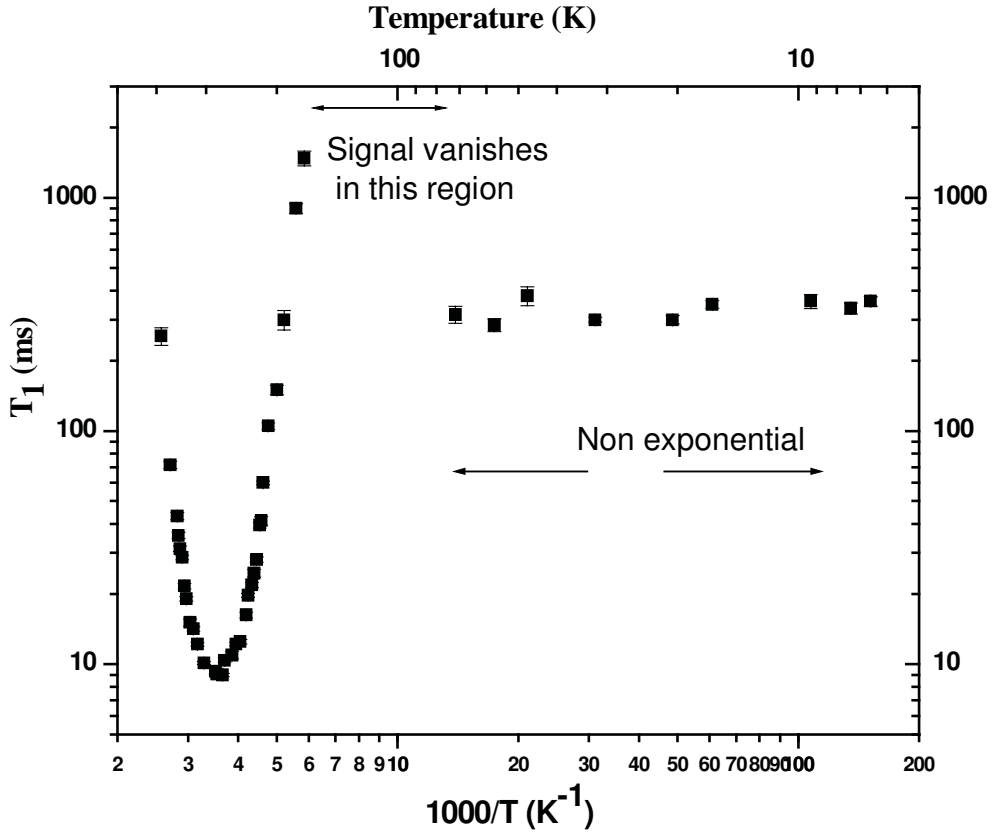

Figure 4.2 Variation of T_1 as a function of inverse temperature at 21.34 MHz for $(TMA)_2SeO_4$ over the entire temperature region (389 - 6.6 K).

Theory

Tetramethylammonium ion has tetrahedral symmetry (similar to the NH_4^+ ion). It has 3 two - fold and 4 three - fold symmetry axes. The T_1 behaviour in tetramethylammonium compounds can be explained using a modified BPP [20] approach, as given by Albert et al [5]. They have studied the ^1H T_1 in several tetramethylammonium halides and the experimental results have been analyzed by considering the tetramethylammonium ion and methyl group reorientations about their C_3 axes. In tetramethylammonium compounds, the two motions that mainly contribute to the relaxation are (a) random

reorientation of the CH_3 groups with correlation time τ_c and (b) isotropic tumbling of the TMA ion (whole cation) with a correlation time τ_{c1}. They modulate the intra-methyl and inter-methyl dipole-dipole interactions and facilitate the spin-lattice relaxation.

The intra-methyl proton-proton interaction is modulated by the reorientations of the methyl groups about their C_3 axes. The relaxation rate due to the intra-methyl contribution is given by [5, 21]

$$T_{1(\text{int}ra)}^{-1} = \frac{9}{20}\frac{\gamma^4 \hbar^2}{r^6}\left(f(\omega,\tau_{c2}) + \frac{1}{3} f(\omega,\tau_{c1}) \right), \qquad (4.1)$$

where,

$$f(\omega,\tau_c) = \frac{\tau_c}{1+\omega_I^2\ \tau_c^2} + \frac{4\,\tau_c}{1+4\,\omega_I^2\ \tau_c^2} \qquad (4.2)$$

and

$$\tau_{c2}{}^{-1} = \tau_c{}^{-1} + \tau_{c1}{}^{-1}\ . \qquad (4.3)$$

In the above equations, γ = 2.675 x 10^4 G^{-1} s^{-1} is the nuclear gyromagnetic ratio of protons, 'τ' represents a correlation time of the motion and is assumed to obey the Arrhenius equation given by

$$\tau = \tau_0 \exp\left(E_a / RT\right)\ . \qquad (4.4)$$

Here τ_0 and E_a are called pre-exponential factor and activation energy of the corresponding motion respectively.

The methyl group is considered as a three-spin system with 3 protons in each methyl group situated at the corners of the triangle and 'r' is the inter proton distance within in the methyl group. Considering 'R' as the distance between the centers of the proton triangles, then the relaxation rate due to the inter methyl proton-proton interaction,

modulated by the tumbling of the TMA ion , is given by [5, 22]

$$T_{1(inter)}^{-1} = \frac{27}{20}\frac{\gamma^4 \hbar^2}{R^6} f(\omega, \tau_{c1}) . \qquad (4.5)$$

The effective relaxation rate is the sum of the relaxation rates due to the intra-methyl and inter-methyl contributions and is given by [22]

$$T_1^{-1} = T_{1(intra)}^{-1} + T_{1(inter)}^{-1} \qquad (4.6)$$

$$\text{i.e., } T_1^{-1} = A f(\omega, \tau_{c2}) + B f(\omega, \tau_{c1}) \qquad (4.7)$$

where

$$A = \frac{9}{20}\frac{\gamma^4 \hbar^2}{r^6} \qquad (4.8)$$

and

$$B = \frac{3}{20}\frac{\gamma^4 \hbar^2}{r^6} + \frac{27}{10}\frac{\gamma^4 \hbar^2}{R^6} \quad . \qquad (4.9)$$

Assuming that the TMA ion is an undistorted tetrahedron with C-H distance of 1.09 Å, C-N distance of 1.5 Å, the values of 'r' and 'R' calculated to be 1.78 Å and 3.04 Å respectively. Thus the values of A and B are found to be A = 8.05 x 10^9 sec^{-2} and B = 4.61 x 10^9 sec^{-2}.

From Eqn. 4.7, one expects a minimum of 20.27 ms corresponding to the TMA tumbling motion, at $\omega\tau_{c1} = 0.616$ and another minimum of 11.74 ms corresponding to the CH_3 group reorientation at $\omega\tau_c = 0.616$ at the larmor frequency of 21.34 MHz. However, T_1 results in the present investigation reveals only one broad asymmetric minimum of 9 ms. The Albert et al model has been used for the analysis of T_1 results in the present compound and the fit is shown in Fig. 4.3. The best-fit parameters for CH_3 and TMA cation motions are given in Table 4.3.

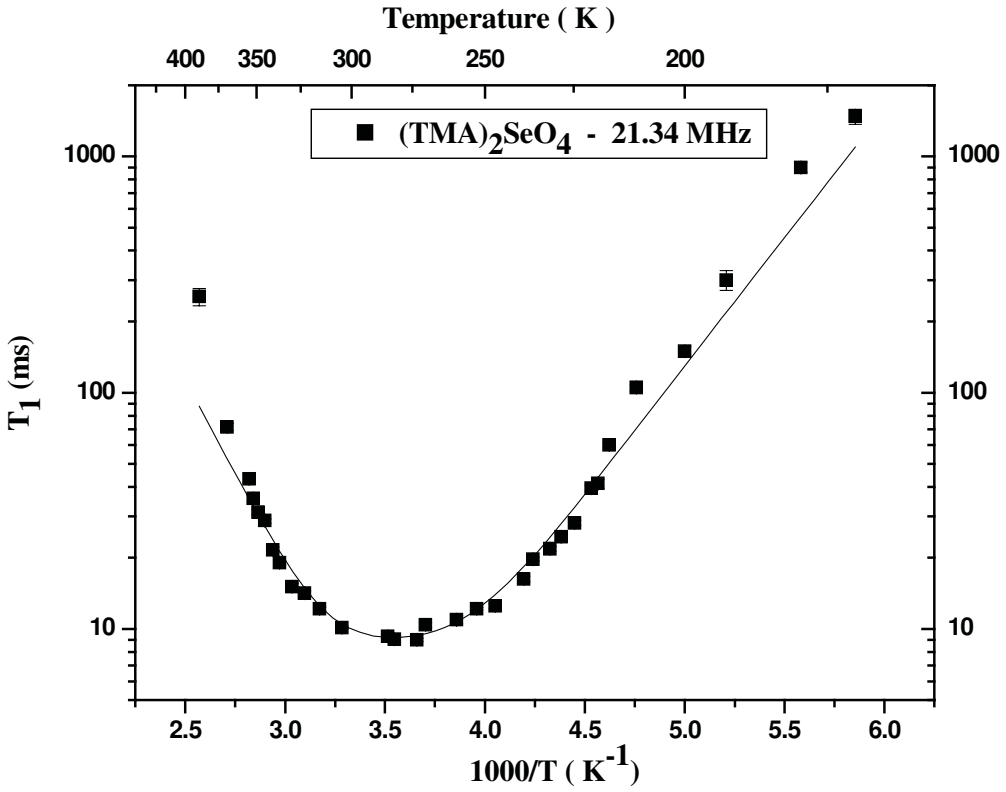

Figure 4.3 T_1 Versus 1000/T in the temperature region 389 – 170 K. Solid line represents the fit to Eqn. 4.7

Table 4.3. Motional parameters for TMA-Selenate in the temperature region (389 –170 K). The values given in the parentheses represent the errors.

Symmetric group	Activation energy (kJ/mol)	Pre-exponential factor (10^{-13} s)
Methyl	20.4 (0.1)	5.3 (0.5)
TMA	33.5 (0.5)	0.09 (0.01)

The observed activation energies for both CH_3 and $(CH_3)_4$ ions obtained from the present study are respectively lesser than that of Sato et al [19] for the same compound (27 and 41 kJ/mol) as well as in $((CH_3)_4N)_2SO_4$ (28 and 45 kJ/mol) and $(CH_3)_4NX$ (X = Cl, Br and I) (23-28 and 37-54 kJ/mol) [8]. However, they are in good agreement with the values reported for the compound $TMAClO_4$ (21.2 and 32.9 kJ/mol) [23]. The CH_3 group activation energy is slightly greater than 15-17 kJ/mol and the $(CH_3)_4$ group activation energy compare well with the reported value of 30-37 kJ/mol, determined for the room temperature phase of $[(CH_3)_4N]_2\ MX_4$ (M=Pb and Pt ; X = Cl and Br) [24]. This shows an increased volume for reorientation of the groups as compared to pure salts**.** On comparing the activation energies of the CH_3 and $(CH_3)_4N$ groups in $((CH_3)_4N)_2\ SeO_4$ with that of $((CH_3)_4N)_2\ SO_4$, it must be noticed that the activation energy of the methyl group is less in $((CH_3)_4N)_2\ SeO_4$ because of larger radius of selenium atom and its increased cell volume [19].

The observed asymmetric broad T_1 minimum of 9 ms at 21.34 MHz in our study is neither in agreement with that of expected minima of 11.74 ms for CH_3 group nor of 20.27 ms for $N(CH_3)_4$ group [5]. Similar broad minimum has been observed in many compounds like TMACl [5], $TMAClO_4$ [23], $TMASnCl_3$ [25, 26] and $TMAHgBr_3$ [27]. The occurrence of this broad minimum could be due to the fact that, the reorientation rates of both methyl and TMA ions are of the same order. As discussed earlier, our powder XRD data do not agree with that of Sato et al, but agree quite well with those reported by Malchus et al, which confirms to the crystal structure as cubic. Further, it is also worth noting that the lower activation energies obtained from the present study, with respect to Sato et al, also suggest that, the symmetric groups are less hindered in the

TMA-Selenate, as expected for a cubic system compared to tetragonal system. Therefore, both our NMR and powder XRD results support the argument of Malchus et al. Hence, we can conclude that, the compound used in the present study is in the cubic space group in agreement with that of Malchus et al [12] and not the hydrated TMA-Selenate as reported by Sato et al [19].

The increase of T_1 on the low temperature side of the T_1 minimum (from 170 K down to about 85 K) and a decrease of signal intensity beyond measurements and subsequent disappearance of the signal indicates that compound reaches rigid lattice limit at least in the NMR time scale.

4.1.4.2 Low temperature region (72 - 6.6 K)

On cooling the sample much below 150 K, the signal reappears at about 85 K and the signal intensity builds up enabling T_1 measurements from 72 K to 6.6 K. T_1 shows almost temperature independent behaviour in the temperature region 72 - 6.6 K. Further the magnetization recovery profile shows a deviation from both single exponential as well as bi-exponential fit. However, it fits well to a stretched exponential function at all temperatures below 72 K down to 6.6 K with a varying stretched exponent. Figure 4.4 represents the typical magnetization recovery profile at 57.3 K and the insert within this figure shows the goodness of the fit to stretched exponential equation given by

$$M_z(\tau) = M_0 \left[1 - 2\ e^{-\left(\frac{\tau}{T_1}\right)^{\alpha}} \right]. \qquad (4.10)$$

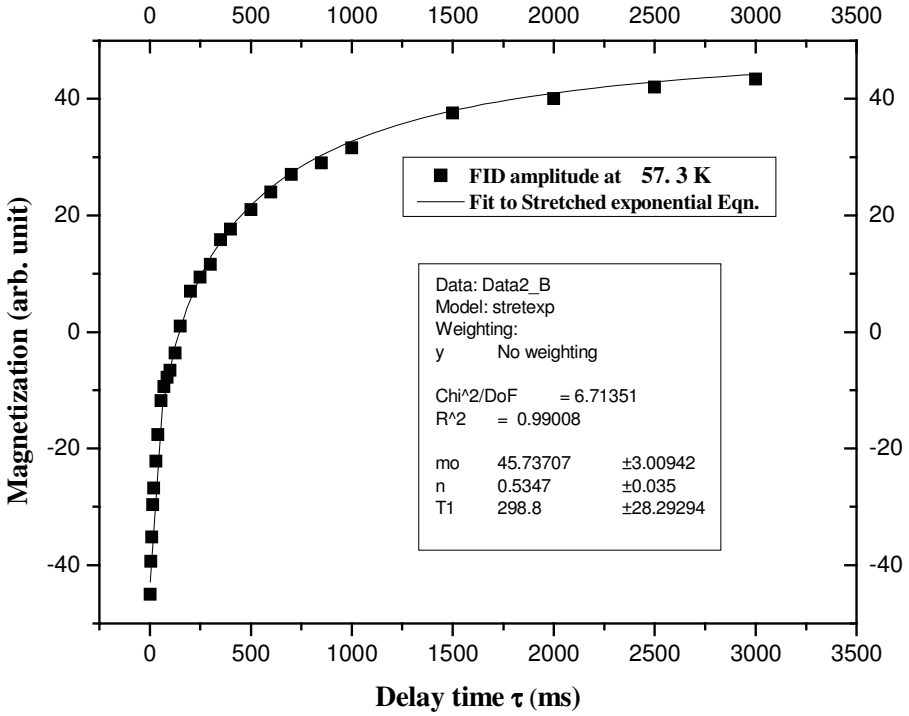

Figure 4.4 Magnetization recovery data versus τ plot for TMA-Selenate at 57.3 K. Solid line represents the fit to stretched exponential equation 4.10.

In this case, the repetition time of the inversion recovery pulse sequence is kept longer than 10 times the spin-lattice relaxation time so that the weight of the slowly relaxing components is also taken care. The value of exponent factor is about 0.5 when the signal reappears and it remains same within experimental errors till about 30 K. Below 30 K, the stretched exponent value increases monotonically and reaches unity as the temperature approaches 6.6 K. All these features points to conclude the presence of quantum rotational tunneling of the methyl groups.

Effects of rotational tunneling of CH_3 and NH_4 groups on proton spin-lattice relaxation have been discussed by several authors [1, 2, 26, 28-38] to explain the non-exponential magnetization recovery and multiple T_1 minima at low temperatures.

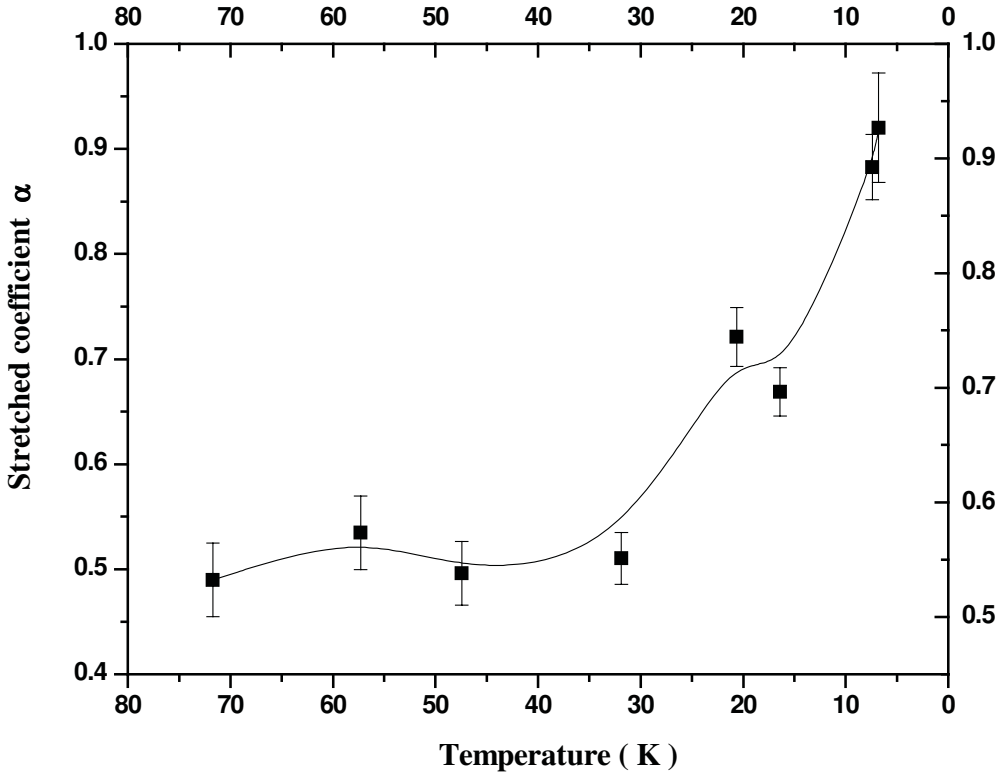

Figure 4.5 Variation of stretched exponent factor (α) with temperature. The line drawn is a guide to the eye.

Variation of the stretched exponent (Fig. 4.5) with temperature can be explained in the following way. In certain systems, the presence of inequivalent CH_3 groups may lead to different spin temperatures and each set of spins relaxing with its own relaxation time constant, and hence the bulk magnetization recovery follows a stretched exponential behaviour. This is true when inequivalent CH_3 groups are present and if the spin diffusion

becomes weaker in certain range of temperatures. However, when the temperature is lowered, the stretched exponent approaches unity, suggesting that the inequivalent methyl groups start attaining a common spin temperature. On further cooling the sample, the bulk magnetization recovery becomes single exponential.

In the present case, T_1 shows almost temperature independent behaviour and we have tried to fit our T_1 results using the model proposed by Koksal et al [39] who also have observed similar behaviour in certain metal acetates. According to the model proposed by them, T_1 shows temperature independent behaviour when only ground state of the tunnel splitting levels are occupied.

Theory

Koksal et al [39] have studied a number of metal acetates by ^{1}H NMR T_1 measurements and explained their experimental results by considering temperature dependence of tunnel splitting. At low temperatures, it is assumed that only the torsional ground state (n = 0) of the methyl group is occupied. The relaxation occurs when spin-flips are connected with the tunnel splittings. When the tunneling frequency is larger than the Larmor frequency, one can write the expression for the relaxation rate by considering only the intra-methyl interaction and temperature dependence of the tunnel frequency, as

$$\frac{1}{T_{AE}} = C_{AE} \sum_{m=-2}^{2} \frac{m^2 \tau_{c0}^T}{1+ < \varpi_T^0 >^2 (\tau_{c0}^T)^2} \tag{4.11}$$

where ϖ_T^0 is the tunnel frequency in the ground state

$$\text{and } C_{AE} = \frac{9}{20} \frac{\gamma^4 \hbar^2}{r^6} d_0^2 \tag{4.12}$$

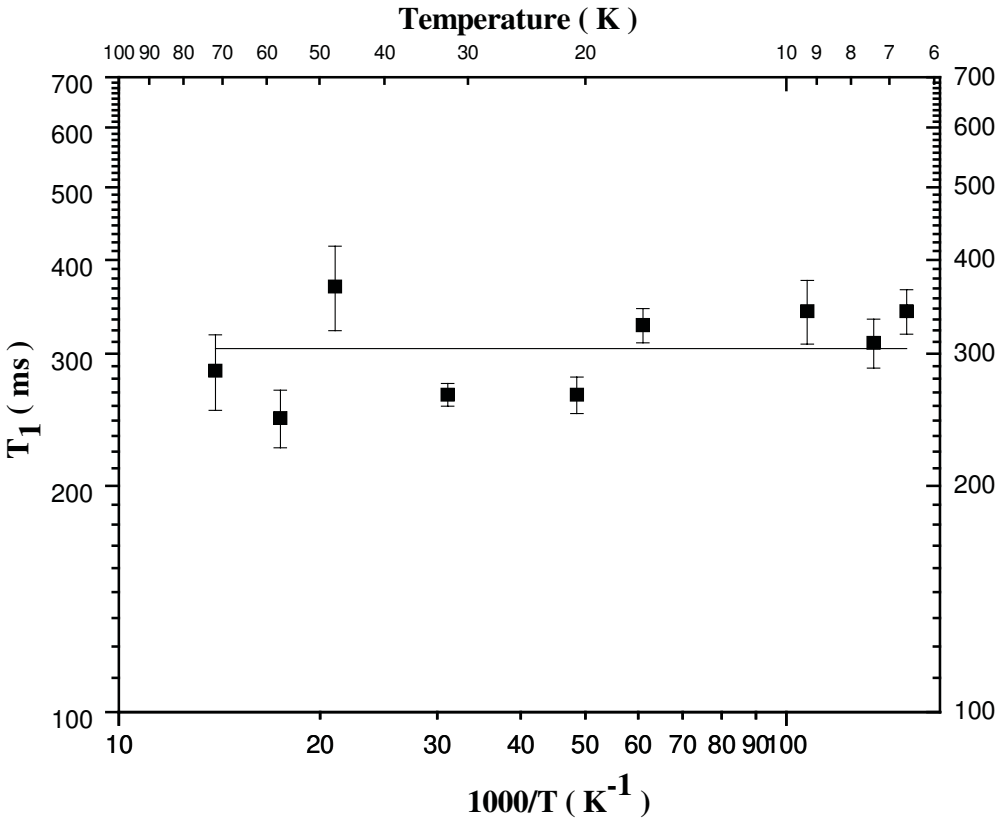

Figure 4.6 Low temperature (72 - 6.6 K) data. Solid line represents the fit to Eqn. 4.11.

Table 4.4 Motional parameters evaluated (72 - 6.6 K) using Koksal model [39].

Parameters	Estimated values
τ^{T}_{c0}	5.26 x 10^{-11} s
C_{AE}	6.25 x 10^{9} s^{-2}
ω^{0}_{T}	5.70 x 10^{9} s^{-1}

In the Eqn. 4.12, '*r*' is the inter proton distance in the methyl group and d_0 is the matrix element of the space part of the dipolar operator between the ground state wave functions of the harmonic oscillator [39, 40].

The T_1 data between 72 and 6.6 K is fit to the model used by Koksal et al and is shown in Fig. 4.6. The best-fit motional parameters obtained from the fit are given in Table 4.4, which are comparable with those reported earlier [26, 39]. Though the magnetization follows stretched exponential in this temperature region, the observed correlation time can be considered as the effective correlation time of the all spin systems.

4.1.5 Conclusions

A broad T_1 minimum observed in TMA – Selenate around 280 K is attributed to the simultaneous motions of CH_3 and $(CH_3)_4N$ groups. Lower activation energy obtained from the T_1 analysis as well as powder XRD measurements confirm that, the present compound crystallizes in cubic form and not as tetragonal. Magnetization recovery is found to be stretched exponential below 72 K with varying stretched exponent. Low temperature T_1 results show the quantum rotational tunneling of methyl groups and the observed T_1 is the resultant of the relaxation of all spin systems.

4.2 Tetramethylammonium Hexafluorophosphate $(CH_3)_4NPF_6$

4.2.1 Introduction

ABX_6 (A = K, Na, Rb, Cs, $C_5H_{10}NH_2$, $C_4H_8NH_2$, $C(NH_2)_3$, NH_4, $N(CH_3)_4$, B =P and X= F) compounds have been investigated using different techniques as they exhibit phase transitions with temperatures, and complex reorientational dynamics [41 - 47]. The line shape and spin lattice relaxation studies of the fluorine NMR have been extensively carried out as a function of temperature in the polycrystalline sodium, potassium, rubidium and cesium hexafluorophosphates [41]. From these studies, it is concluded that the fluorine line shape is sensitive to the physical state and in the case of $RbPF_6$, the thermal history of the sample and this behaviour is also observed in heat capacity measurements [48]. Motional narrowing of the dipolar broadening by PF_6^- reorientations are found in all the samples studied and the temperature of its occurrence is found to increase monotonically from a temperature less than about 50 K for the cesium compound to about 155 K for the sodium. These effects are attributed to crystal defects, which lower the hindrance to reorientation of the PF_6^- ions and decrease the size of domains in which there is a cooperative 'freezing out' of the reorientations. Thus the samples exhibits two-phase behaviour, a phase without imperfections (or with fewer) in which the PF_6 ions reorient more slowly than in a phase with a high (or higher) concentration of defects. This study along with the earlier very extensive NMR investigations of the ammonium and tetramethylammonium complexes in general and ammonium hexafluorophosphate in particular have suggested that it would be instructive to investigate tetramethylammonium hexafluorophosphate (TMA-Phosphate), in which the reorientations of both cation and anion groups are present. It is observed that, T_1 is

often more sensitive to phase changes and cross relaxation than to line shape or second moment and its temperature dependence provides much more reliable values of the activation energies for the processes governing the relaxation.

In the present study, the proton and fluorine spin lattice relaxation time (T_1) and proton second moment measurements are undertaken in an analogues compound, TMA-Phosphate for the following reasons: (1) The three possible reorienting groups CH_3, $N(CH_3)_4$ and PF_6 are very well suited for NMR studies. (2) The importance of proton-fluorine dipolar interactions can be investigated. (3) The anions BF_6 (B = P, Sb and As) are known to form very weak hydrogen bonds [49] (4) The coexistence of two phases.

Further TMA-Phosphate is a promising candidate for technological applications Viz., in high energy density battery applications, as electrolyte for the preparation of the films, as electrolyte for preparation of films, as antifungal agent to make semiconductor films, as corrosive resistant material and in making opaque inkjet ink compositions [49A].

In the present study, commercially available TMA-Phosphate from Aldrich Chemicals [558-32-7] is used directly without further purification. The compound is finely powdered and vacuum-sealed into glass ampoules of 5 mm diameter in helium atmosphere and then used for NMR measurements.

49A. **Earlier studies**

Wang et al have reported the room temperature crystal structure of TMA-Phosphate [50]. The crystal structure of TMA-Phosphate indicates that even though the N- atom formally has a distorted tetrahedral symmetry ($\bar{4}2m - D_{2d}$), the cation can nevertheless be considered to be tetrahedral within experimental accuracy and the P atom has square-pyramidal symmetry (4mm). The infrared and Raman studies [47] have not revealed any phase transitions with temperature and the existence of ordered PF_6 groups. The characteristic parameters of TMA- Phosphate are given in Table 4.5. ^{31}P NMR, DSC and X-ray powder diffraction measurements as a function of temperature have been carried out by Reynhardt et al [51]. DSC measurements from 120 to 800 K revealed three endothermic transitions, viz. at 770, 789 and 795 K. On lowering the temperature below 210 K, the X- ray diffractogram has shown additional peaks and the peak intensities increase with decreasing temperature and remain constant below 150 K. The additional peaks appearing below 210 K represent new diffraction plane, which is indexed by hexagonal unit cell. ^{31}P NMR T_1 studies as a function of temperature at 81 MHz, revealed a single minimum of about 100 ms around 150 K. This observation is explained in terms of Miller and Gutowsky's two-phase model [41], through which they concluded that TMA- Phosphate contains two phases one with imperfections and another one without imperfections. ^{31}P NMR T_1 studies yielded an activation energy of 15 ± 2 kJ/mol, $\tau_{co} = (6 \pm 2) \times 10^{-15}$s for isotropic reorientation of all PF_6 ions.

Table 4.5. Characteristic parameters of TMA-Phosphate [50]

Structure	Tetragonal
Space group	P4/ nmm
Cell dimensions	a = 8.436 Å and c = 6.089 Å
Density	1.68 mg m^{-3}
PF_6	4 mm
P-F (axial 1)	1.585 Å
P-F (axial 1)	1.591 Å
P-F (equatorial)	1.568 Å
F-P-F	90º or 180º
$(CH_3)_4$	$\bar{4}3m$
N-C	1.486 Å
C-H	1.06 Å
C-N-C	109.5º
N-C-H	107º
N-C-H	112º

4.2.3 Results and discussion

^{1}H NMR second moment (M_2) measurements are carried out, as a function of temperature in the temperature range 300 – 77 K, at 7 MHz using a home made wide-line NMR spectrometer described in Chapter 2 [52]. Second moment is calculated from the derivative of the absorption signal recorded using lock-in detection as described in Chapter 1.

^{1}H NMR spin lattice relaxation time (T_1) measurements are carried out, as a function of temperature, at three larmor frequencies 21.34 MHz, 16.1 MHz and 11.4 MHz, in the temperature range from 350 K down to liquid helium temperatures using a home made pulsed NMR spectrometer described in Chapter 2. Inversion recovery pulse sequence is used for the measurement of T_1 through out the temperature region studied.

^{19}F NMR spin lattice relaxation time (T_1) measurements are carried out, as a function of temperature, at two larmor frequencies 21.34 MHz and 16.1 MHz, in the temperature range from 320 K down to liquid helium temperatures. Inversion recovery pulse sequence is used for the measurement of T_1 except at higher temperatures where T_1 is higher than 1 s, saturation burst sequence is used. For both the nuclei studied (^{1}H and ^{19}F), the magnetization recovery is found to be single exponential within the experimental error throughout the temperature region studied.

4.2.3.1 Second moment

The second moment determined as a function of temperature in the range 300 -77 K is shown in Fig. 4.7. The second moment value remains almost constant of about 3 (± 0.2) G^2 in the temperature range 300 -180 K within the experimental error. Below 180 K, the signal starts broadening and second moment increases monotonically with the decrease of intensity. The lowest temperature at which the signal can be detected in this compound is 155 K with a second moment of 18 (±1) G^2. Below this temperature, the signal is completely buried in noise and hence no second moment measurements are possible. Attempt to measure second moment at 77 K, by directly immersing the sample tube in liquid nitrogen dewar has also failed due to poor signal to noise ratio.

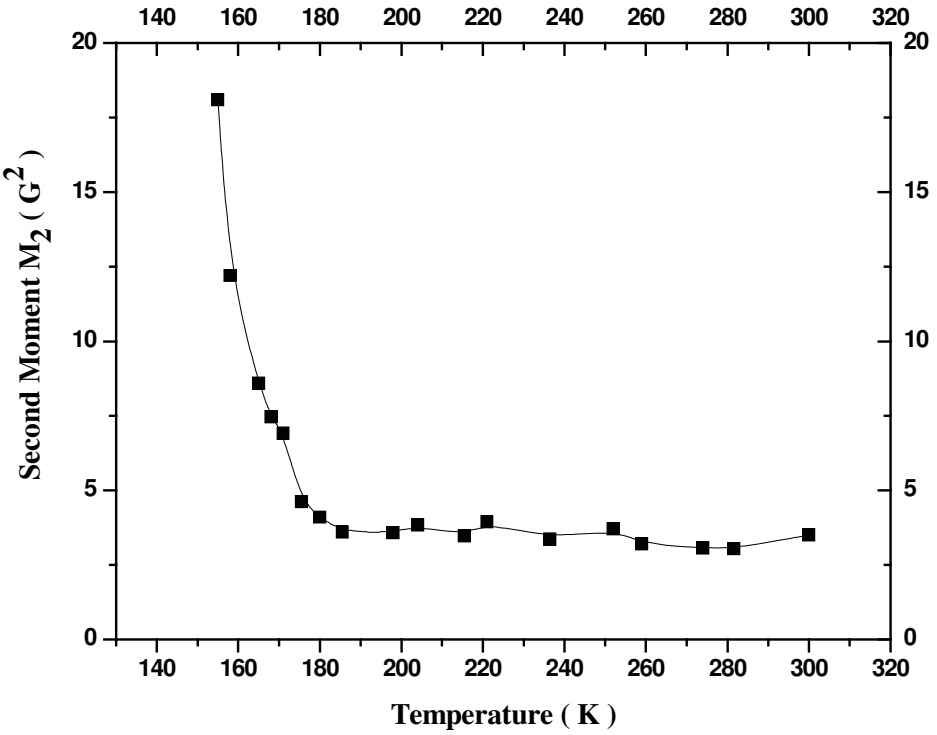

Fig. 4.7 ^{1}H NMR Second moment data of TMA-Phosphate at 7 MHz in the temperature region 300 -155 K; the line is guide to the eye.

The theoretical dipolar second moment for a rigid array of nuclei in the crystal lattice can be calculated using the expression of Van Vleck [53]. There are many second moment simulation studies reported in the literature including those for Tetramethylammonium ion in different complexes [54-60]. The rigid lattice second moment can be calculated for a rigid $(CH_3)_4N$ ion using the formula [60]

$$M_2 = \frac{9}{10}\frac{\gamma^2\hbar^2}{r^6} + \frac{81}{20}\frac{\gamma^2\hbar^2}{R^6} + M_{HT} \ , \qquad (4.13)$$

where γ = 2.675 x 10^4 G^{-1} s^{-1} is the nuclear gyromagnetic ratio of protons and M_2 is measured in G^2. Following Albert et al [5], we have used r = 1.78 Å as the distance between the protons belonging to the same CH_3 group and R = 3.04 Å as the average

distance between the protons belong to different groups, for the second moment calculations. The high temperature residual second moment M_{HT} is considered to be 1 G^2 [62] and the estimated rigid lattice M_2 value is found to be 28 G^2 [59]. In the present investigations, the observed M_2 is only 18 G^2 at 155 K. However, second moment plot shows the tendency to increase further to rigid lattice limit at lower temperatures. Hence, the tendency of the second moment to reach its rigid lattice limit as well as the disappearance of the signal at 77 K suggest that, molecular motions responsible for motional narrowing of the signal start freezing at temperature below 180 K. We can estimate the activation energy from the formula $E_a = 155\ T_C$ J/mol [58], where T_C is the temperature at which the NMR spectrum narrows. The activation in the present investigation yields (for T_C = 155 K) 24 kJ/mol suggesting the activation energy should be lower than this value. The observed plateau second moment of about 3 G^2 in the high temperature region suggests that both TMA and methyl groups reorientations are active down to 180 K and below which, motions of both the groups start freezing. The present investigations show no resolved plateau in second moment, (two plateau regions are expected for TMA compounds) indicating that the two motions do not have widely differing correlation frequencies [60]. Since the line narrowing observed in this complex seems to occur in a single step, it can be concluded that the individual C_3 reorientation of four CH_3 groups in the cation and the overall reorientation of the cation as a whole occur simultaneously at a very narrow interval of temperature. Similar behaviour has been observed in $(CH_3)_4NCdCl_3$ [59], $(CH_3)_4NCl$ [60], and $((CH_3)_4N)_2MX_6$ (M = Pt, Te and Sn, X = Cl and Br) compounds [9, 63]. These results are consistent with our T_1 measurements discussed in the next section.

4.2.3.2 Spin lattice relaxation time

Figure 4.8 shows the variation of ^{1}H and ^{19}F NMR spin lattice relaxation times (T_1) with inverse temperature (1000/T) over the entire temperature range studied. The ^{31}P T_1 data at 81 MHz in the same compound, reported by Reynhardt et al [51] is also included for comparison. The T_1 data are analyzed in two parts (a) ^{1}H NMR spin lattice relaxation time studies as shown separately in Fig. 4.9 and (b) ^{19}F NMR spin lattice relaxation time studies as shown separately in Fig. 4.10.

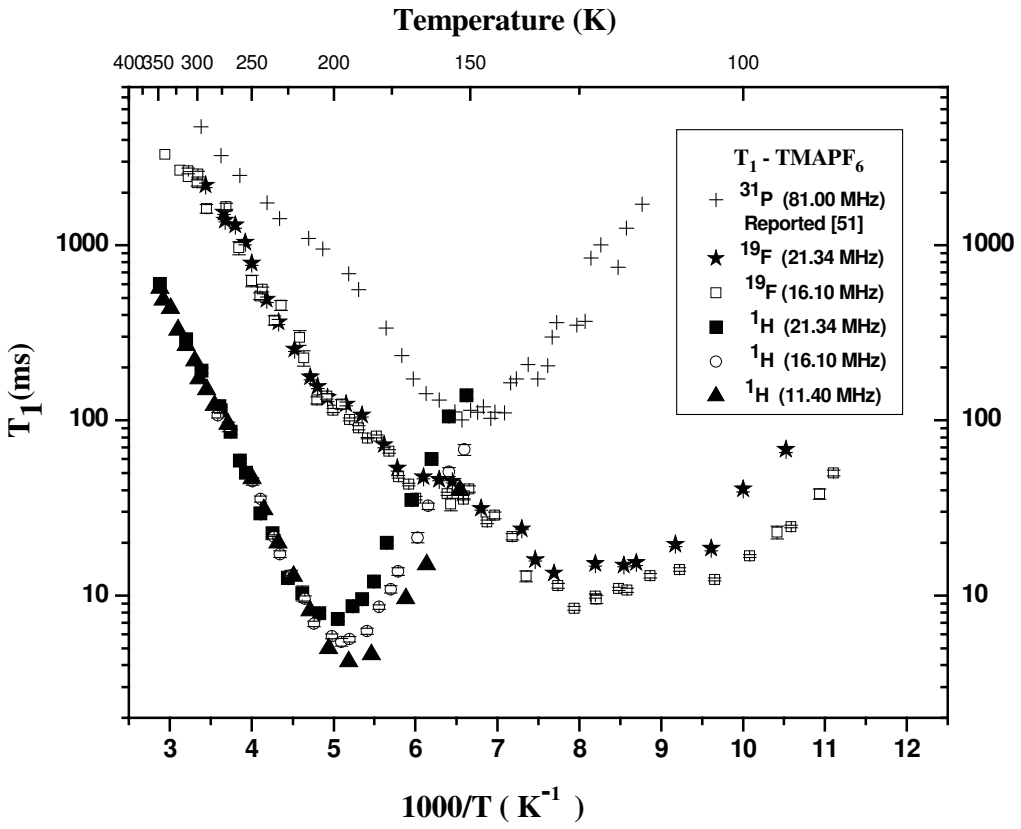

Figure 4.8 ^{1}H (11.4, 16.1 and 21.34 MHz), ^{19}F (16.1 and 21.34 MHz) and ^{31}P (Reynhardt et al [51] at 81 MHz) NMR T_1 versus 1000/T in TMA-Phosphate in the entire temperature range studied.

(a) ^{1}H NMR T_1 analysis

Figure 4.8 shows only the ^{1}H NMR spin lattice relaxation time data at three larmor frequencies (11.4, 16.1 and 21.34 MHz). Initially T_1 decreases with decrease in temperature from 350 K giving rise to a single asymmetric minimum instead of two expected minima, corresponding to each symmetric groups (TMA and CH_3) present in the compound, as in most of the Tetramethylammonium compounds. T_1 minima of about 4.20, 5.42 and 7.35 ms observed respectively at 11.4, 16.1 and 21.34 MHz, around 190 K, suggest that this single minimum is unlikely to be solely due to the single

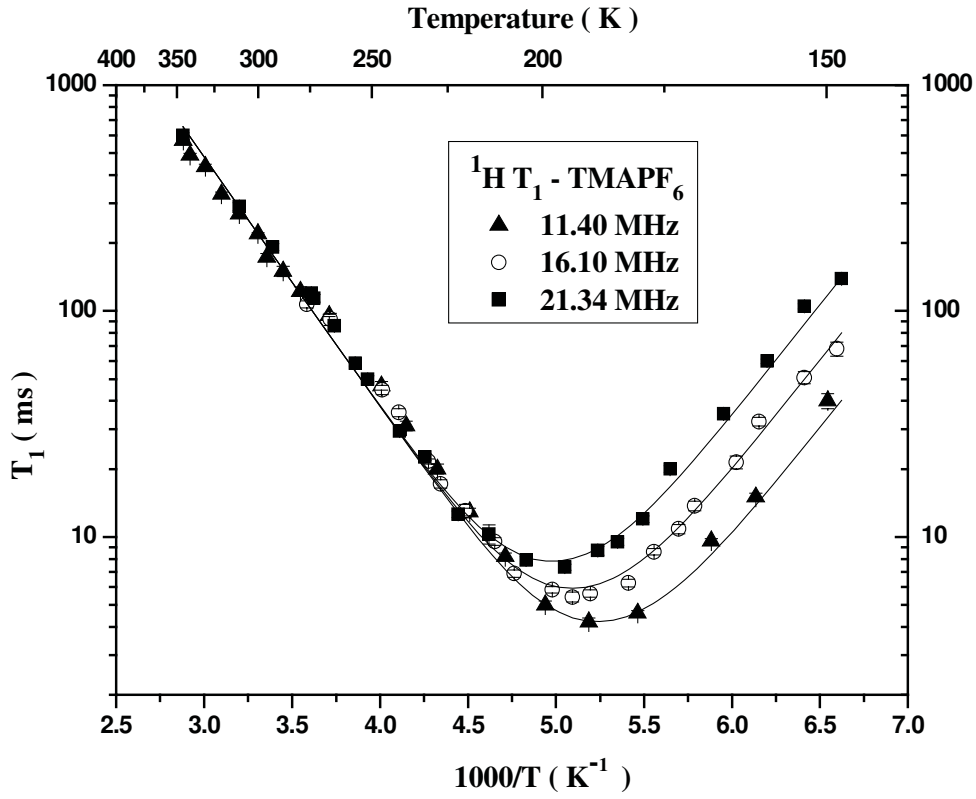

Figure 4.9 ^{1}H NMR T_1 data of TMA-Phosphate at 11.40 MHz (▲), 16.10 MHz (○) and 21.34 MHz (■) . Solid line represents the Albert et al model fit [5].

group reorientation, but due to the resultant of both CH_3 and TMA group reorientations.

On further decrease in temperature, T_1 increases with a decrease in signal intensity, at all frequencies studied and hence we could make measurements only up to 150 K. The signal to noise ratio decreases drastically and signal vanishes completely below 150 K. The signal did not reappear, as in the case of TMA - Selenate, below 150 K and down to liquid helium temperatures.

The ^1H T_1 behaviour can be explained using Albert et al [5] model as explained in the section 4.1.4.1. Here also, assuming that the TMA ion is an undistorted tetrahedron, with C-H distance of 1.09 Å and C-N distance of 1.5 Å, the values of r and R are calculated to be 1.78 Å and 3.04 Å respectively. The values of A and B are found to be A= 8.05 x 10^9 sec^{-2} and B = 4.61 x 10^9 sec^{-2}. From Eqn. 4.7, at a frequency of 21.34 MHz, one expects a minimum of 20.27 ms corresponding to the TMA tumbling motion, at $\omega\tau_{c1}$ = 0.616 and another minimum of 11.74 ms corresponding to the CH_3 group reorientation at $\omega\tau_c$ = 0.616. However, present investigation reveals only one broad asymmetric minimum. The Albert et al model (expressed by equation 4.15 and used for the analysis of TMA- Selenate in the previous section) fits well to the present ^1H NMR T_1 data for TMA- Phosphate, at all frequencies studied and the fit curves are shown in Fig. 4.9. The fit parameters (activation energies and pre-exponential factors) obtained for all frequencies are within the error limits (shown in the parentheses) and are given in Table 4.6.

The observed activation energies for both CH_3 and $(CH_3)_4$ ion in the present compound are lower than that observed in TMA- Selenate and hence single minimum occurs at much lower temperature than that observed in the later compound. The activation energy obtained from T_1 results (22 kJ/mol) is in excellent agreement with that

(lees than 24 kJ/mol) obtained from second moment studies. Also, these values are less than that of $((CH_3)_4N)_2SO_4$ (28 and 45 kJ/mol), $TMAClO_4$ (21.2 and 32.9 kJ/mol) [23] and $(CH_3)_4NX$ (X = Cl, Br and I) (23-28 and 37-54 kJ/mol) [8]. However, they are in good agreement with those reported for other TMA compounds [64]. The CH_3 group activation energy compare well with reported value of 15-17 kJ/mol and the $(CH_3)_4$ group activation energy is slightly lesser than the reported value of 30-37 kJ/mol, for the room temperature phase of $[(CH_3)_4N]_2$ MX_4 (M=Pb and Pt ; X = Cl and Br) [24]. This indicates an increased volume for reorientation of the groups as compared to pure salts**.** This could be correlated to the increased volume (higher metal ion radius) available for the motion of the symmetric groups.

(b) ^{19}F NMR T_1 analysis

Figure 4.10 shows the ^{19}F NMR spin lattice relaxation time data at two larmor frequencies (16.1 and 21.34 MHz). Initially T_1 decreases with decrease in temperature from 350 K giving rise to a prominent single broad asymmetric minimum at much lower temperatures (around 100 K). On further decrease in temperature, T_1 increases with a decrease in signal intensity, at both the frequencies studied. Hence we could make measurements only up to 85 K and the signal to noise ratio decreases drastically below 85 K and the signal vanishes completely below 80 K. No measurements were possible down to liquid helium temperatures.

Theory

The analysis of the fluorine relaxation time T_1 is rather complicated compared to that of proton T_1. Several MPF_6 compounds have been investigated by Gutowsky et al [42] by ^{19}F NMR second moment and relaxation time studies. Albert et al [46] have observed the cross relaxation effects between proton and fluorine by ^{1}H and ^{19}F NMR relaxation time studies in NH_4PF_6. ^{19}F spin lattice relaxation may occur due to several reasons. Four main contributions to ^{19}F relaxation are : (a) the intra-ionic F-F interaction. (b) intra ionic F-H

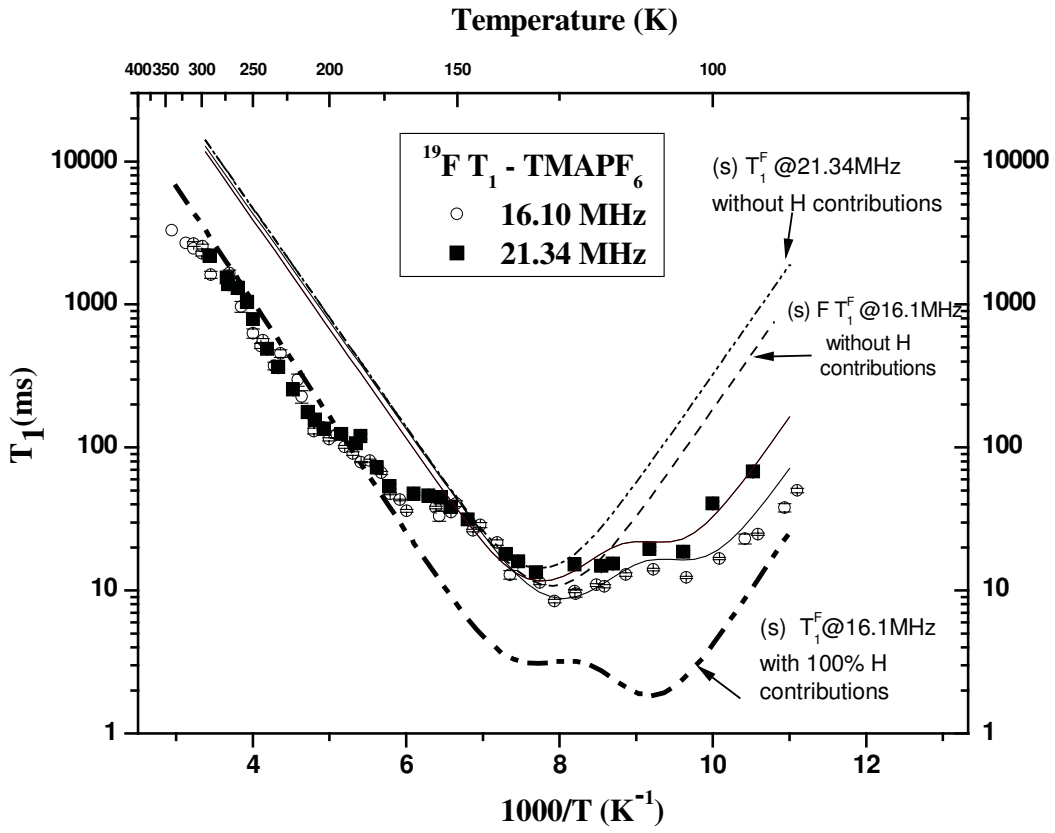

Figure 4.10 ^{19}F NMR T_1 data of TMA-Phosphate at 16.10 MHz (○) and 21.34 MHz (■) . Dotted lines show the simulations (s) considering only the PF_6 reorientation without considering the cross relaxation from proton. Solid lines represent the fit to Albert et al model with cross relaxation fit [46].

interaction. (c) P-F interactions and (d) interionic F-F interactions. The P-F contribution is only about 3% of the total and is neglected. Further, since the larmor frequencies of P and F differ by a factor of ≈ 0.432, P-F cross relaxation will not play a significant role in relaxation process. However, the cross relaxation between F and H cannot be neglected. In fact it is a prominent source for relaxation at least at higher temperatures, because the larmor frequencies of F and H differ only by a factor of 1.063. Thus ^{19}F spin lattice relaxation occurs due to the magnetic dipole – dipole interactions modulated by both the random reorientations of the PF_6 ions and random reorientation of the overall cation or methyl group.

In the high temperature region (T > 155 K), the fluorine relaxation is too fast to affect spin-lattice relaxation, and hence the minima observed in the ^1H T_1 and ^{19}F T_1 values are due to the reorientation of protons. In accordance with the second moment data, the high-temperature proton T_1 minimum is assigned as due to the simultaneous motions of both overall rotation of the TMA ion about the N-P bond axis and reorientation of the methyl groups about C_3 axis. The relaxation rate for the fluorine nucleus can then be written as [61, 65-67]

$$\frac{1}{T_1^F} = R_F = \frac{2}{3}\gamma_F^2 \Delta M_{FF}\ g(\omega_F, \tau_F) + \frac{1}{2}\gamma_F^2 \Delta M_{FP}\ g_F(\omega_{PF}, \tau_F) + \frac{5}{48}\gamma_F^2 \Delta M_{FH}\ g_F(\omega_{HF}, \tau_F) + \frac{3}{16}\gamma_F^2 \Delta M'_{FH}\ g_F(\omega_{HF}, \tau_F), \quad (4.14)$$

where

$$g(\omega_F,\tau_F)=\frac{\tau_F}{1+\omega_F^2\tau_F^2}+\frac{4\tau_F}{1+4\omega_F^2\tau_F^2} \tag{4.15}$$

$$g_F(\omega_{PF},\tau_F)=\frac{\tau_F}{1+(\omega_P-\omega_F)^2\tau_F^2}+\frac{3\tau_F}{1+\omega_F^2\tau_F^2}+\frac{6\tau_F}{1+(\omega_P+\omega_F)^2\tau_F^2} \tag{4.16}$$

and

$$g_F(\omega_{HF},\tau_F)=\frac{\tau_F}{1+(\omega_H-\omega_F)^2\tau_F^2}+\frac{3\tau_F}{1+\omega_F^2\tau_F^2}+\frac{6\tau_F}{1+(\omega_H+\omega_F)^2\tau_F^2}\ . \tag{4.17}$$

In the above equations, $\gamma_F = 2.5166 \times 10^4\ G^{-1}\ s^{-1}$ is the gyromagnetic ratio of the fluorine nucleus; τ_F is the correlation time describing the orientations of the PF_6 ions; ω_F, ω_H and ω_P are larmor frequencies. For $\omega_F = 21.34$ MHz, the corresponding ω_H is 22.68 MHz and ω_P is 9.18 MHz.

The quantities ΔM_{FF} and ΔM_{FP} in Eqn. 4.14 are the changes in the apparent second moment of the fluorine resonance, in G^2, associated with the random reorientations of the PF_6 ions. The intraionic contributions to ΔM_{FF} and ΔM_{FP} depend upon the P-F bond distance in the octahedral ion. If one takes this value as 1.58Å [50], these two contributions are found be 12 and 1.7 G^2, respectively [42]. ΔM_{FH} and $\Delta M'_{FH}$ represent the reduction in second moment for the H-F interactions for spherically averaged TMA ion and stationary PF_6 ions respectively. The ΔM_{FH} and $\Delta M'_{FH}$ values are assumed to be respectively, 3.1 and 3.8 G^2 for tetrahedral symmetry for the cation [46]. Considering these factors, one can rewrite the Eqn. 4.14 as

$$\frac{1}{T_1^F}=5.066\times10^9\ g(\omega_F,\tau_F)+0.5383\times10^9\ g_F(\omega_{PF},\tau_F)+$$
$$c_1\ 2.045\times10^9\ g_F(\omega_{HF},\tau_F)+c_2\ 4.5126\times10^9\ g_F(\omega_{HF},\tau_F)\ , \tag{4.18}$$

The theoretical trends of the fluorine relaxation times expected from above Eqn. 4.18. are seen to be well reproduced in the experimental data (Fig.4.10.). In particular, the minimum at $(\omega_H - \omega_F)\,\tau_F \approx 1$ (i.e $\tau_F \approx 1.17 \times 10^{-7}$ s, which occurs at 108 K) and a hump at $\omega_F\,\tau_F \approx 1$ (i.e., $\tau_F \approx 7.46 \times 10^{-8}$ s, which occurs at 111 K) which are expected [68] from the form of Eqn. 4.17 are well reproduced in the experimental fluorine relaxation time curve. If the contribution from the proton is neglected, i.e., considering only first two terms in the Eqn. 1.41, one gets single T_1 minimum of 13.34 ms at 21.34 MHz and 10.06 ms at 16.1 MHz as shown by the dotted lines in the Fig. 4.10. Further, if one considers proton relaxation is efficient throughout the temperature region studied, then the ^{19}F NMR T_1 data should have been followed by the thick dotted line shown in the Fig. 4.10. However, experimental T_1 data follows this trend from higher temperatures to about 155 K and below this temperature, it deviates significantly. It is interesting to note that, at the same temperature i.e., 155 K the ^1H NMR signal becomes very week and then vanishes completely as observed both in second moment measurements as well as in T_1 measurements. Considering all these factors, one can conclude that both methyl and TMA groups freeze below this temperature. However, still there is a finite contribution from some protons, which are still actively relaxing fluorine nuclei. By considering this model to fit the present experimental results, it may be concluded from the observed values of C_1 (0.089) and C_2 (0.1) that, the number of protons that contribute at most may be about 10% of the total number of protons. The best-fit parameters are given in table 4.6.

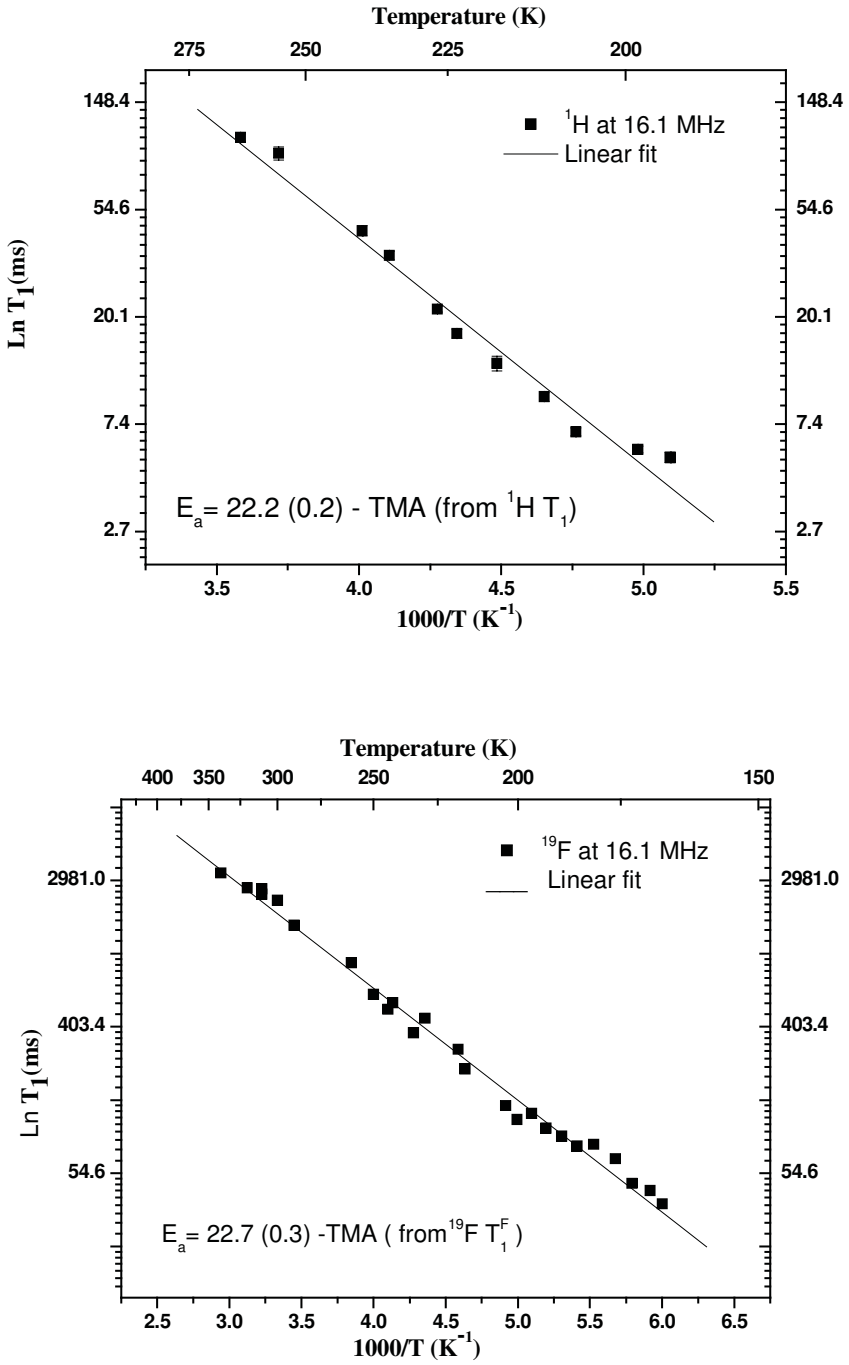

Figure 4.11 Estimation of activation energy for TMA ion in TMA- Phosphate from the linear portion of the high temperature sides of the ^{1}H T_1 and ^{19}F T_1 minima.

Table 4.6 Motional parameters for TMA-Phosphate obtained from ^{1}H T_1 and ^{19}F T_1 fit to models [5, 46].

Symmetric group	Activation energy (kJ/mol)	Pre-exponential factor (10^{-13} s)
Methyl	16.8 (0.5)	2.81 (1)
TMA	22 (1)	0.15 (0.02)
PF_6	15(1)	0.06(0.01)

Also, Eqns. 4.14 to 4.17 suggest that the linear portions of the high temperature side of the ^{1}H T_1 and ^{19}F T_1 minima should yield almost same activation energy. Indeed, the high-temperature linear portion of the ^{19}F T_1 data (Fig. 4.11.), gives an activation energy of 22.6 (0.5) kJ/mole, in excellent agreement with that obtained from the high-temperature T_1^H data (Fig. 4.9), 22 (±1) kJ/mole. Fig. 4.11 shows the linear portions of high temperature sides of T_1 from which the activation energies have been estimated. Similar behaviour is observed in $(CH_3)_3NPF_5$ by McDowell et al [67]. However, ^{1}H NMR T_1 data appear not to get affected by the fluorine nuclei.

Reynhardt et al [51] have explained ^{31}P NMR T_1 results of TMA-Phosphate as due to the PF_6 reorientations and hence reported the motional parameters of the PF_6 ions. Present experimental results yield motional parameters, which are in excellent agreement with the reported values. However, the existence of two phases, one with imperfections

and another without imperfections as reported by Reynhardt [51] seems not to change the surrounding of at least the cation.

4.2.4 Conclusions

^{1}H T_1 measurements at all frequencies have shown single asymmetric minimum and is attributed to simultaneous reorientations of both CH_3 and $(CH_3)_4N$ groups. Second moment measurements made at 7 MHz also supports this. Cross correlation between proton and fluorine has been invoked to account for the observed ^{19}F T_1 data.

References

1. Latanowicz L, Medycki W and Jakubas R. *J. Phys. Chem. A*, **109(14)**, 3097 (2005).
2. Latanowicz L. *J. Phys. Chem. A*, **108(51)**, 11172 (2004).
3. Woessner DE and Snowden BS. *J. Chem. Phys.*, **47**, 2367 (1967).
4. Andrew and Canepa PC. *J. Magn. Reson.*, **7**, 429 (1972).
5. Albert S, Gutowsky HS and Ripmeester JA. *J. Chem. Phys.,* **56(7)**, 3672 (1972).
6. Albert S and Ripmeester JA. *J. Chem. Phys.*, **58(2)**, 541 (1973).
7. Tsuneyoshi T, Nakumara N and Chihara H. *J. Magn. Reson.,* **27**, 191 (1977).
8. Furukawa Y, Kiriyama H and Ikeda R. *Bull. Chem. Soc. Jpn.*, **54**, 103 (1981).
9. Prabhumirashi LS, Ikeda R and Nakamura D. *Ber. Bunsenges. Phys. Chem.*, **85**, 1142 (1981).
10. Rao CNR and Rao KJ. *Phase Transitions in Solids.* Mcgraw-Hill, Newyork, 1978.
11. Serr BR, Heckert G, Rotter HW, Thiele G and Ebling D. *J. Mol. Struct.*, **348**, 95 (1995).
12. Michael Malchus and Martin Jansen. *Z. Naturforsch.* **53b**, 704 (1998).
13. Iizumi M, Axe JD, Shirane G and Shimaoka K. *Phys. Rev. B.*, **15(9)**, 4392 (1979).
14. Blinc R, Južnič S, Rutar V, Seliger J and Žumer S. *Phys. Rev. Lett.,* **44**, 609 (1980).
15. Arend H, Muralt P, Plesko S and Altermatt D. *Ferroelectrics*, **24**, 297 (1980).
16. Shozo Sawada, Yoshihiro Shiroishi, Akitoshi Yamamoto, Masaaki Takashige and Mutsumi Matsuo. *J. Phys. Soc. Jpn.*, **43(6)**, 2101 (1977).

17. Shozo Sawada, Yoshihiro Shiroishi, Akitoshi Yamamoto, Masaaki Takashige and Mutsumi Matsuo. *J. Phys. Soc. Jpn*., **44(2)**, 687 (1978).

18. Keizo Horiuchi, Shinsaku Uezato, Yumiko Yogi, Akihiko Abe, Takanori Fukami, Ryo Takeishi and Ryuichi Ideda. *Phys. Rev.,* **B72**, 174114 (2005).

19. Sato S, Endo M, Hara N, Nakamura D and Ikeda R, *J. Mol. Struct.,* **345**, 197 (1995).

20. Bloembergen N, Purcell EM and Pound RV. *Phys. Rev.*, **73 (7),** 679 (1948).

21. Woessner DE. *J. Chem. Phys.,* **36**, 1291 (1962).

22. Oreilly DE and Tsang T. *J. Chem. Phys.*, **46**, 1 (1967).

23. Tsuneyoshi T, Nakamura N and Chihara H. *J. Magn. Reson*. **27**, 191 (1977).

24. Sato S, Ikeda R and Nakamura D. *Ber. Bunsenges. Phys. Chem.* **91**, 122 (1987).

25. Yano H, Furukawa Y, Kuranaga Y and Okuda T. *J. Mol. Struct.*, **520**, 173 (2000).

26. Senthil Kumaran S, Ramesh KP and Ramakrishna J. *Mol. Phys*. **99(16)**, 1373 (2001).

27. Sarma BS and Ramakrishna J. *Curr. Sci*., **53**, 459 (1984).

28. Latonowicz L. J. *Concept. Magn. Reson. A*. **27(1)**, 38 (2005).

29. Horsewill AJ. *Progr. in Nucl. Magn. Reson. Spectroscopy,* **35,** 359 (1999).

30. Svare I, Raaen AM and Finland WO. *Physica B.* **128,** 144 (1985).

31. Svare I, Raaen AM and Thorkildsen G. *J. Phy. C: Solid State Phys.*, **11**, 4069 (1978).

32. Ylinel EE, Tuohi JE and Niemela LKE. *Chem. Phy. Lett.* **24**, 447 (1974).

33. Clough S, Horsewill AJ, Johnson, MR, Sutchliffe JH, Tomsah IBI. *Mol. Phys.*, **81**, 975 (1994).

34. Srenivasan R. *MTP International Review of Science*, Magnetic Resonance, Series II (ed. McDowell, C.A.) London, P209 (1975).

35. Clough S, Horsewill AJ, Johnson MR, Sutchliffe JH and Tomsah IBI. *Mol. Phys.*, **81**, 975 (1994).

36. Ingman LP, Punkkinen M, Vuorimaki AH and Ylinen EE. *J. Phy. C: Solid State Phys.,* **18**, 5033 (1985).

37. Tuohi JE and Ylinen EE, *Phys. Scr.*, **13**, 253 (1976).

38. Ingman LP, Punkkinen M, Ylinen EE and Dimitropoulos C. *Chem. Phys. Lett*. **125**, 170 (1986).

39. Koksal F, Rossler E and Sillescu H. *J. Phys. C.* **15**, 5821 (1982).

40. Műller-Warmuth W, Schűler R, Prager M and Kollmar A. *J. Chem. Phys.*, **69(6),** 2382 (1978).

41. Miller GR and Gutowsky HS. *J. Chem. Phys.*, 3**9(8),** 1983 (1963).

42. Gutowsky HS and Albert S. *J. Chem. Phys.*, **58(12),** 5446 (1973).

43. Hiroshi Ono, Shin'ichi Ishimaru, Ryuichi Ikeda and Hiroyuki Ishida. *Bull. Chem. Soc. Jpn.,* **72**, 2049 (1999).

44. Hiroshi Ono, Shin'ichi Ishimaru, Ryuichi Ikeda and Hiroyuki Ishida. Ber. Bunsenges. *Phys. Chem,*. **102**, 650 (1998).

45. Grotte M, Kozak A, Kozil AE and Pajak Z. *J. Phys: Condens. Matter,*. **1,** 7069 (1989).

46. Albert S and Gutowsky HS. *J. Chem. Phys.,* **59(7),** 3585 (1973).

47. Heyns AM and de Beer WHJ. *Spectrochimica Acta,* **39A(7)**, 601 (1983).

48. Staveley LAK, Grey NR and Layzell MJ. *Z. Naturforsch.* **A 18**, 148 (1963).

49. De Beer WHJ and Heyns AM. *Spectrochimica Acta,* **37A**, 1099 (1981).

49A. United States Patents **6773822**, **20040110868**:

OSTI ID: **4572627**, **AD0757883**:

Ugalde L, Bernede JC, Del Valle MA, Díaz RF and LeRay P. *J. Appl. Polymer Science*, **84(10)**, 1799 (2002):
Al-Nakib Chowdhury, Yoshihito Kunugi, Yutaka Harima and Kazuo Yamashita. *Thin Solid Films,* **271**, 1 (1995).

50. Wang Y and Calver LD and Brownstein SK. *Acta Cryst.,* **B36**, 1523 (1980).

51. Reynhardt EC, Jurga S and Jurga K. *Chem. Phys. Let*t.**, 194,** 410 (1992).

52. Mallikarjunaiah KJ and Damle R. *Vignana Bharathi*. **11(1),** 50 (2005).

53. Van Vleck JH. *Phys. Rev.,* **74**, 1168 (1948).

54. Goc R. *J. Magn. Reson.,* **78**, 132 (1998).

55. Goc R. *Comp. Phys. Comm.*, **162**, 102 (2004).

56. Goc R. *Z. Naturforsch.* **58a,** 537 (2003).

57. Blears DJ, Danyluk SS and Bock E. *Journal of Physical Chemistry*. **72(6),** 2269 (1968).

58. Waugh JS and Fedin EI. *Soviet Physics Solid State*, **4**, 1633 (1963).

59. Tung Tsang and Utton DB. *J. Chem. Phys.,* **64(9)**, 3780 (1976).

60. Andrew ER and Canepa PC. *J. Magn. Reson.*, **7,** 429 (1972).

61. Abragam A. *The Principles of Nuclear Magnetism.* Oxford University Press; New York, 1961.

62. Mahajan M and Nageswara Rao BD. *J. Phy. C: Solid State Phys.,* **7**, 995 (1974).

63. Sato S, Ikeda R and Nakamura D. *Ber. Bunsenges. Phys. Chem.***, 91**, 122 (1987).

64. Senthil Kumaran S, Ramesh KP, Ramakrishna J. *Mol. Phys.*, 2001; **99(16)**: 1373.

65. Oreilly DE, Peterson EM and Tsang T. *Phys. Rev.,* **160**, 333 (1967)

66. SCHhwrzLErt R. *Advan. Fluorine Chem.,* 5,3 1 (1965).

67. McDowell CA, Raghunathan P and Williams DS. *J. Magn. Reson.,* 32, 57 (1978).

68. Caron AP, Huttner DJ, Ragle JL, Sherk L and Stengle TR. *J. Chem. Phys.*, 47(8), 2577 (1967).

Chapter 5

NMR Studies in Trichlorogermanates

5.1 Introduction

ABX_3 (A = alkali metal and alkylammonium ion, B = metal atom and X = Cl, Br and I) systems are interesting group of compounds because of the changes in their physical properties due to structural phase transitions. Compounds of the type, $(MR_4)BX_3$, where M = N, P, As, Sb, R = H, D, CH_3 and B = Hg, Zn, Cd, Ca, Cu…. can lead to ferroelectricity [1, 2]. The dynamics of the protonic groups are also interesting in these compounds. The low melting temperatures and good solubilities in common solvents are favorable features in the preparation of these compounds. The feasibility of crystal engineering by anion and cation substitution within related structure types is another additional attractive feature of these compounds [3]. ABX_3 systems with low activation energy are interesting candidates to study tunnelling at low temperatures. The symmetry of the reorienting group can be altered, for example, by substituting a methyl group for a hydrogen atom, and its effects on the dynamics of the system can be studied. Techniques like neutron scattering studies, NMR, heat capacity measurements etc., are extremely used to elucidate different physical properties. This gives the additional insight into the dynamics of the reorienting groups, in relation to the crystal structure. NH_4MF_3 (M = Mn, Zn, Mg, Co) have been investigated using different techniques [4 - 7]. The transition temperature (T_c) in these compounds has been found to decrease with decreasing metal ion radius and anion radius. Low activation energy is observed in a number of ammonium and alkyl substituted ammonium compounds [8 - 9]. Successive replacement of hydrogen by CH_3 groups in ammonium ion according to the formula Me_xNH_{4-x} (Me = methyl, x = 1…4), leads to a larger ionic radius of the cation, which

may result in strong phase transitions. Other than the deviation from spherical symmetry, additional symmetry elements may lead to increased reorientation motions.

Perovskite halides ABX_3 of group IV elements such as Ge, Sn, and Pb have been studied extensively, not only because of their successive phase transitions but also due to the diversity in their electrical properties such as ferroelectricity, ionic and electronic conductivity [10 - 13]. The low oxidation state of group IV elements has an s-electron lone pair and this is the main origin of the interesting structural and electrical properties. According to previous studies, the following general tendencies have been observed: (1) each BX_6 octahedron tends to deform with decreasing atomic number of the B atom and results in the appearance of an isolated pyramidal BX_3 anion [14 - 21] and (2) electronic conductivity appears in bromides or iodides if the distortion from an ideal perovskite is small and the conductivity depends strongly on the lattice constant [22 - 26]. The structural tendencies that appear in this perovskite family are closely related to the hypervalent nature of the central metal, that is, a symmetric trans X-B-X bond known as a three - center four-electron bond (3c - 4e) [12] tends to deform to an asymmetric X-B….X bond with decreasing atomic number of the B metal. Similar behavior is also reported with decreasing temperature for $CH_3NH_3SnBr_3$, where a red semiconducting cubic crystal undergoes a phase transition to an yellow insulator below 229 K accompanied by a distortion of the perovskite lattice [11, 17].

In ABX_3 perovskite halides, the tolerance factor is defined by [27]

$$t = \frac{r_A + r_X}{\sqrt{2}\left(r_B + r_x\right)}, \qquad (5.1)$$

where r_A, r_B and r_x are the ionic radii of A, B and X (halogen) respectively. When t = 1, these systems possess ideal cubic structure. Depending on the relative ionic sizes, perovskites show tetragonal, rhombohedral, orthorhombic, and other types of distortions. Both A and B ions play a major role in determining the symmetry of the structure. It is also known that ABX_3 compounds which have rhombohedral, orthorhombic, or other low-symmetry structure at low temperatures, transform to the cubic phase at high temperatures [28]. At room temperature, the majority of these germanium compounds adopt distorted perovskite–type structures with 3–fold or 3+3 coordination at Ge. In alkylammonium trichlorogermanate (II) compounds, mobile chloride ion is found to be responsible for ionic conductivity and its abrupt change at the phase transitions at high temperatures [29-30].

This Chapter contains the results of proton NMR studies in Trimethylammonium Trichlorogermanate ($(CH_3)_3NHGeCl_3$) and Tetramethylammonium Trichlorogermanate ($(N(CH_3)_4)\ GeCl_3$).

5.2 Trimethylammonium Trichlorogermanate $((CH_3)_3NHGeCl_3)$

5.2.1 Earlier studies

Both $CH_3NH_3GeCl_3$ and $(CH_3)_4NGeCl_3$ have been studied extensively using AC conductivity, temperature dependent single crystal XRD, ^{35}Cl NQR/NMR, quasielastic scattering and many other techniques [12-13, 28-34]. On the other hand, very little work has been reported on trimethylammonium trichlorogermanate, to best of our knowledge. The preparation and Differential Scanning Calorimetry results of this compound are

reported by Poskozim et al [35, 37] and single crystal XRD (at 293 K) results are reported by Möller et al [36]. Möller et al have shown that at room temperature (293 K), the title compound crystallizes in an orthorhombic modification ($Cmc2_1$) with a = 9.537 Å, b = 8.235 Å , c = 12.138 Å and Z = 4, which slightly deviates from cubic system. The characteristic parameters of TriMA- Germanate are given in Table 5.1.

Table 5.1 Characteristic parameters of TriMA-Germanate [36]

Structure	Orthorhombic
Space group	$Cmc2_1$
Cell dimension	a = 9.537 Å
	b = 8.235 Å
	c = 12.138 Å
Density	1.665 g cm^{-3}
Melting point	462 – 464 K [24]

Table 5.2 X-ray powder diffraction data of TriMA-Germanate [36]

d (Å) [Reported 36]	d (Å) [Present study]
6.061	6.060
5.550	5.549
4.768	4.768
4.347	4.346
3.409	3.410
3.115	3.110
3.035	3.032
2.046	2.050

5.2.2 Sample preparation and characterization

Trimethylammonium trichlorogermanate (TriMA-Germanate) is prepared following the method described by Poskozim et al [35]. To begin with, germanium tetrachloride is prepared by the reaction of germanium oxide (Aldrich, 19,947-6) with hydrogen chloride, which is further reduced to $GeCl_2$ with hypophosphorous acid H_3PO_2 (Aldrich, 21,490-6) [37]. Trimethylammonium chloride is prepared by neutralizing the trimethylamine with little excess of hydrogen chloride and crystallized on slow evaporation of water. The TriMA-Germanate is prepared by the addition of equimolar quantities of trimethylammonium chloride to $GeCl_2$-H_3PO_2 media [35]. The reaction can be represented as

$$GeO_2 + H_3PO_2 + 2\,HCl + (CH_3)_3NHCl \rightarrow (CH_3)_3NHGeCl_3 + HPO_2 + 2\,H_2O$$

The resulting colourless precipitate is filtered and dried under vacuum for a few days since the compound is hygroscopic in nature. The sample is characterized using powder XRD, melting point by DSC (heat flow) and our results are in good agreement with those reported in the literature [35, 37] and is shown in Table 5.2. The compound is finely powdered and vacuum-sealed into glass ampoules of 5 mm diameter in helium atmosphere for NMR studies.

The Differential Scanning Calorimetry (DSC) measurements are carried out in the temperature range 130 K to 470 K using Universal V 3.0G TA instrument with a scan rate of 1 kelvin per minute.

5.2.3 Results and discussion

Figure 5.1 shows the variation of ^1H NMR spin lattice relaxation time (T_1) with inverse temperature (1000/T) at 20.53 MHz in the entire temperature range 391 – 5.2 K. The

magnetization recovery is found to be exponential within experimental errors throughout the temperature region studied. The T_1 data are analyzed in three parts: the High Temperature (HT) region (391 - 272 K), the Intermediate Temperature (IT) region (272 - 100 K) and the Low Temperature (LT) region (100 - 5.2 K).

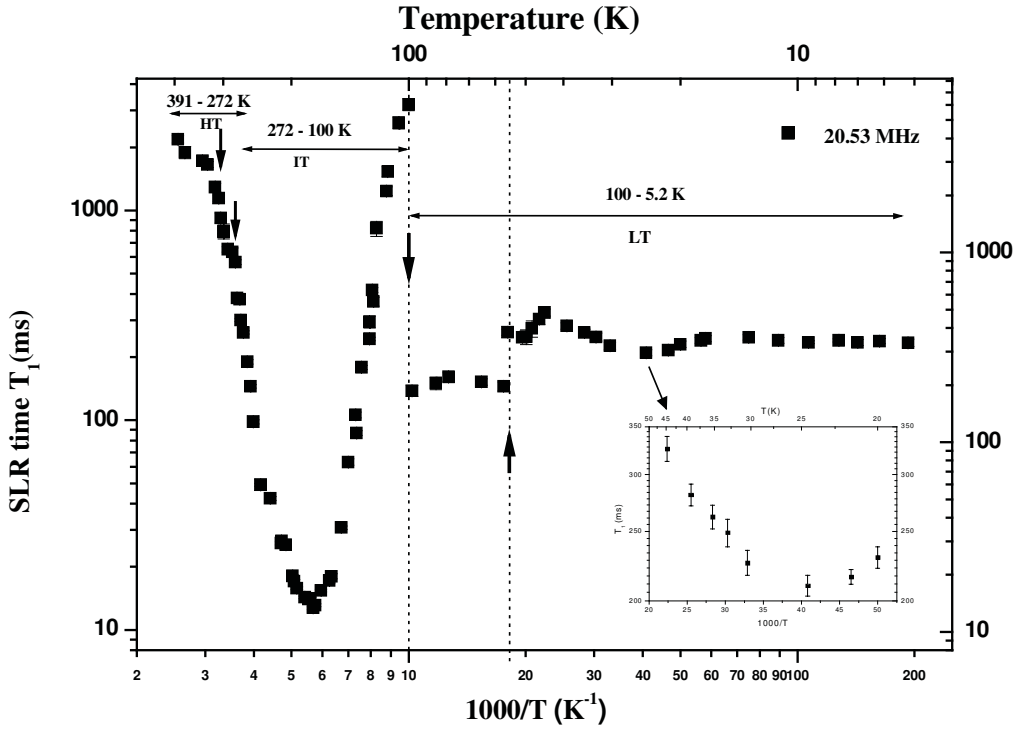

Figure 5.1 ^{1}H NMR T_1 data of TriMA-Germanate at 20.53 MHz in the temperature range 391 – 5.2 K. (Insert : Variation of T_1 in the temperature region 45 - 20 K).

5.2.3.1 High Temperature (HT) region (391 - 272 K)

The high temperature T_1 data in Fig.5.1 is redrawn in Fig. 5.2. in a limited temperature range (391-230 K) for better readability, which clearly shows that, T_1 gradually decreases with decreasing temperature from 391 K exhibiting slope changes at 323 K and 272 K.

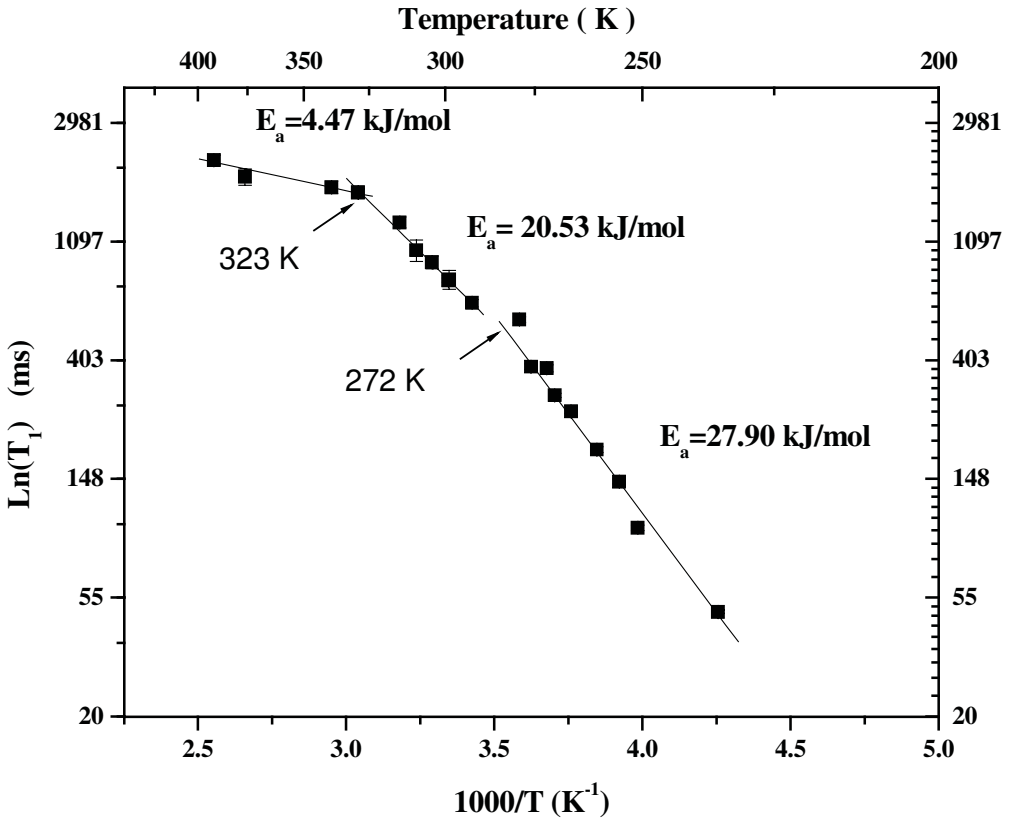

Figure 5.2 T_1 data in the temperature region 391-272 K. Solid lines represent straight line fit.

To substantiate NMR data, we have carried out Differential Scanning Calorimetry (DSC) study over the temperature region 130 – 470 K and is shown in Fig. 5.3. The DSC data reveal four enthalpy peaks: the peak observed around 272 K appears to be a sharp phase transition, where the proton T_1 versus temperature plot has also shown a clear slope change. A sluggish phase transition is observed in DSC in the range 317– 345 K and T_1 also shows a slope change around the same temperature (323 K). In addition, DSC also shows two more clear peaks at 388 K and 465 K. The later peak is attributed to melting point of the compound [37]. Such high temperature phase transitions are also observed in

analogous compounds [38 - 39]. However, our T_1 data do not show any observable change at 388 K, which is close to the highest temperature that can be reached in our experimental set up. The activation energies (E_a) for the trimethylammonium ion are calculated from the slopes of the linear portions of ln (T_1) versus 1000/T graph in the temperature region 230-391 K. Estimated E_a's are 27.90 (below 272 K), 20.53 (in the temperature range 272 - 323 K) and 4.47 kJ/mol (in the range 323-391 K). The E_a is found to decrease at high temperatures and this may be due to increased symmetry, which is generally observed in most of the perovskite halides.

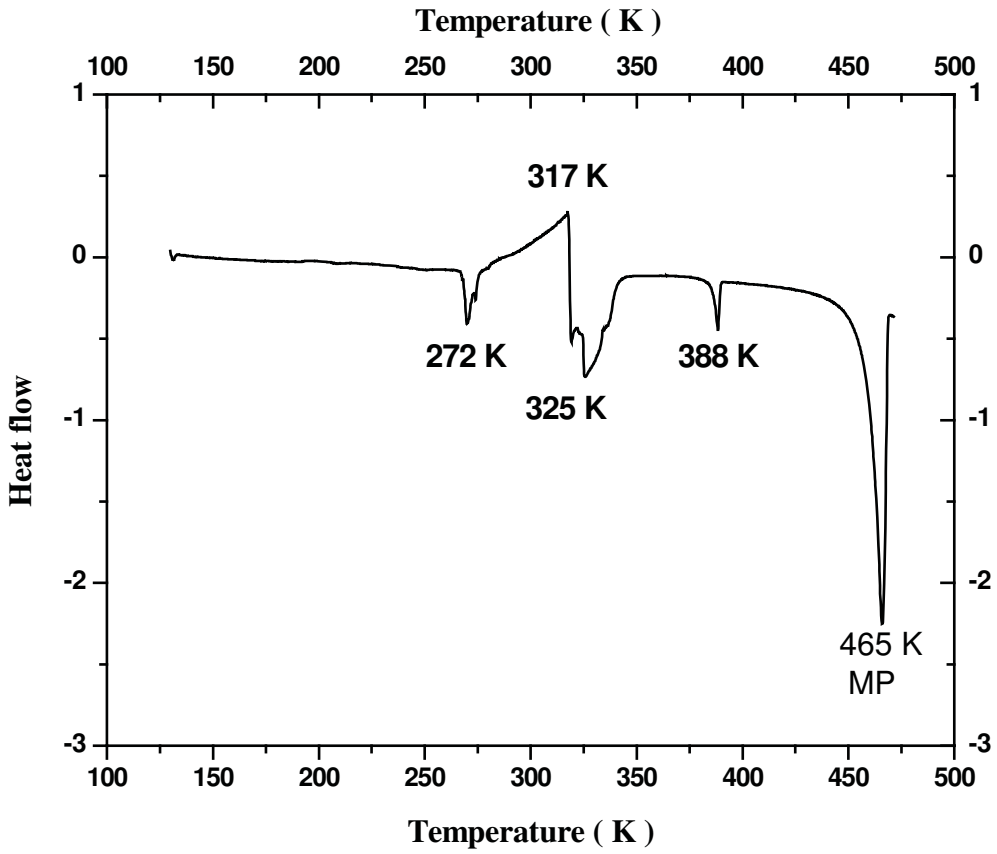

Figure 5.3 DSC data (TriMA-Germanate) in the temperature region 465 - 130 K.

5.2.3.2 Intermediate Temperature (IT) region (272 - 100 K)

Figure 5.4 shows the variation of T_1 with inverse temperature (1000/T). Below 272 K down to 100 K, T_1 data reveal two minima: a shallow one of 25.9 ms around 213 K and another deep one of 12.7 ms around 176 K. On further cooling below 176 K, T_1 increases to a few seconds till about100 K. T_1 data in this temperature region has been analyzed using the modified Ikeda's model [40].

Theory

Ikeda et al [40] have studied the ^{1}H T_1 in several compounds of $(TriMA)_2MX_6$ (M = Pt, Sn and Te and X = Cl, Br and I). They have observed two T_1 minima: one around 220 K and the other around 170 K, which are attributed to trimethyl ammonium ion and methyl group reorientations about their C_3 axes. Ikeda et al have analyzed the observed T_1 variation by assuming the superimposition of two Bloembergen-Purcell-Pound (BPP) curves [41], each of which is given by

$$T_1^{-1} = C\, f(\tau) = C[\,\tau(1+\omega^2\,\tau^2)^{-1} + 4\,\tau(1+4\,\omega^2\,\tau^2)^{-1}]\ , \qquad (5.2)$$

where, C is a constant which depends on the motional mode considered, ω is the Larmor frequency and 'τ' represents a correlation time of the motion which is assumed to obey the Arrhenius equation given by

$$\tau = \tau_0 \exp\,(E_a / RT)\ , \qquad (5.3)$$

where τ_0 and E_a are called pre-exponential factor and activation energy of the respective motion.

In trimethylammonium compounds two reorientations are possible: (1) reorientation of trimethylammonium ion and (2) reorientation of methyl group. The spin lattice relaxation in these systems is due to dipolar interactions between protons of CH_3

groups (intra-methyl) and interaction between protons of different methyl groups belonging to the cation (inter-methyl) modulated by these reorientations.

The relaxation time caused by dipolar interactions between protons within CH_3 groups can be expressed as [42]

$$T_1^{-1}(\text{int}\, ra - CH_3) = \frac{9}{10}\frac{9}{80}\frac{\gamma^4 \hbar^2}{r^6}[A f(\tau_c) + B f(\tau_{c1}) + C f(\tau_{c2})] \ , \qquad (5.4)$$

where

$$\tau_{c2}^{-1} = \tau_c^{-1} + \tau_{c1}^{-1} \qquad (5.4\,a)$$

$$A = (3/2)\sin^4 \delta \qquad (5.4\,b)$$

$$B = \sin^2 2\delta + \sin^4 \delta \qquad (5.4\,c)$$

and

$$C = (1/2)(8 - 3\sin^4 \delta) \ . \qquad (5.4\,d)$$

Here r (1.78 Å) and δ (109°) stand respectively for the inter-proton distance in the CH_3 group, and the angle between the two kinds of rotation axes namely the C-N bond and the N-H bond (C_3 axis). τ_c and τ_{c1} correspond to the correlation times of CH_3 and TriMA ion respectively and τ_{c2} is the effective correlation time.

The relaxation time caused by dipolar interaction between protons belonging to different CH_3 groups within the cation is approximated by [43]

$$T_1^{-1}(\text{int}\, er - CH_3) = \frac{27}{10}\frac{9}{20}\frac{\gamma 4 \hbar^2}{R^6} f(\tau_{c1}) \ , \qquad (5.5)$$

where R (3.04 Å) is the distance between the centers of the triangles formed by the three protons of each CH_3 group. The effective spin lattice relaxation time is given by

$$T_1^{-1} = T_1^{-1}(\text{inter} - CH_3) + T_1^{-1}(\text{intra} - CH_3)\,. \qquad (5.6)$$

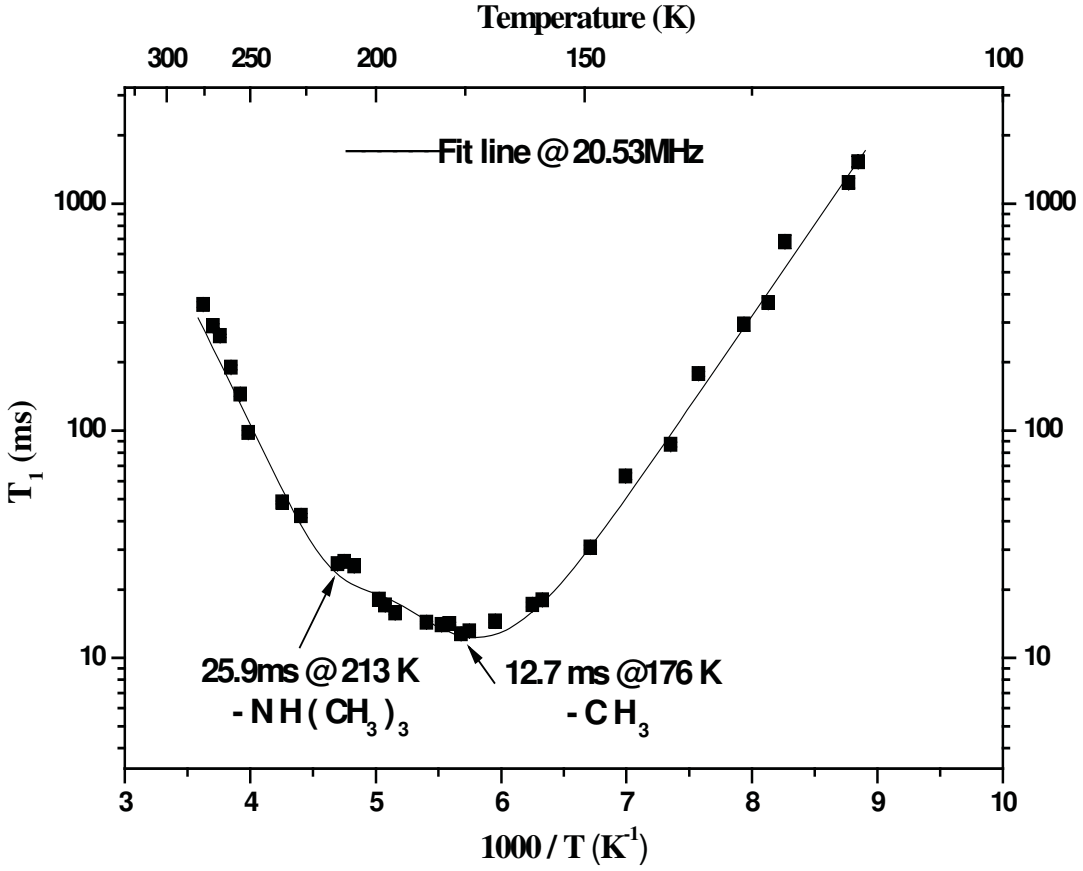

Figure 5.4 T_1 data for TriMA-Germanate in the temperature range 272 -100 K. Solid line represents fit to Ikeda's model [36].

Table 5.3 Motional parameters evaluated from fit of the T_1 data to Ikeda's model for TriMA-Germanate in the temperature region (272 –100 K). The numbers in the parenthesis represent errors.

Group	Activation energy (kJ/mol)	Pre-exponential factor (10^{-13} s)
Methyl (τ_c)	15.4 (0.7)	1.0 (0.04)
TriMA (τ_{c1})	26.9 (0.4)	0.01 (0.002)

A theoretical fit of the T_1 data to Eqn. (5.6) is shown in Fig. 5.4. It is assumed that the dipolar interactions between the N-H proton and the CH_3 protons do not contribute much because of their relatively small effect on spin relaxation and hence are not included in the equation. Similar assumptions have been made by Yano et al. [11]. Ikeda's model fits well with our T_1 data and the best fit parameters for CH_3 and TriMA cation motions are given in the Table 5.3. The observed motional parameters are found to be in good agreement with the literature [40, 44]. On comparing the activation energies of the methyl groups in $(CH_3)_3NHMCl_3$ (M = Cd, Sn and Ge) salts with identical structures, it is found that activation energy of the methyl group increases with decreasing metal ion radius [38, 11]. This can be correlated to the decreased volume available for the motion of methyl group.

5.2.3.3 Low temperature (LT) range (100 – 5.2 K)

In this temperature region, T_1 decreases discontinuously from a few seconds (at 100 K) to about 135 ms and remains almost constant until 57 K as shown in Fig. 5.1. At 57 K, T_1 again increases abruptly to 250 ms and then monotonically increases to 325 ms around 50 K. In the temperature range 50-20 K, T_1 follows a shallow minimum of about 210 ms at 25 K. Below 20 K, T_1 remains almost constant (~ 240 ms) within experimental errors till the lowest temperature of measurement (5.2 K). From the discontinuous change in T_1 at 100 K and 57 K, only qualitative inference on the occurrence of phase transitions can be made.

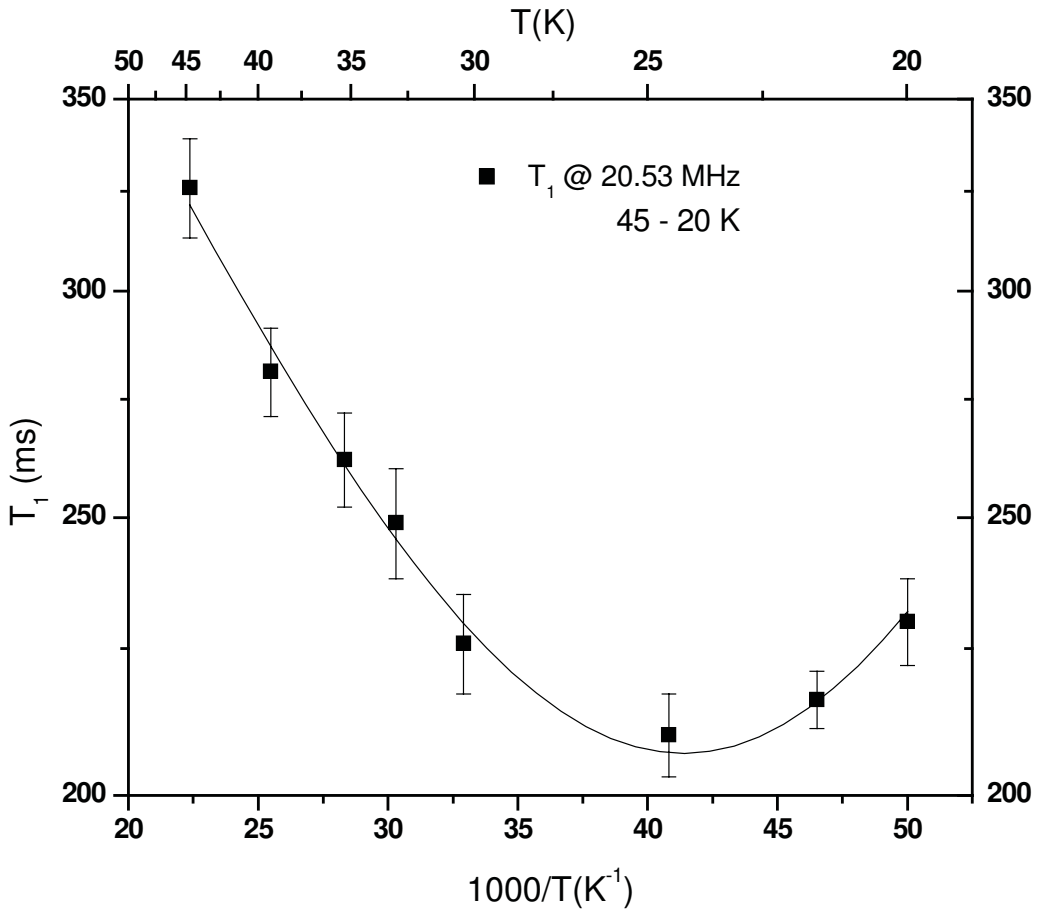

Figure 5.5 T_1 data of TriMA-Germanate in the temperature range 45-20 K: Solid line represents the fit to Köksal model [45].

A large change in T_1 at 100 K may be due to first order phase transition while the 57 K transition may be a second order one. To understand the actual nature of phase transition, additional experimental results like crystal structure determination, DSC measurements below 130 K and ^{35}Cl NQR measurements at low temperature would be required. Yamada et al [30] have observed a change in the symmetry of Cl ion upon phase transition in $AGeCl_3$ compounds using ^{35}Cl NQR experiments. In the present compound also, one can speculate that the low temperature phase transitions may have

resulted in a change in the symmetry of the anion, which may affect the cation environment.

Below 100 K, T_1 results show a broad asymmetric minimum in the temperature region 45 - 20 K which can be explained using the model proposed by Köksal et al [45], They have studied a number of acetates using ^{1}H NMR T_1 measurements and explained their experimental results by considering temperature dependence of tunnel splitting. At low temperatures, only the torsional ground state (n = 0) of the methyl group is occupied and thermal excitations to the first level (n = 1) can be described by the correlation time

$$\tau_c^T = \tau_{co}^T \exp(E_{01}/RT) \ , \qquad (5.7_a)$$

where E_{01} is the energy difference between ground and first excited states of the methyl group. The relaxation occurs when spin-flips are connected with the tunnel splittings. When the tunneling frequency is larger than the Larmor frequency, one can write the expression for the relaxation rate by considering only the intra-methyl interaction and temperature dependence of the tunnel frequency as

$$\frac{1}{T_{AE}} = C_{AE} \sum_{m=-2}^{2} \frac{m^2 \tau_c^T}{1+ < \omega_T >^2 (\tau_c^T)^2} \ , \qquad (5.7_b)$$

where $< \omega_T >^2$ is the average tunnel frequency [46] and is given by

$$< \omega_T >= \frac{\omega_T^0 - \omega_T^1 \exp(-E_{01}/RT)}{1+\exp(-E_{01}/RT)} \qquad (5.7_c)$$

and

$$C_{AE} = \frac{9}{20} \frac{\gamma^6 \hbar^2}{r^6} d_0^2 \ . \qquad (5.7_d)$$

In the above equations, ω_T^0 and ω_T^1 are the ground and first excited torsional tunnel splittings; d_0 is the matrix element of the space part of the dipolar operator between the ground state wave functions of the harmonic oscillator [45].

Table 5.4 Motional parameters evaluated (45 –20 K) using Köksal model for CH_3 group tunneling in TriMA-Germanate.

Parameters	Best fit values
E_{01}	0.32 (±0.01) kJ/mol
τ^T_{c0}	2.4 (±0.05) × 10^{-11} s
C_{AE}	5.4 × 10^9 s^{-2}
ω^0_T	10 × 10^9 s^{-1}
ω^1_T	21 × 10^9 s^{-1}

A theoretical fit of our T_1 data in the temperature range 45 – 20 K to Eqn. 5.7b is shown in Fig 5.5. The best fit parameters are given in the Table 5.4. The motional parameters obtained by the fit are in good agreement with that of Cd $(CH_3COO)_2$ [45], except the activation energy, which is comparatively less, but in reasonable agreement with the results of Senthil Kumaran et al. [39]. Below 20 K, the observed temperature independent T_1 data suggests that only the ground tunnel state is occupied. Similar T_1 behaviour has been observed in many other compounds at low temperatures [45, 47].

5.2.4 Conclusion

The TriMA-Germanate undergoes several phase transitions (at 388, 323, 272, 100 and 57 K) along with thermally activated reorientations of the trimethylammonium and methyl groups. The observed phase transitions are attributed to the chloride ion diffusion (at higher temperatures) and changes in the symmetry of the $GeCl_3$ ions (at lower temperatures), which may have indirect effect on proton spin lattice relaxation time. To understand the actual nature of phase transition, additional experimental results like crystal structure data and ^{35}Cl NQR measurements at low temperature would be interesting. The observed two minima in intermediate temperature region are attributed to reorientation of $NH(CH_3)_3$ and CH_3 symmetric groups and hence corresponding motional parameters are evaluated. It can be noticed that the decrease of activation energy of the TriMA/methyl groups with the decrease metal ion radius, in $TriMABCl_3$ complexes, may be due to the increased volume (higher metal ion (B) radius). At lower temperatures, T_1 results show quantum rotational tunneling of the methyl group.

5.2 Tetramethylammonium Trichlorogermanate ($(CH_3)_4NGeCl_3$)

5.3.1 Earlier studies

Tetramethylammonium Trihalometallates are interesting candidates to study as a number of such compounds have shown interesting physical properties. $TMAHgCl_3$ is ferroelectric between 190 K and 480 K [48, 49]. $TMAHgBr_3$ and $TMAHgI_3$ are ferroelectric between 240 K and 440 K. $TMAGeCl_3$ decomposes around 480 K without showing a curie point and similarly $TMAHgBr_3$ and $TMAHgI_3$ decompose around 450 k. Proton spin lattice relaxation studies in $TMAHgBr_3$ by Sarma et al [49] in the temperature range 488 K –112 K show a single t_1 minimum around 180 K and this result has been attributed to the reorientation of both symmetric groups with close correlation times and subsequent freezing of classical motions below 111 K. Proton t_1 studies in $TMACdBr_3$ [49] in the temperature range 450 –77 K by Sarma et al shows two minima and are attributed to TMA ion reorientation and methyl group reorientation respectively. the proton t_1 study by Vijayaraghavan et al [50] in $TMAPbBr_3$ exhibits phase transition at 270 K and a broad t_1 minimum and these results are explained in terms of two inequivalent TMA ions and reorientation of two methyl groups. Proton second moment and T_1 studies are reported for $TMASnBr_3$ [51, 39, 11]. The observed second moment value of 17 G^2 is less than that reported for rigid TMA ion (~ 28 G^2) and more than the calculated value for the frozen ch_3 motion (9 G^2). This discrepancy has been attributed to small angle reorientation of the methyl group. The observed single broad T_1 minimum at 170 K is less than the expected value for TMA tumbling and higher than the expected value for CH_3 group (at the same operating frequency). This behaviour is explained using small angel orientations of the CH_3 group. The observed hump in the FID for the same

compound is also attributed to the small angle methyl reorientation and non exponential magnetization recovery is also observed in this compound [51].

Moller et al [52] have shown that at room temperature (293 K), TMA-Germanate crystallizes in an orthorhombic modification ($Pna2_1$) with a = 13.096 Å, b = 8.911 Å and c = 9.128 Å and Z = 4. The TMA-Germanate has been reported [34] to reveal five phases in the temperature region 463 – 130 K, in which highest temperature phase being cubic perovskite structure above 424 K. Further, to understand the mechanism of phase transitions, the compound has been studied using AC conductivity, temperature dependent single crystal XRD and ^{35}Cl NQR/NMR techniques [34]. This compound is also investigated by Winkler et al [32] using quasielastic and inelastic neutron scattering and Raman spectroscopic techniques and they have observed the molecular reorientation of the whole TMA and methyl groups in the temperature region 446 – 4 K. Further, the observed structural phase transitions at 170, 200 and 424 K are found to be unrelated to the temperature induced changes of the molecular dynamics. However, to best of our knowledge, ^1H NMR studies as a function of temperature have not been reported in TMA- Germanate. This motivated us to investigate low temperature dynamics in the present compound, as it is expected to be a potential candidate to do so, because analogous compounds have also shown quantum rotational tunneling at lower temperatures [39, 53].

In the present study, the second moment and T_1 measurements have been carried out to invoke similar physical properties in the analogues compound TMA-Germanate and its results are analyzed using appropriate theoretical models pertaining to reorientations of the $(CH_3)_4N$ and CH_3 groups at higher temperatures, along with quantum rotational tunneling at lower temperatures.

5.3.2 Sample preparation and characterization

TMA-Germanate is prepared following the method described by Poskozim et al [35]. All the chemicals used in this preparation are obtained from Aldrich Chem. Co. To begin with, germanium tetrachloride is prepared by the reaction of germanium oxide with hydrogen chloride, which is further reduced to $GeCl_2$ with hypophosphorous acid H_3PO_2 [37]. The TMA-Germanate is prepared by the addition of equal molar quantities of Tetramethylammonium chloride to $GeCl_2$-H_3PO_2 media [35]. The reaction can be represented as

$$GeO_2 + H_3PO_2 + 2\,HCl + (CH_3)_4NCl \rightarrow (CH_3)_4NGeCl_3 + HPO_2 + 2\,H_2O$$

The resulting colourless precipitate is filtered and dried under vacuum for a few days because of its hygroscopic nature. The sample is characterized using powder XRD along with DSC (heat flow) and the results are in good agreement with the literature [52] and is given in Table 5.6. The stereoscopic view of the structure of TMA-Germanate is given in Fig. 5.6 [34]. The compound is finely powdered and vacuum-sealed into glass ampoules of 5 mm diameter in helium atmosphere for NMR studies.

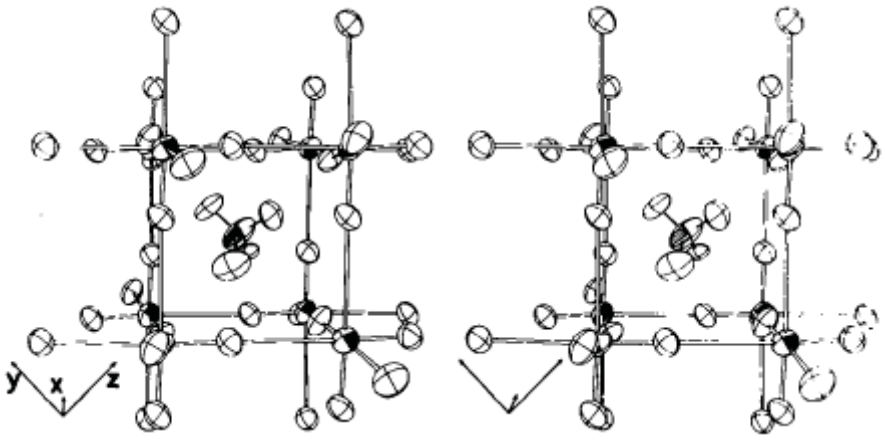

Figure 5.6 Stereoscopic view of the structure of TMA-Germanate. The ellipsoids of Ge and N are shaded. N and four C are at the center [34].

Table 5.5 Characteristic parameters of TMA-Germanate at 293 K [52]

Structure	Orthorhombic
Space group	$Cmc2_1$
Cell dimensions	a = 13.096 Å
	b = 8.911 Å
	c = 9.128 Å
Density	1.56 g cm^{-3}
Ge-Cl (1)	2.321 Å
Ge-Cl (2)	2.262 Å
Ge-Cl (3)	2.299 Å
N-C (1)	1.475 Å
N-C (2)	1.502 Å
N-C (3)	1.410 Å
N-C (4)	1.580 Å
Phase transitions	428, 390, 200 and 170 K [34]

Table 5.6 X-ray powder diffraction data of TMA-Germanate [52]

d (Å) [Reported 52]	d (Å) [Present study]
6.380	6.381
5.720	5.719
5.272	5.270
4.563	4.562
4.453	4.453
3.190	3.189
2.023	2.023
1.690	1.692

5.3.3 RESULTS AND DISCUSSION

5.3.3.1 Second moment

Second moment studies have been carried out as a function of temperature in the range 300 -77 K is shown in Fig. 5.7. The second moment value remains almost constant of about 2.8 (± 0.2) G^2 in the temperature range 300 -160 K within the experimental error. Below 160 K, the signal starts broadening and second moment increases monotonically to 24.8 (±0.5) G^2 at 114 K. The lowest temperature that can be reached with the existing low temperature liquid nitrogen gas flow cryostat is about 114 K and hence the second moment measurements have not been made in the temperature range 114 -77 K. The second moment data at 77 K has been obtained by directly immersing the sample tube in liquid nitrogen dewar. At 77 K, the signal becomes narrow leading to a second moment of 5.5 (± 0.4) G^2.

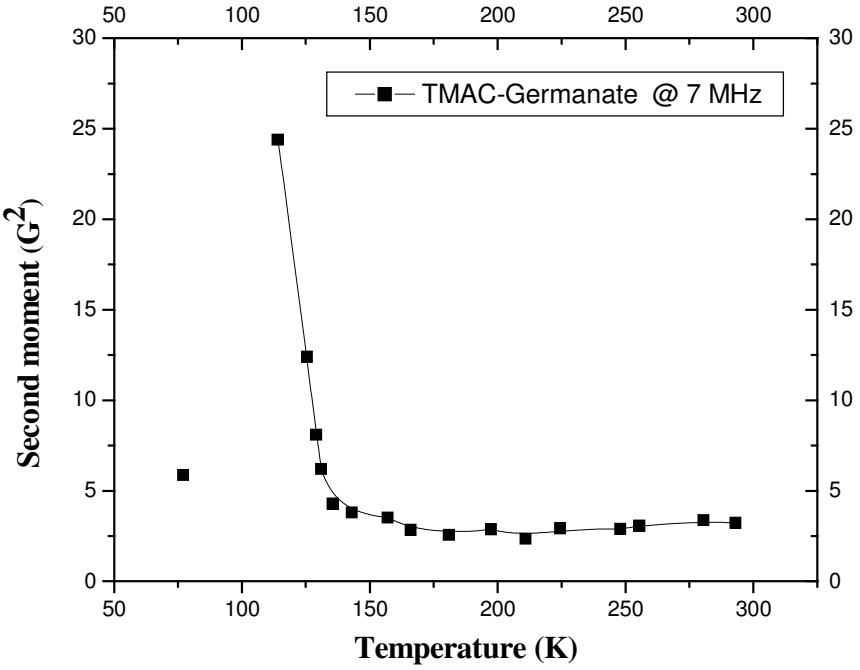

Figure 5.7 ^{1}H NMR Second moment data of TMAC-Germanate at 7 MHz in the temperature region 300-77 K; the line is guide to the eye.

There are many second moment simulation studies reported in the literature including those for Tetramethylammonium ion in different complexes [54 - 61]. We have calculated the second moment using standard models as explained in Chapter 4 and same theory is given here for ready reference. The rigid lattice second moment can be calculated for a rigid $(CH_3)_4N$ ion using the formula [62]

$$M_2 = \frac{9}{10}\frac{\gamma^2 \hbar^2}{r^6} + \frac{81}{20}\frac{\gamma^2 \hbar^2}{R^6} + M_{HT} \qquad (5.8)$$

where γ = 2.675 x 10^4 G^{-1} s^{-1} is the nuclear gyromagnetic ratio of protons and M_2 is measured in G^2. Following Albert et al [43], we have used r = 1.78 Å as the distance between the protons belonging to the same CH_3 group and R = 3.04 Å as the average distance between the protons belong to different groups for second moment calculations. The high temperature residual second moment M_{HT} is considered to be 1 G^2 [63] and the estimated rigid lattice M_2 value is 28 G^2 [60], which is fairly comparable with our low temperature second moment value of 24.8 G^2 (at 114 K). The observed second moment value of 24.8 G^2 is in good agreement with the rigid lattice second moment value for the Tetramethylammonium ion calculated in Tetramethylammonium bromide by Blears et al [57] and also as observed experimentally by Prabhumirashi et al in $((CH_3)_4N)_2SnCl_6$ [58]. An estimation of activation energy [59] from the formula E_a =155 T_C J/mol, where T_C is the temperature at which the NMR spectrum narrows, yields 18 kJ/mol. Since the line narrowing observed in this complex seems to occur in a single step, it can be concluded that the individual C_3 reorientation of four CH_3 groups in the cation and the overall reorientation of the cation as a whole occur simultaneously at a very narrow interval of temperature. Similar behaviour has been observed in $(CH_3)_4NCdCl_3$, but at much lower temperatures [60].

The observed plateau second moment of about 2.8 G^2 in the high temperature

region suggests that both TMA and methyl groups reorientations are active down to 160 K and below which, motions of both the groups start freezing. The present investigations show no resolved plateau in second moment (two plateau regions are expected for TMA compounds) indicating that the two motions do not have widely differing correlation frequencies [61]. The finite second moment of 5.5 G^2 at 77 K suggests the existence of rotational tunneling of the methyl groups [64], which is consistent with our low temperature T_1 results discussed below. Similar behaviour is observed by Ramesh et al [64] in second moment studies for NH_4SnBr_3 and hence predicted to be a result of tunneling. Indeed later, it has been experimentally observed by Senthil Kumaran et al [39] by T_1 measurements.

5.3.3.2 Spin lattice relaxation time

Figure 5.8 shows the variation of ^1H NMR spin lattice relaxation time (T_1) with inverse temperature (1000/T) at 26 MHz and 11.4 MHz. T_1 measurements have been carried out in the temperature region 270 – 17 K at 26 MHz, while at 11.4 MHz, the temperature range is restricted to 270 - 115 K, due to poor signal to noise ratio at lower temperatures. The magnetization recovery is found to be exponential within the experimental error throughout the temperature region studied. The T_1 data are analyzed in two parts (a) the High Temperature (HT) region (270-115 K) as shown in Fig. 5.9 and (b) the Low Temperature (LT) region (115 – 17 K) as shown in Fig. 5.10.

(a) High Temperature (HT) region (270 - 115 K)

Figure 5.8 is redrawn in Fig. 5.9 in a limited temperature range (270-115 K) for convenience of presentation of the fitting at both frequencies. Figure 5.9 shows that, T_1

plots at both frequencies show a single asymmetric minimum instead of two minima expected, corresponding to each symmetric groups(TMA and CH_3) as observed in most of the Tetramethylammonium compounds. However, this is consistent with the second moment studies described in the previous section, where the second moment as a function of temperature shows a single plateau region instead of two plateau regions. Similar behaviour has been observed in several other TMA compounds [11, 43, 47, 58].

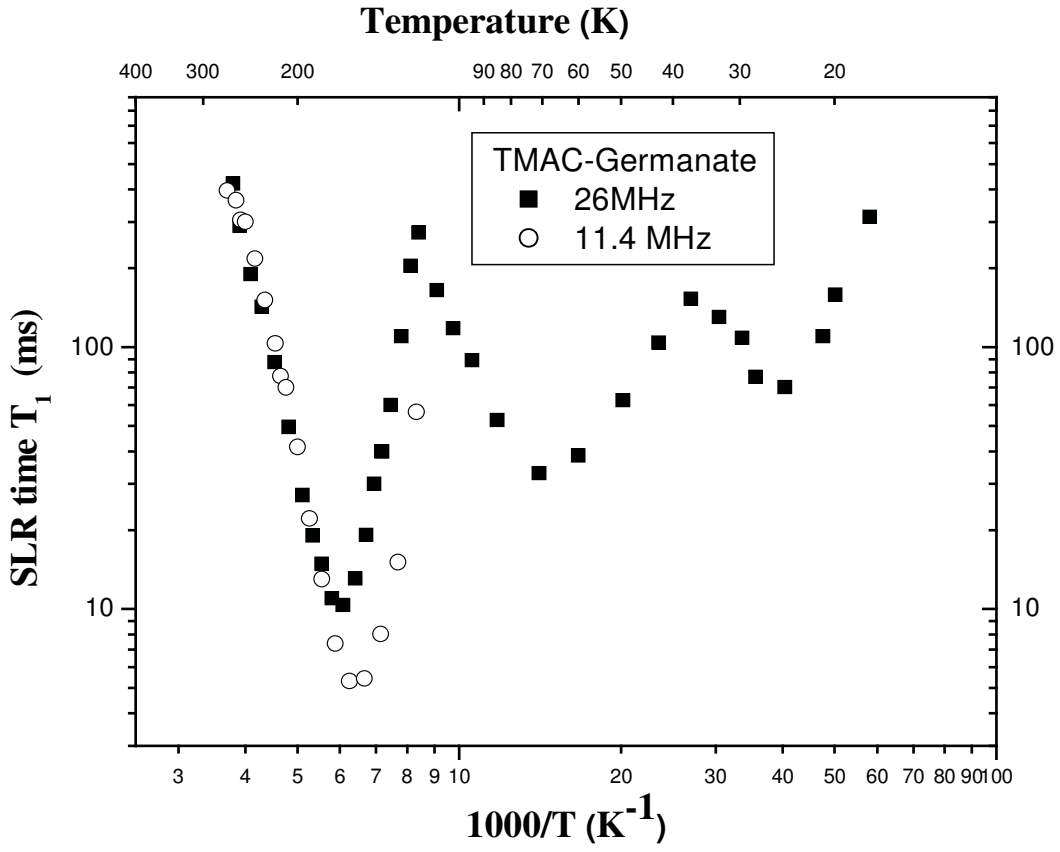

Figure 5.8 ^{1}H NMR T_1 data of TMAC-Germanate at 26 MHz (■) [270-17 K] and 11.4 MHz (○) [270-115 K].

Theory

The T_1 behaviour in Tetramethylammonium compounds can be explained using a modified BPP [41] approach, as given by Albert et al [43]. Albert et al have studied the ^1H T_1 in several Tetramethylammonium halides and the experimental results have been analyzed by considering the Tetramethylammonium ion and methyl group reorientations about their C_3 axes. In Tetramethylammonium compounds, the two motions which mainly contribute to the relaxation are (a) random reorientation of the CH_3 groups with correlation time τ_c and (b) isotropic tumbling of the TMA ion (whole cation) with a correlation time τ_{c1}. They modulate the intra-methyl and inter-methyl dipole-dipole interactions and facilitate the spin lattice relaxation.

Albert et al [43] have assumed that the observed curves could be described by two superimposed BPP curves [41] and the effective relaxation rate is the sum of the relaxation rates due to the intra-methyl and inter-methyl contributions and hence can be written as

$$T_1^{-1} = A\, f(\tau_{c2}) + B\, f(\tau_{\mathbf{c1}}) \qquad (5.9)$$

where

$$\tau_{c2}^{-1} = \tau_c^{-1} + \tau_{c1}^{-1} \qquad (5.9a)$$

$$A = \frac{9}{20}\frac{\gamma^4 \hbar^2}{r^6} \qquad (5.9b)$$

$$B = \frac{3}{20}\frac{\gamma^4 \hbar^2}{r^6} + \frac{27}{10}\frac{\gamma^4 \hbar^2}{R^6}. \qquad (5.9c)$$

Here $\gamma = 2.675 \times 10^4$ G^{-1} s^{-1} is the nuclear gyromagnetic ratio of protons, r is the inter proton distance within the methyl group and R is the distance between the centers of the triangles formed by the three protons of each CH_3 group. τ_c , τ_{c1} and τ_{c2} respectively represent the correlation time of the methyl group, TMA cation and the effective correlation time due to both methyl and TMA cation reorientations around the preferred

axes. The function f (τ) is given by

$$f(\tau) = \tau(1+\omega^2\,\tau^2)^{-1} + 4\tau(1+4\omega^2\,\tau^2)^{-1} \quad , \qquad (5.10)$$

where 'τ' represents the correlation time of the motion and is assumed to obey the Arrhenius equation given by

$$\tau = \tau_0 \exp(E_a / RT) \quad . \qquad (5.11)$$

Here τ_0 and E_a are called pre-exponential factor and activation energy of the corresponding motion respectively.

Generally in TMA salts, one expects (also evident from Eqn. 5.9) two minima corresponding to TMA reorientation (in high temperature region around 230-240 K) and methyl group reorientation around 130-160 K). In the present compound, the first minima occur around 160 K while the second and third minima occur around 70 K (32 ms) and 23 K (70 ms) respectively. The occurrence of T_1 minimum around 70 K is unlikely due to methyl group reorientation because of its temperature of occurrence and also due to its higher value of 30 ms as compared to the expected value of 14.3 ms at 26 MHz. Winkler et al [32] have also concluded from quasielastic scattering experiments that CH_3 groups reorient only above 85 K. Further, the temperature dependence of second moment also shows a single-step transition instead of two-step transition which normally occurs in TMA compounds. The high temperature T_1 minimum occurring around 160 K (at both the frequencies) is much lower in value (9.64 ms) than the expected minimum of 24.7 ms for TMA alone.

The T_1 data in this temperature region (270 -115 K) have been analyzed using the Albert et al model (Eqn. 5.9). Generally, one uses theoretically calculated values of A = 8.05 x 10^9 s^{-2} and B = 4.61x 10^9 s^{-2} for Tetramethylammonium (TMA) compounds using well known bond length and bond angles of the TMA molecule, as estimated by Albert et

al. For this compound, Albert et al model as given by Eqn. 5.9 is fit to the present experimental data by considering A and B also as fit parameters, independently for both the frequencies and the theoretical fit curves are shown as solid lines in Fig 5.9. The A and B values obtained are in good agreement with the calculated values. The fit parameters (Activation energies and pre-exponential factors) obtained for both the frequencies are within the error limits (shown in the parentheses) and are given in Table 5.7.

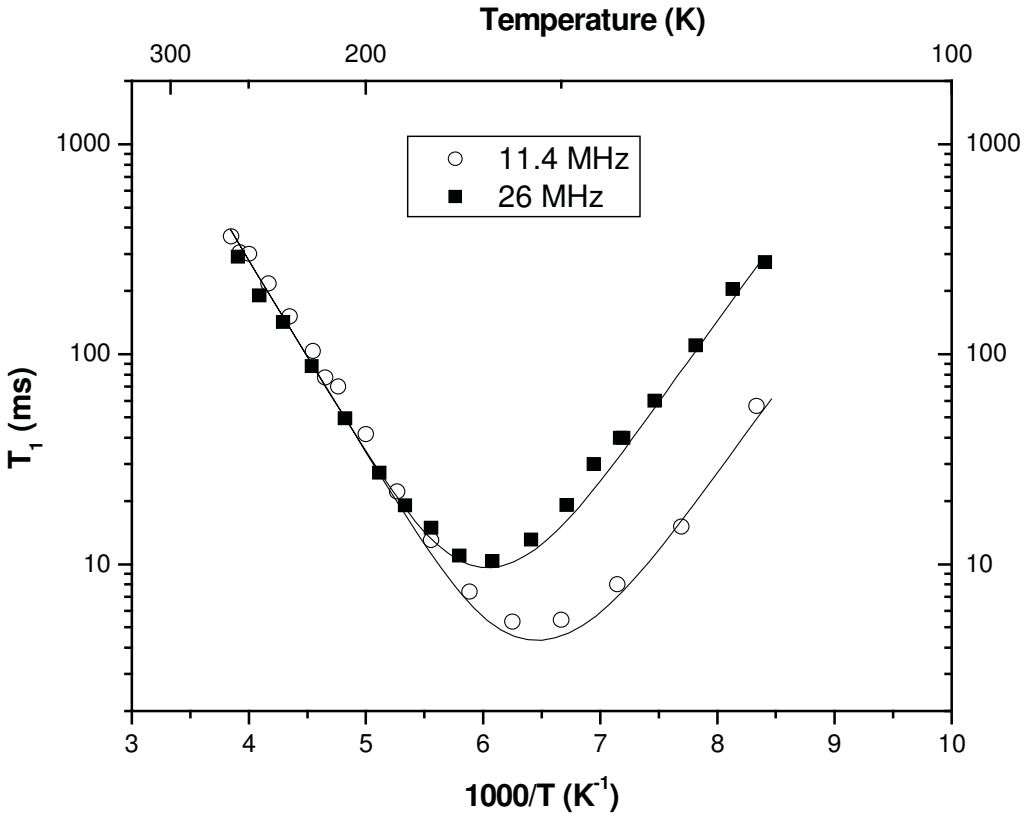

Figure 5.9 ^{1}H NMR T_1 data of TMAC-Germanate at 26 MHz (■) and 11.4 MHz (○): Solid lines represent fit to the Eqn 5.9.

The observed motional parameters are found to be in good agreement with those

reported for other TMA compounds [58, 59, 63]. The activation energy obtained from T_1 results (~18.5 kJ/mol) is in excellent agreement with that (18 kJ/mol) obtained from second moment studies. On comparing the activation energies of both the TMA and methyl groups in $(CH_3)_4NMCl_3$ (M = Cd, Sn and Ge) salts, it can be noticed that activation energy of the TMA/methyl groups increases with decreasing metal ion radius [39, 59]. This can be correlated to the increased volume (higher metal ion radius) available for the motion of the symmetric groups.

Table 5.7 Motional parameters evaluated from Albert et al model for TMA-Germanate in the temperature region (270 – 115 K). The values given in the parentheses represent the errors.

Frequency MHz	Methyl		TMA		A	*B*
	E_a kJ/mol	τ_{co} 10^{-13} s	E_a kJ/mol	τ_{co} 10^{-13} s	10^9 s^{-2}	10^9 s^{-2}
11.4	13.59 (0.7)	2.75 (0.4)	18.35 (0.8)	0.1 (0.02)	8.10 (1.2)	4.65 (0.9)
26	13.30 (0.5)	2.90 (0.4)	18.76 (0.5)	0.1 (0.02)	8.02 (1.0)	4.50 (0.7)

(b) Low temperature (LT) range (115 – 17 K)

The effects of rotational tunneling of CH_3 groups on proton spin lattice relaxation have been discussed by several authors [39, 65 - 75]. Non-exponential magnetization recovery and multiple minima in T_1 graphs at low temperatures are some of the signatures of the tunneling. Tunneling motions influence the proton spin lattice relaxation in various striking ways and no complete understanding of the spin-phonon interaction has been reached [68]. The T_1 results in the title compound show two broad asymmetric minima in the temperature region 115 - 17 K and the magnetization recovery is found to be

exponential throughout the temperature region studied. Here, the model proposed by Koksal et al [45] is tried to fit the present T_1 results by considering inequivalent CH_3 groups (A type and B type). Similar observations of multiple minima have been reported earlier [46, 74].

Theory

Koksal et al [45] have studied a number of acetates by ^{1}H NMR T_1 measurements and the experimental results are explained by considering temperature dependence of tunnel splitting. At low temperatures, it is assumed that only the torsional ground state (n = 0) of the methyl group is occupied and thermal excitations to the first level (n = 1) can be described by the correlation time

$$\tau_c^T = \tau_{co}^T \exp(E_{01}/RT) \qquad (5.12)$$

where E_{01} is the energy difference between the ground and first excited states of the torsional oscillator levels. The relaxation occurs when spin-flips are connected with the tunnel splittings. When the tunneling frequency is larger than the Larmor frequency, one can write the expression for the relaxation rate by considering only the intramethyl interaction and temperature dependence of the tunnel frequency as

$$\frac{1}{T_{AE}} = C_{AE} \sum_{m=-2}^{2} \frac{m^2 \tau_c^T}{1+ <\omega_T>^2 (\tau_c^T)^2} \quad , \qquad (5.13)$$

where $<\varpi_T>^2$ is the average tunnel frequency [46] and is given by

$$<\omega_T> = \frac{\omega_T^0 - \omega_T^1 \exp(-E_{01}/RT)}{1+\exp(-E_{01}/RT)} \qquad (5.14)$$

and

$$C_{AE} = \frac{9}{20} \frac{\gamma^4 \hbar^2}{r^6} d_0^2 \ . \qquad (5.15)$$

In the above equations, ω_T^0 and ω_T^1 are the ground and first excited torsional

tunnel splittings; d_0 is the matrix element of the space part of the dipolar operator between the ground state wave functions of the harmonic oscillator [76].

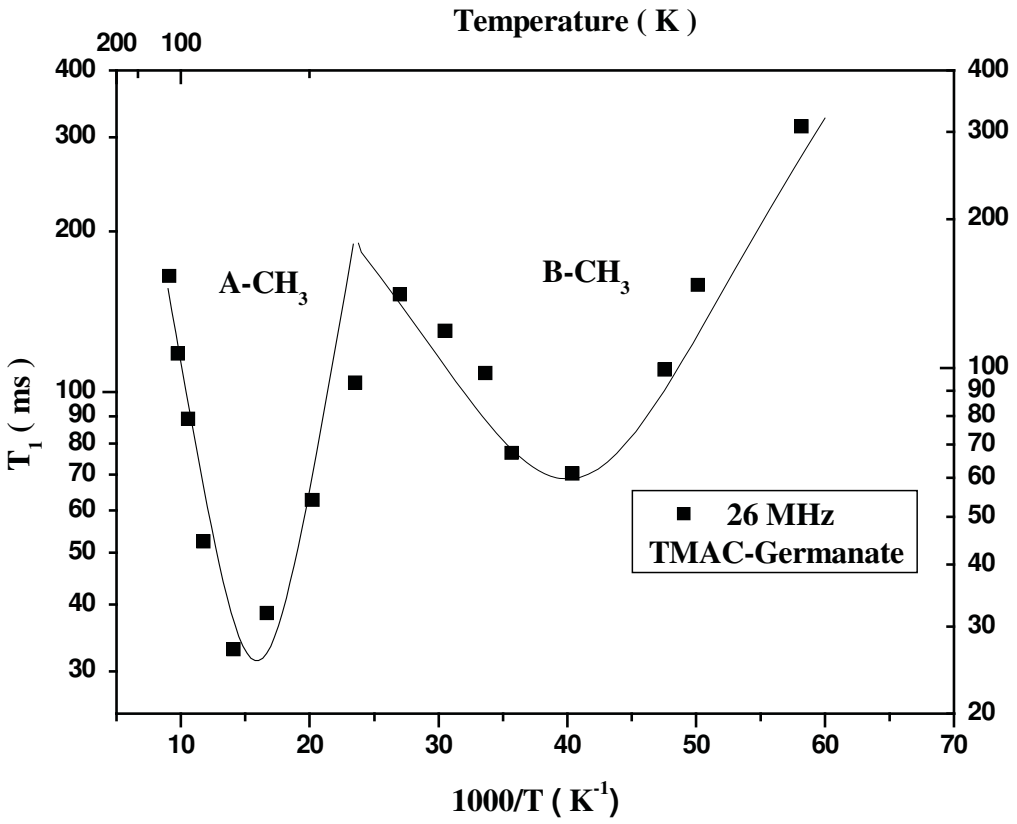

Figure 5.10 T_1 data of TMAC Germanate in the temperature range 115-17 K: Solid line represents fit to Koksal model considering inequivalent CH_3 groups [34 - 35].

Figure 5.10 shows the fit of the model proposed by Koksal et al (Eqn. 5.13) to the T_1 data between 115 and 17 K by considering the existence of inequivalent methyl groups. The best fit parameters are given in the Table 5.8. The motional parameters are comparable with those reported for $Cd(CH_3COO)_2$ [76] except the activation energy, which is comparatively less, but in reasonable agreement with the results of Senthil Kumaran et al [39].

Table 5.8 Motional parameters evaluated (115 – 17 K) using Koksal model for inequivalent CH_3 groups tunneling in TMA-Germanate. Numbers in the parentheses represent the errors.

Parameters	Best fit values	
	'A' type	'B' type
E_{01} (kJ/mol)	0.67 (0.01)	0.092 (0.01)
τ^{T}_{c0} (s)	0.09 (0.05) x 10^{-11}	4.5 (0.05) x 10^{-11}
C_{AE} (s^{-2})	40 x 10^{9}	6 x 10^{9}
ω^{0}_{T} (s^{-1})	6.9 x 10^{9}	9 x 10^{9}
ω^{1}_{T} (s^{-1})	100 x 10^{9}	45 x 10^{9}

5.3.4 CONCLUSIONS

The TMA-Germanate exhibits thermally activated reorientations of the Tetramethylammonium and methyl groups. In this compound, second moment results show only one plateau region and T_1 results show a single asymmetric minimum than expected two plateau regions in the second moment and two minima in T_1. However, if both CH_3 and TMA groups reorient relatively at same frequency (with same correlation time), then both the motions freeze around the same temperature leading to a single transition. Hence, the CH_3 and TMA groups in TMA – Germanate may also be reorienting with the same (order of magnitude) correlation times. The correlation times estimated from the present fit parameters for both the groups become 10^{-6} s around 115 K leading to a second moment transition around the same temperature [60] instead of two independent transitions. It can be inferred that the decrease of activation energy of the TMA/methyl groups with the decrease metal ion radius, in $TMABCl_3$ complexes, may be

due to the increased volume (higher metal ion (B) radius).

Present investigations have not shown any perceptible change in either M_2 or T_1 behaviour at the reported phase transition temperatures. As inferred by Klaus Fűtterer [33], the environment of TMA ion in the lattice remains unaltered when the compound undergoes a phase transition at 200 K. Present investigations also have not revealed any change in the magnetization recovery profile even below 170 K. Hence it can be concluded that the TMA ion surrounding remains unaltered through phonon transitions. At lower temperatures, T_1 results suggest the existence of the inequivalent methyl groups undergoing quantum rotational tunneling.

References

1. Fatuzzo E and Nitsche R. *Phys. Rev.,* **117**, 936 (1960).
2. Nitsche R and Fatuzzo E. *U.S. Patent* 3, **085 184** (Cl 317-262) (1963).
3. Arend H, Mulalt P, Plesko S and Altermatt D. *Ferroelectrics*, **24**, 297 (1980).
4. Bartolome J, Navarro R, Gonzalez D and Jongh LJ. *Physica*, **92B**, 23 (1977)
5. E. Palacios E, Bartolomé J, Navarro R, Garcia J, González D and Brom HB. *Ferroelectrics,* **55**, 287 (1984).
6. Raaen AM, Svare I. and Fibich M. *Phys. Scr.,* **25**, 957 (1982).
7. Steenbergen C, Graaaf LA, Bevaart L, Bartolome J and Jong LJ. *J. Chem. Phys.,* **70 (3)**, 1450 (1979).
8. Pelzl J and Dimitropoulos CZ. *Z. Naturforsch*, **49a**, 232 (1994).
9. Hallsworth R and Pintar MM. 18th *Congress Ampere, Mag. Res and Rel Phenomena*, Nottingham, **381** (1974).
10. Senthil Kumaran S. *Ph.D. Thesis*, IISc, Bangalore, India (**1997**).
11. H. Yano, Y. Furukawa, Y. Kuranaga, K. Yamada and T. Okuda, *J. Mol. Struct.*, **520**, 173 (2000).
12. Koji Yamada, Keiko Mikawa, Tsutomu Okuda and Kevin S. Knight. *J. Chem. Soc., Dalton Trans.,* **2112** (2002).
13. Tsutomu Okuda, Shusaku Gotou, Toshirou Takahashi, Hiromitsu Terao and Koji Yamada, *Z. Naturforsch*, **51a**, 686 (1996).
14. Thiele G, Rotter HW and Schmidt KD. *Z. Anorg. Allg. Chem.*, **545**, 148 (1987).
15. Thiele G, Rotter HW and Schmidt KD. *Z. Anorg. Allg. Chem.*, **559**, 7 (1988).
16. Messer D. *Z. Naturforsch., Teil B*, **33**, 366 (1978).

17. Yamada K, Nose S, Umehara T, Okuda T and Ichiba S. *Bull. Chem. Soc. Jpn.,* **61,** 4265 (1988).

18. Yamada K, Funabiki S, Horimoto H, Matsui T, Okuda T and Ichiba S. *Chem. Lett.,* **20(1)**, 801 (1991).

19. Plesko S. Kind R and Roos J. *J. Phys. Soc. Jpn*., **45**, 553 (1978).

20. Sharma S. Weiden N and Weiss A. *Z. Naturforsch., Teil A*, **46**, 329 (1991).

21. Poglitsch A Weber D. J. Chem. Phys., **87**, 6373 (1987).

22. Yamada K, Matsui T, Tsuritani T, Okuda T and Ichiba S. *Z. Naturforsch., Teil A*, **45**, 307 (1990).

23. Yamada K, Kawaguchi H, Matsui T, Okuda T and Ichiba S. *Bull. Chem. Soc. Jpn.,* **63**, 2521 (1990).

24. Onoda-Yamamuro N, Matsuo t and Suga H. J. Chem. *Thermodnam.*, **23**, 987 (1991).

25. Yamada K, KuranagaY, Ueda K, Foto S, Okuda T and Furukawa Y. *Bull. Chem. Soc. Jpn.*, **71**, 127 (1998).

26. Seo DK, Gupta N, Whangbo MH, Hillebrecht M and Thiele G. *Inorg. Chem.,* **37,** 407 (1998).

27. Rao CNR and Rao KJ, *Phase Transitions in Solids* (Mcgraw-Hill, Newyork, **1978**), p 43.

28. Serr BR, Heckert G, Rotter HW, Thiele G and Ebling D, *J. Mol. Struct.,* **348**, 95 (1995).

29. Koji Yamada, Kazuaki Isobe, Emi Tsuyama, Tsutomu Okuda and Yoshihiro Furukawa, *Solid State Ionics*, **79**, 152 (1995).

30. K. Yamada, K. Isobe, T. Okuda and Y. Furukawa, *Z. Naturforsch*, **49a**, 258 (1994).

31. NØrlund Christensen and S.E Rasmussen, *Acta Chem. Scand.,* **19(2)**, 421 (1965).

32. B. Winkler, I. Kaiser, M. Chall, G. Coddens, B. Hennion and R. Kahn, *Physica B*, **234-236**, 70 (1997).

33. Klaus Fűtterer, Wulf Depmeier and Vaclav Petŕiček, *Acta Cryst.,* **B51**, 768 (1995).

34. W. Depmeier, A. Möller and K. H. Klaska, *Acta Cryst*., **B36**, 803 (1980).

35. Poskozim PS and Stone AL, *J. Inorg. Nucl. Chem.,* **32**, 1391 (1970).

36. Möller A and J. Felsche, *J. Appl. Cryst*., **15**, 247 (1982).

37. Paul S. Poskozim and Aubrey L. Stone, *J. Organometal. Chem.,* **16**, 314 (1969).

38. Walther U, Brinkmann D, Chapuis G and Arend H. *Solid State Communications,* **27**, 901 (1978).

39. Senthil Kumaran S, Ramesh KP and Ramakrishna J, *Mol. Phy.,* **99(16)**, 1373 (2001).

40. Ryuichi Ikeda, Rainer Kadel, Alarich Weiss, Nobuku Ishida and Daiyu Nakamura. *Ber. Bunsenges. Phys. Chem.,* **86**, 685 (1982).

41. Bloembergen N, Purcell EM and Pound RV, *Phys. Rev*., **73(7)**, 679 (1948).

42. Dunn MB and McDowell CA, *Mol. Phy.,* **24**, 969 (1972).

43. Albert S, Gutowsky HS, and Ripmeester JA. *J. Chem. Phys*., **56(7)**, 3672 (1972).

44. Ratcliffe CI, *J. Phys. Chem.,* **94**, 152 (1990).

45. Köksal F, Rössler E and Sillescu H. *J. Phys. C: Solid State Phys.,* **15**, 5821 (1982).

46. Műller-Warmuth W, Schűler R, Prager M and Kollmar A. *J. Chem. Phys.,* **69(6)**, 2382 (1978).

47. Mallikarjunaiah KJ, Paramita KC, Ramesh KP and Damle R. *Solid State Nucl. Magn. Reson.,* **32 (1)**, 11 (2007).

48. Fatuzzo E, Nitsche R, Roetschi H and Zingg S. *Phys. Rev.,* **125**, 514 (1962).

49. Sarma BS and Ramakrishna J. *Curr. Sci.,* **53**, 459 (1984).

50. Vijayaraghavan D and Ramakrishna J. *Spectrochim Acta*. **49A**, 1121 (1993).

51. Ramesh KP, Devaraj ND and Ramakrishna J. *Proc. DAE Sol. St. Phys. Symp*., **32**, 303 (1989).

52. Möller A and Felsche J. *J. Appl. Cryst.*, **12,** 617 (1979).

53. Svare I. and Ain el Hiah Abd el Haleem. *Phys. Scr.,* **19(4),** 351 (1979).

54. Goc R, *J. Magn. Reson*., **132,** 78 (1998).

55. Goc R, Comp. *Phys. Comm*., **162,** 102 (2004).

56. Goc R, *Z. Naturforsch*. **58a,** 537 (2003).

57. Blears DJ, Danyluk SS and Bock E. *J. Phys. Chem.,* **72(6),** 2269 (1968).

58. Prabhumirashi LS, Ryuichi Ikeda and Daiyu Nakamura, *Ber. Bunsenges. Phys. Chem.,* **85**, 1142 (1981).

59. Waugh JS and Fedin EI, *Soviet Physics Solid State*. **4**, 1633 (1963).

60. Tung Tsang and Utton DB. *J. Chem. Phys*., **64(9)**, 3780 (1976).

61. Andrew ER and Canepa PC. *J. Magn. Reson.,* **7**, 429 (1972).

62. Abragam A, *The Principles of Nuclear Magnetism*. Oxford University Press; New York, **1961.**

63. Mahajan M and Nageswara Rao BD, *J. Phy. C: Solid State Phys.,* **7**, 995 (1974).

64. Ramesh. KP, Devaraj N, Ramakrishna J, Venu K and Sastry VSS. *Spectrochim Acta.* **49A**, 1773 (1993).

65. Latonowicz L. *J. Concept. Magn. Reson.,* A. **27(1),** 38 (2005).

66. Latonowicz L. *J. Phys. Chem. A*. **108(51)**, 11172 (2004).

67. Latonowicz L, Medycki W and Jakubas R. *J. Phys. Chem. A*. **109(14)**, 3097 (2005).

68. Horsewill AJ. *Progr. in Nucl. Magn. Reson. Spectro.,* **35,** 359 (1999)

69. Svare I, Raaen AM and Finland WO. *Physica B.* **128,** 144 (1985).

70. Svare I, Raaen AM and Thorkildsen G. *J. Phy. C: Solid State Phys.,* **11,** 4069 (1978).

71. Ylinel EE, Tuohi JE and Niemela LKE. *Chem. Phy. Lett.,* **24**, 447 (1974).

72. Clough S, Horsewill AJ, Johnson, MR, Sutchliffe JH and Tomsah IBI. *Mol. Phys*., **81,** 975 (1994).

73. Ingman LP, Punkkinen M, Vuorimaki AH and YLinen EE. *J. Phy. C: Solid State Phys.,* **18,** 5033 (1985).

74. Tuohi JE and YLinen EE. *Phys. Scri.*. **13,** 253 (1976).

75. Ingman LP, Punkkinen M, Ylinen EE and Dimitropoulos C. *Chem. Phys. Lett.,* **125,** 170 (1986).

76. Sobol WT, Sreedharan KR., Cameron IG and Pintar MM. *Z. Naturforsch*. **40a**, 1075 (1985).

Appendix 1

Program used to acquire wide-line NMR signal through an ADC (p 51).

```
1 CLS
2 SCREEN 9: KEY OFF: CLS
20 INPUT "ENTER FILENAME FOR FORWARD SCAN:", F$
21 INPUT "ENTER SCAN TIME:",ST
30 OPEN F$ FOR OUTPUT AS #1
40 BASE% = &H200
50 OUT BASE% + 10, 0
70 OUT BASE% + 12, 0
80 HI = INP(BASE% + 5)
90 IF HI >= 16 THEN 80
100 LO = INP (BASE% + 4)
110 XVOLT = (HI * 256 + LO - 2048)* 10/4096
120 H = XVOLT
130 H= HOLD
131 Y=0
135 TIM=TIMER
140 WHILE (TIMER-TIM)=< ST
143 IF TIMER > (TIM+(Y*(ST/640))) GOTO 150 ELSE 143
150 OUT BASE% + 10, 2
160 OUT BASE% + 12, 0
170 HI = INP(BASE% + 5)
180 IF HI >= 16 THEN 170
185 LO = INP(BASE% + 4)
190 XVOLT = (HI * 256 + LO - 2048) * 10/4096
200 H = XVOLT * 711.4
210 IF H = HOLD THEN GOTO 320
211 PSET(Y,175+((-INTENSITY*50)+40))
216 Y=Y+1
220 HOLD = H
222 I = 0
230 OUT BASE% + 10,1
240 OUT BASE% + 12,0
250 GI = INP(BASE% + 5)
260 IF GI >= 16 THEN 250
270 GO = INP(BASE% + 4)
280 I= I + (GI * 256 + GO - 2048) * 10/4096
285 INTENSITY = I
290 PRINT #1,      H              , "     ",INTENSITY
300 LOCATE 23, 1
310 PRINT     H                , "     ", INTENSITY
320 WEND
330 CLOSE #1
730 INPUT "DO YOU WANT TO CONTINUE?",ST$
740 IF ST$ = "y" GOTO 2
741 IF ST$ = "Y" GOTO 2
750 END
```

Appendix 2

Program used to generate pulse sequences using PCI DIOT (p 59).

```
#include<dos.h>
#include<stdio.h>
#include<conio.h>
#include<dos.h>
#include<process.h>
# define tim1 0xb400
void singlepulse(void)
    {
    int ton1,toff;
    register short ton,tp;
    clrscr();
    gotoxy(20,5);
     printf("Single Pulse Generation Mode");
     gotoxy(20,8);
     printf("Enter ON Time of the Pulse (micro seconds):");
     scanf("%d",&ton1);
     ton=ton1;
     tp=ton1*2;
    gotoxy(20,10);
    printf("Enter OFF time of the Pulse (Milli seconds):");
     scanf("%d",&toff);
     outportb(tim1+3,0x10);
     outportb(tim1+3,0x50);
     gotoxy(20,15);
     printf(" Press any key Quit");
     while(!kbhit())
            {
             outportb(tim1+1,tp);
             outportb(tim1,ton);
             delay(toff);
            }
            getch();
     return;
    }
void doublepulse(void)
    {
    int t11,t31,t2,t4;
    register short t1,t3,t3t;
    clrscr();
    gotoxy(20,5);
     printf("Double Pulse Generation Mode");
     gotoxy(20,8);
     printf("Enter T1on Time of the Pulse (micro seconds):");
     scanf("%d",&t11);
     t1=t11;
```

```
      gotoxy(20,10);
      printf("Enter T2on Time of the Pulse (micro seconds):");
      scanf("%d",&t31);
      t3=t31;
      t3t=t31*2;
     gotoxy(20,12);
     printf("Enter T1off tim of the Pulse (Milli seconds):");
      scanf("%d",&t2);
      gotoxy(20,14);
      printf("Enter T2off tim of the Pulse (Milli seconds):");
      scanf("%d",&t4);
      outportb(tim1+3,0x10);
      outportb(tim1+3,0x50);
      gotoxy(20,20);
      printf(" Press any key Quit");
      while(!kbhit())
             {
              outportb(tim1,t1);
              delay(t2);
              outportb(tim1+1,t3t);
              outportb(tim1,t3);
              delay(t4);
             }
            getch();
      return;
     }
void tribblepulse(void)
     {
     int t11,t31,t51,t2,t4,t6;
     register short t1,t3,t5,tp;
     clrscr();
     gotoxy(20,5);
      printf("Tripple Pulse Generation Mode");
      gotoxy(20,8);
      printf("Enter T1on Time of the Pulse (micro seconds):");
      scanf("%d",&t11);
      t1=t11;
      gotoxy(20,10);
      printf("Enter T2on Time of the Pulse (micro seconds):");
      scanf("%d",&t31);
      t3=t31;
      gotoxy(20,12);
      printf("Enter T3on Time of the Pulse (micro seconds):");
      scanf("%d",&t51);
      t5=t51;
      tp=t51*2;
     gotoxy(20,14);
     printf("Enter T1off tim of the Pulse (Milli seconds):");
```

```
      scanf("%d",&t2);
      gotoxy(20,16);
      printf("Enter T2off tim of the Pulse (Milli seconds):");
      scanf("%d",&t4);
      gotoxy(20,18);
      printf("Enter T3off tim of the Pulse (Milli seconds):");
      scanf("%d",&t6);
      gotoxy(20,22);
      printf(" Press any key Quit");

      outportb(tim1+3,0x10);
      outportb(tim1+3,0x50);
      while(!kbhit())
            {
             outportb(tim1,t1);
             delay(t2);
             outportb(tim1,t3);
             delay(t4);
             outportb(tim1+1,tp);
             outportb(tim1,t5);
             delay(t6);
            }
           getch();
      return;
     }
void pulsetrain(void)
     {
     int ton1,toff,tp,count;
     register short ton,i;
     clrscr();
     gotoxy(20,5);
      printf("Single Pulse Train Generation Mode");
      gotoxy(20,8);
      printf("Enter ON Time of the Pulse (micro seconds)     :");
      scanf("%d",&ton1);
      ton=ton1;
     gotoxy(20,10);
     printf("Enter OFF tim of the Pulse (Milli seconds)      :");
      scanf("%d",&toff);
      gotoxy(20,12);
     printf("Enter  Time b/w Two Pulse Trains (Milli seconds):");
      scanf("%d",&tp);
      gotoxy(20,14);
     printf("Enter Number of Pulses in the Train             :");
      scanf("%d",&count);
      gotoxy(20,18);
      printf(" Press any key Quit");
      outportb(tim1+3,0x10);
```

```
     while(!kbhit())
            {
           for(i=1;i<=count;i++)
             {
              outportb(tim1,ton);
              delay(toff);
             }
            delay(tp);
           }
           getch();
     return;
    }

void main()
{
int choice,i=1;
while(i)
   {
    clrscr();
    gotoxy(20,7);
    printf("1. Single Pulse Generation");
    gotoxy(20,9);
    printf("2. Double Pulse Generation");
    gotoxy(20,11);
    printf("3. Tripple Pulse Generation ");
    gotoxy(20,13);
    printf("4. Single Pulse Train Generation Mode ");
    gotoxy(20,15);
    printf("5. Quit");
    gotoxy(20,17);
    printf("   Enter The Choice:");
    gotoxy(40,17);
    scanf("%d",&choice);

    switch(choice)
            {
             case 1:singlepulse();                    break;
             case 2:doublepulse();                     break;
             case 3:tribblepulse();                   break;
             case 4:pulsetrain();              break;
             case 5: exit(0);

             default:
                       printf("\n\nEnter the correct choice");
                       getch();
            }
    }
}
```